

Physical Properties of Arctic and Antarctic Aerosol Particles and Cloud Condensation Nuclei

Von der Fakultät für Physik und Geowissenschaften

der Universität Leipzig

genehmigte

DISSERTATION

zur Erlangung des akademischen Grades

doctor rerum naturalium

Dr. rer. nat.

vorgelegt

von Master Meteorologe Paul Herenz

geboren am 25. Januar 1989 in Riesa

Gutachter: Prof. Dr. Manfred Wendisch

Prof. Dr. Andreas Macke

Asst. Prof. Dr. Paul Zieger

Tag der Verleihung 16. September 2019

Bibliographische Beschreibung:

Herenz, Paul

Physical Properties of Arctic and Antarctic Aerosol Particles and Cloud

Condensation Nuclei

Universität Leipzig, Dissertation

97 S.*, 121 Lit.*, 32 Abb., 4 Tab., Anlagen

Referat: Aerosol Partikel interagieren mit solarer und terrestrischer Strahlung durch Absorption und Streuung. Zusätzlich bilden und modifizieren sie die Eigenschaften von Wolken da sie das Potential besitzen als Wolkenkondensationskeim (CCN) fungieren zu können und stellen somit eine wichtige Komponente im Klimasystem dar. Die Eigenschaften von Partikeln und CCN müssen genauestens bekannt sein um deren Einfluss in Klima- und Strahlungsmodellen akkurat berücksichtigen zu können.

Ziel dieser Arbeit ist die Charakterisierung der Partikeleigenschaften in Regionen, welche das Klima maßgeblich beeinflussen, wie die Arktis und die Antarktis. Im Rahmen dieser Arbeit wurden 2 Datensätze aufgenommen, welche helfen das Verständnis über Partikel und CCN im Frühjahr und Sommer in der Arktis und Antarktis zu verbessern. Es wurden jeweils die Gesamt- und CCN-Anzahlkonzentration (N_{CN} , N_{CCN}), die Anzahlgrößenverteilung ($PNSD$) und der Hygroskopizitätsparameter (κ) der Partikel bestimmt. Die Herkunft der vermessenen Partikel wurde mit Rückwärtstrajektorien ermittelt sowie weitere Analysen bezüglich der Verweilzeiten durchgeführt.

Beide Datensätze zeigen, dass eine starke Abhängigkeit der Partikel- und CCN-Eigenschaften vom Luftmassenursprung vorliegt. Zeigen arktische $PNSDs$ nur eine Akkumulationsmode, konnte diese auf gealtertes Aerosol mit einem eurasischen Ursprung zurückgeführt werden. Kommt eine zweite Mode mit kleineren Partikeln hinzu, wurde der Nord-Pazifische Raum als Ursprung bestimmt. In der Antarktis wurde besonders für N_{CN} und N_{CCN} eine starke Abhängigkeit vom Luftmassenursprung gefunden. Dabei konnten mit der Anwendung des Dispersionsmodells NAME Antarktische Hintergrundkonzentrationen ermittelt werden. Weiterhin wurde gefunden, dass Antarktische Aerosolpartikel mit einem κ von 1 hygroskopischer als das Arktische ist, für welches ein κ von 0,19 bestimmt wurde. Zusätzlich durchgeführte Flugzeugmessungen über Tuktoyaktuk (Arktis) zeigen, dass die Messungen am Boden auch repräsentativ für die Grenzschicht sind. Die Schichten über der Grenzschicht scheinen jedoch von dieser entkoppelt zu sein und es wird vermutet, dass der Ursprung der Partikel in größeren Höhen in niedrigeren geographischen Breiten liegt.

*

97 S. (Seitenzahl insgesamt)

121 Lit. (Anzahl der im Literaturverzeichnis ausgewiesenen Literaturangaben)

Bibliographic Description:

Herenz, Paul

Physical Properties of Arctic and Antarctic Aerosol Particles and Cloud

Condensation Nuclei

University of Leipzig, Dissertation

97 pp.* , 121 Ref.* , 32 Fig., 4 Tab., Appendix

Abstract:

Atmospheric aerosol particles interact with solar and terrestrial radiation by absorption and scattering. Further, they have the potential to act as cloud condensation nuclei (CCN) and to form and modify the radiative properties of clouds and thus are an important component in the Earth's climate system. An accurate knowledge about the aerosol particle and CCN properties is very important for accurate climate and radiation models.

The objective of this thesis is the characterization of aerosol particles in regions that are key regulators of the Earth's climate. The Arctic and the Antarctic are such regions. Hence, in the framework of this doctoral thesis two data sets were recorded, that help gaining further knowledge about the spring and summer time aerosol particles and CCN in the Arctic and Antarctic region.

For both, the Arctic and the Antarctic aerosol population, the CCN and the total particle number concentration (N_{CCN} , N_{CN}), the particle number size distribution ($PNSD$) and the hygroscopicity parameter κ were determined. The history of the measured air masses was explored using back trajectories and residence time analysis.

For both examined regions, a strong influence of the air mass origin on the aerosol particle and CCN properties was found. The $PNSDs$ measured in the Arctic were found to be mono-modal showing an accumulation mode which most likely contains well aged particles that have an Eurasian origin. Bi-modal $PNSDs$ with an additional mode of smaller particles were found to originate from the Northern Pacific. In the Antarctic the air mass origin was found to significantly influence N_{CCN} and N_{CN} . With the application of the NAME dispersion model Antarctic continental background concentrations could be determined. With κ values of 1 the Antarctic aerosol was found to be much more hygroscopic than the Arctic aerosol, for which a κ of 0.19 was determined. Additional Arctic aircraft measurements show that ground based measurements are representative for the Arctic boundary layer. However particles above the boundary layer seem to be decoupled from lower layers and were believed to be advected from lower latitudes in different height layers and mixed down in the lower Arctic troposphere.

*

97 pp. (number of pages)

121 Ref. (Number of references)

Contents

List of Abbreviations	iii
List of Symbols	v
1. Introduction	1
2. Experimental	9
2.1. Measured Properties	9
2.1.1. Total Particle Number Concentration	9
2.1.2. Particle Number Size Distribution	10
2.1.3. Total Concentration of Cloud Condensation Nuclei	15
2.2. Determination of the CCN hygroscopicity	16
2.2.1. Köhler theory	16
2.2.2. The hygroscopicity parameter κ and the critical diameter d_{crit}	18
2.3. Determination of the Air Mass Origin	20
2.3.1. The NAME Dispersion Model	20
2.3.2. Potential Source Contribution Function	22
3. Results and Discussion	25
3.1. Measurements of aerosol and CCN properties in the Mackenzie River delta (Canadian Arctic) during Spring-Summer transition in May 2014	25
3.1.1. Campaign overview	25
3.1.2. Overview of N_{CN} , N_{CCN} and $PNSD$ data for the entire measure- ment period	29
3.1.3. Identification of air mass origins and potential source regions	32
3.1.4. $PNSD$ of the three periods	35
3.1.5. Critical diameter d_{crit} and hygroscopicity parameter κ	38
3.1.6. Comparison of height resolved airborne and ground based $PNSDs$	41
3.2. Measurements of aerosol and CCN properties at the Princess Elisabeth Antarctica Research Station during three austral summers	45
3.2.1. Campaign overview	45

3.2.2. Total Particle and CCN number concentrations and regional analysis of the NAME model footprints	50
3.2.3. PSCF results	59
3.2.4. Hygroscopicity	61
4. Summary, Conclusions and Outlook	65
A. Appendix	71
A.1. SS calibration of the CCNC	71
A.2. Error Analysis with Monte Carlo Simulation	73
B List of Figures	vii
C List of Tables	viii
Bibliography	xi

List of Abbreviations

Acronym	Description
<i>ACLOUD</i>	Arctic CLOUD Observations Using airborne measurements during polar Day
<i>APD</i>	Avalanche Photodiode
<i>ARCPAC</i>	Aerosol, Radiation, and Cloud Processes affecting Arctic Climate
<i>ARCTAS</i>	Arctic Research of the Composition of the Troposphere from Aircraft and Satellites
<i>ASL</i>	Above Sea Level
<i>AWI</i>	Alfred Wegener Institute for Polar and Marine Research
<i>AWS</i>	Automatic Weather Station
<i>BACCHUS</i>	Impact of Biogenic versus Anthropogenic emissions on Clouds and Climate: towards a Holistic Understanding
<i>CCN</i>	Cloud Condensation Nuclei
<i>CCNC</i>	Cloud Condensation Nuclei Counter
<i>CE</i>	Continental Events
<i>CN</i>	Condensation Nuclei
<i>CPC</i>	Condensation Particle Counter
<i>DMA</i>	Differential Mobility Analyzer
<i>DMS</i>	Dimethyl Sulfide
<i>DMT</i>	Droplet Measurement Technologies
<i>DWD</i>	Deutscher Wetterdienst
<i>ECMWF</i>	European Center of Medium-Range Weather Forecasts
<i>EMAC</i>	ECHAM-MESSy Atmospheric Chemistry
<i>GDAS</i>	Global Data Assimilation System
<i>IPCC</i>	Intergovernmental Panel on Climate Change
<i>LAGRANTO</i>	Lagrangian analysis tool
<i>LAS</i>	Laser Aerosol Spectrometer
<i>MCS</i>	Monte Carlo Simulation
<i>ME</i>	Marine Events
<i>MODIS</i>	Moderate Resolution Imaging Spectroradiometer
<i>MPI</i>	Max Planck Institute
<i>MSA</i>	Methane Sulfonic Acid
<i>NAME</i>	Numerical Atmospheric dispersion Modelling Environment
<i>NETCARE</i>	Network on Climate and Aerosols: Addressing Key Uncertainties in Remote Canadian Environments
<i>NOAA</i>	National Oceanic and Atmospheric Administration

Acronym	Description
<i>HYSPLIT</i>	Hybrid Single Particle Lagrangian Integrated Trajectory Model
<i>NPF</i>	New Particle Formation
<i>OPC</i>	Optical Particle Counter
<i>PDF</i>	Probability Density Function
<i>PE</i>	Princess Elisabeth
<i>PM</i>	Particulate Matter
<i>POM</i>	Particulate Organic Matter
<i>PSCAL</i>	Physical feedback of Arctic PBL, Sea ice, Cloud And Aerosol
<i>PSL</i>	Polystyrene Latex
<i>RACEPAC</i>	Radiation-Aerosol-Cloud Experiment in the Arctic Circle
<i>RH</i>	Relative Humidity
<i>SMPS</i>	Scanning Mobility Particle Sizer
<i>SS</i>	Supersaturation
<i>TROPOS</i>	Leibniz-Institut for Tropospheric Research
<i>UHSAS</i>	Ultra-High Sensitivity Aerosol Spectrometer
<i>UM</i>	Unified Model
<i>VERDI</i>	Vertical Distribution of Ice in Arctic Clouds
<i>VOC</i>	Volatile Organic Compounds

List of Symbols

Acronym	Description
D	Diameter of a solution droplet
d_p	Diameter of dry aerosol particles
d_{50}	Diameter at which 50 % of the particles are detected
d_{act}	Activation diameter
d_{crit}	Critical diameter
e	Vapor pressure
$e_{s,w}$	Saturation water vapor pressure
e_w	Water vapor pressure
κ	Kappa
M_w	Molar mass
n_s	Number of moles of a solute
N	Number
N_{CCN}	Number concentration of cloud condensation nuclei
$N_{CCN,0.1}$	Number concentration of cloud condensation nuclei at SS = 0.1%
N_{CN}	Total aerosol particle number concentration
N_{CNraw}	Total aerosol particle number concentration not filtered
$N_{summer,type}$	Trajectories indicating summer air masses
$N_{spring,type}$	Trajectories indicating spring air masses
N_2	Nitrogen
$NaCl$	Sodium chloride
O_2	Oxygen
p	Pressure
$PNSD$	Particle Number Size Distribution
$PSCF$	Potential Source Contribution Function
PM_{10}	Particulate Matter of particles < 10 nm (aerodynamical diameter)
R	Ideal Gas Constant
RH, RH_w	Relative Humidity with respect to water
RH_i	Relative Humidity with respect to ice
s_{MC}	MCS signal
S_w	Saturation ratio
S_{crit}	Critical Saturation ratio
SS, SS_w	Supersaturation with respect to water
SS_{crit}	Critical Supersaturation

List of Symbols

Acronym

Description

T	Absolute temperature
ε_i	Volume fraction of an individual chemical species
ρ_w	Density of water
σ	Standard derivation
$\sigma_{s/a}$	Surface tension of a solution droplet

1. Introduction

An aerosol is a suspension of liquid or solid particulate matter in a gaseous medium. Atmospheric aerosol particles have a huge impact on the Earth's climate and its current change by interacting with solar and terrestrial radiation, water vapor and other components of the atmosphere (IPCC, 2013). Furthermore, aerosol particles influence human health by causing heart diseases and allergies (IPCC, 2013). It is the diverse properties of aerosol particles like their concentrations and sizes, their chemical composition but also their spatial temporal distribution, that determine their influence on weather and climate and lead to multitude of interactions within the Earth's atmosphere as well as with human health. Hence, their investigation is of utmost importance.

The total aerosol particle number concentration (N_{CN}) is a simple but extremely variable parameter and can span up to several orders of magnitudes. In remote marine or high latitude regions N_{CN} values as low as 10 cm^{-3} are possible. Over rural regions, at mountain stations and near seashores N_{CN} reaches from a few hundred to a few thousand cm^{-3} . In polluted air over cities or during new particle formation (NPF) events N_{CN} values up to 10^6 cm^{-3} can be reached (Pruppacher and Klett, 1997). N_{CN} depends on the geographic region and is strongly affected by formation processes and anthropogenic influences. Also, aerosol particles feature many different sizes ranging from some nanometers to some hundreds of micrometers. The combination of the particle size with the corresponding number concentration is called the Particle Number Size Distribution (*PNSD*). Because of typical formation, growth and loss processes of atmospheric aerosol particles, their *PNSD* usually appears in form of different size modes. The smallest aerosol particles, that are indirectly emitted into the atmosphere and formed due to nucleation from the gas-phase, build the nucleation mode, containing aerosol particles up to $\approx 10\text{ nm}$. For their formation process precursor gases like sulfur dioxide, nitrous oxides or volatile organic compounds (VOCs) are necessary. Due to condensation of low vapor pressure substances on already existing aerosol particles or due to coagulation, larger aerosol particles are formed, which show up in the size range of the Aitken and accumulation mode (Seinfeld and Pandis, 1998). The Aitken mode contains aerosol particles between ≈ 10 and $\approx 70\text{ nm}$ and the accumulation mode between $\approx 70\text{ nm}$ and $\approx 1\text{ }\mu\text{m}$. However, aerosol particles in these size ranges can also be directly emitted into the atmosphere e.g., by mechanical processes or combustion. Also the largest particles, that form the coarse mode with diameters larger than $\approx 1\text{ }\mu\text{m}$, are directly emitted into the atmosphere. Examples are dust, ash and

sea spray particles, but also organic and biogenic particles like pollen, bacteria and spores are typical for the coarse mode size range.

Under specific conditions, aerosol particles can act as cloud condensation nuclei (CCN) and form cloud droplets. Whether a particle forms a cloud droplet depends on the chemical composition and the size of the particle as well as the surrounding supersaturation (SS). The process of the cloud droplet formation is described by the Köhler theory (Köhler, 1936). Aerosol particles can influence the climate either directly, by scattering or absorption of radiation, or indirectly due to their impact on cloud formation and cloud properties. A change in the amount of available aerosol particles can modify cloud properties and indirectly change the energy budget. Twomey (1974) found that an increased number concentration of CCN leads to smaller but more numerous cloud droplets if the same amount of water vapor is available for cloud formation. From this follows an increased cloud reflectivity which changes the interaction with incoming shortwave radiation. On the other hand a higher droplet number concentration would also lead to an increased cloud longwave emissivity which potentially warms the Earth's surface (Garrett et al., 2002; Lubin and Vogelmann, 2006). Further, a shift of the droplet size distribution to smaller sizes can also affect cloud lifetime due to a possible later onset of precipitation (Albrecht, 1989). The direct effect of aerosol particles is well understood. In contrast to this, the numerous indirect aerosol effects are less understood. The influence of indirect aerosol effects on the global climate and the radiative forcing still features a low confidence level and large uncertainties (IPCC, 2013).

The impact of aerosol particles on clouds, climate and global radiative forcing is mainly determined by their physical and chemical properties. Investigations of these properties of aerosol particles in general and of CCN in particular by means of in situ measurements at various different sites and conditions are necessary to lower the uncertainties that are reported by the IPCC (IPCC, 2013). A huge number of scientific projects that took place during the last years focused on aerosol particles, the characterization of their properties and their interaction with clouds and the Earth's climate. One of these projects was BACCHUS (Impact of Biogenic versus Anthropogenic emissions on Clouds and Climate: towards a Holistic UnderStanding) which is a collaborative European project organized by the ETH Zurich. One key goal of BACCHUS is to characterize aerosol particles in regions that are key regulators of the Earth's climate as well as regions that experience the most intense climate changes with possible irreversible transitions. Without any doubt the high latitude areas, the Arctic and the Antarctic, are such regions. Therefore, this doctoral thesis, which was realized within the framework of BACCHUS, focuses on the characterization of aerosol particles and CCN in the Arctic and Antarctic region.

The Arctic region is particularly sensitive to climate forcing and reacts with a number of amplifying feedback mechanisms (Law and Stohl, 2007). Thereby aerosol particles

have the ability to modify these feedbacks in different ways. One example is the deposition of black carbon on ice surfaces, which can significantly change the surface albedo, supporting the uptake of heat due to absorption (Keegan et al., 2014). This effect triggers the albedo-sea ice feedback which describes that melting ice surfaces are replaced by open water surfaces with a lower albedo which in turn increases the temperature so that more ice surfaces melt. Further, the indirect effect of aerosol particles due to their impact on cloud formation has a special relevance in terms of the Arctic. The generally cooling cloud albedo effect (shortwave radiation) for example might be of limited relevance in the Arctic since its surface is highly reflective due to snow and ice (Tietze et al., 2011). However, Garrett et al. (2002) found a high sensitivity of arctic clouds to pollution with respect to their longwave emissivity. Especially for thin stratus clouds during Arctic winter and early spring even the addition of a low number of anthropogenic CCN seems to substantially increase the clouds liquid water content. As these low altitude clouds tend to be warmer than the surface, the Arctic is potentially sensitive to this effect which potentially warms the surface in the Arctic. Hence the resulting issues that were in the focus of Arctic aerosol studies in the last years are the characterization of particle sources, their chemical and physical properties as well as the direct and indirect impacts of Arctic aerosol particles and pollutants on cloud forming properties (Jacob et al., 2010).

It is well known that the origin of Arctic air masses is dependent on the season. Connected to that, there are recurring yearly cycles of both N_{CN} and $PNSD$. Tunved et al. (2013) describe these cycles based on measurements taken for the years 2000 to 2010 at Mt. Zeppelin on Svalbard.

In winter and spring the Arctic aerosol in general is dominated by long-range transport of mid-latitude air masses. The polar front is located further south in areas of high anthropogenic pollution so that anthropogenic industrial emissions reach the Arctic atmosphere (Iversen and Joranger, 1985). Also biomass burning in Russia contributes to the high aerosol particle loading during winter and spring (Warneke et al., 2009). During polar night, the Arctic atmosphere is extremely stable which prevents turbulent mixing between vertical layers and with that also cloud formation and precipitation (Shaw, 1981). Hence the so called Arctic haze can be trapped for 15 up to 30 days (Shaw, 1981, 1995). The major part of the Arctic haze consists of particulate organic matter (POM) and sulfate but also contains ammonium, nitrate, mineral dust, black carbon and heavy metals (Quinn et al., 2002). Reported $PNSDs$ show an accumulation mode with N_{CN} constantly increasing during the winter months from October until April from below 50 to above 200 cm^{-3} (Tunved et al., 2013).

During the transition from spring to summer an increased vertical mixing causes the presence of low-level clouds and the related wet removal stops the Arctic haze period (Tunved et al., 2013), making the well aged (Heintzenberg, 1980) Arctic haze particles of the accumulation mode disappear (Engvall et al., 2008; Tunved et al., 2013). Indeed, these

precipitation related scavenging processes, which are effective from late spring throughout the summer, were shown to be among the drivers of the yearly cycle in Arctic *PNSDs* (Browse et al., 2012; Croft et al., 2016a). Resulting low number concentrations of particles in the accumulation mode size range enable new particle formation (NPF). The latter is also based on the presence of MSA (methane sulfonic acid), an oxidation product of DMS (dimethyl sulfide) that is emitted due to biological activity in the oceans (Quinn et al., 2007; Leaitch et al., 2013), with increasing emissions related to the decline of the Arctic sea ice cover (Sharma et al., 2012). Additionally, ammonia, also a contributor to NPF, was described to be connected to seabird colonies by Croft et al. (2016b) and Wentworth et al. (2016) and was discussed to have a far ranging influence on the Arctic aerosol. In general, during the Arctic summer locally and freshly produced aerosol particle species are dominant, driven by an increase in both biological activity and photochemistry, (Ström et al., 2009) showing up as a pronounced Aitken mode in *PNSDs* in summer month, particularly in July and August (Tunved et al., 2013).

Consequently, the Arctic aerosol particle number size distribution as well as the particle number concentrations show a large seasonal variability (Tunved et al., 2013). Moreover the sources and sinks for Arctic aerosol particles are subject to the fast changes in the Arctic that currently take place. Dall'Osto et al. (2017a) for instance found a negative correlation between the Arctic sea ice extent and NPF events, that were observed at Mt. Zeppelin (Svalbard). From this connection follows an increased new particle production due to the current decrease in the sea ice pack extent (Dall'Osto et al., 2017a).

Croft et al. (2016a) reported data collected in the years 2011 to 2013 from Mt. Zeppelin, i.e., examining different years than Tunved et al. (2013), together with additional data from Alert, Canada. Both, yearly cycles of N_{CN} and *PNSDs* were similar at Alert and Mt. Zeppelin, and also similar to those discussed in Tunved et al. (2013). Croft et al. (2016a) suggest that the observed similarities at these two stations, which are 1000 km apart, and between the different years examined at Mt. Zeppelin indicate the existence of an annual cycle that spans the high Arctic. This assumption is corroborated by Nguyen et al. (2016), reporting comparable yearly cycles of number concentrations and *PNSDs* from the Villum Research Station in northern Greenland, only differing in more pronounced Aitken modes in the summer months. The shape of the yearly cycle of N_{CN} and the most often occurring *PNSDs* observed in Tiksi, Russia, described in Asmi et al. (2016), were again similar to those observed at Mt. Zeppelin and Alert. However, number concentrations were higher in general in Tiksi, and NPF events occurred more readily, which is suggested to be related to regional continental sources of nucleating and condensing vapors. Generally, a comparison of *PNSDs* presented in Freud et al. (2017) from Alert, Villum Research Station, Mt. Zeppelin, Tiksi and Barrow (Alaska) shows some differences between Arctic sites due to local effects, but indicates that on a large scale there is a pronounced annual cycle in *PNSDs* with common features, with all Arctic sites sharing the Asian continent

as the main large-scale source region of accumulation mode aerosols.

Similarly, also the Arctic CCN number concentrations vary, with values between less than 100 cm^{-3} (pristine Arctic background), occasionally less than 1 cm^{-3} (Mauritsen et al., 2011), and up to 1000 cm^{-3} (in Arctic haze layers, Moore et al. (2011) and references therein). In the previously mentioned study by Dall'Osto et al. (2017a) it is also shown that the NPF events and the growth of these aerosol particles to larger sizes can affect the CCN number concentration. Dall'Osto et al. (2017a) found an increase of the CCN number concentration (measured at a supersaturation of 0.4 %) of 21 % which was linked to NPF events. Within the NETCARE project based on summer time measurements in the Canadian Arctic Archipelago, high concentrations of newly formed particles were observed particularly in the marine boundary layer and above clouds (Burkart et al., 2017b). One particle growth event measured during NETCARE was described in Willis et al. (2016), showing newly formed particles growing to sizes above 50 nm, subsequently being able to activate to cloud droplets at 0.6% supersaturation. For the same project, Leaitch et al. (2016) examined cloud droplet number concentrations for 62 cloud samples and reported that particles with comparably small diameters, below 50 nm, activated to cloud droplets in 40% of all cases.

Besides the fact that aerosol particles need to have a certain size to act as CCN, also the aerosol particle chemistry matters in terms of the activation to a cloud droplet. The single hygroscopicity parameter κ (Petters and Kreidenweis, 2007) is commonly used to express the affinity of aerosol particles to water and characterizes their CCN activity. The hygroscopicity of the Arctic aerosol particulate matter (PM) was also found to show a seasonality. κ values determined from CCN measurements done on water soluble particulate matter collected in Spitzbergen by Silvergren et al. (2014) were between 0.3 and 0.7, with a minimum from March to May and a maximum in October. The past and future changes in the Arctic climate may cause changes of CCN number concentrations and their properties and consequently also to the sources and sinks of Arctic CCN. Hence there is a need for measurements in the Arctic region to quantify the CN and CCN number concentrations, their sources and sinks as well as the aerosol particle hygroscopicity.

The Antarctic region is particularly interesting for aerosol particle and CCN in situ studies for two reasons. Firstly, Antarctica is located far from anthropogenic activities and is one of the most pristine areas on the globe (Hamilton et al., 2014). Thus, it is a favorable environment for studying natural aerosol particle background conditions and processes that prevailed in a preindustrial atmosphere. A more accurate knowledge about preindustrial aerosol processes, conditions and properties, including aerosol-cloud interactions, is important for a reduction of uncertainties of model estimates concerning radiative forcing (Hamilton et al., 2014; Carslaw et al., 2013). Secondly, similar to the Arctic, the Antarctic region is extremely sensitive to climate change. Jacka and Budd (1998) analyzed surface

temperature data of 16 stations on the Antarctic continent and 22 stations on Southern Ocean islands and found warming rates of 0.9-1.2 °C and 0.7-1 °C, respectively. In particular in the West Antarctic and the Antarctic Peninsula the warming is several times higher than in other regions (Jacka and Budd, 1998; Vaughan et al., 2003; Kravchenko et al., 2011; IPCC, 2013). The Antarctic sea ice as well as the inland ice sheet are potentially subject to change in such a changing environment. However, at the moment, the Southern Hemisphere has not shown a decrease in sea ice extent. Cavalieri and Parkinson (2008) and Parkinson and Cavalieri (2012) even found an increasing annual maximum Southern Ocean sea ice extent. Both, the sea ice area and the open water area have the potential to emit aerosol particles into the atmosphere. Sea ice is a potential source for sea salt aerosol particles (Huang and Jaeglé, 2017; Yang et al., 2008; Wagenbach et al., 1998) and nitrogen (Dall'Osto et al., 2017b) and open sea water may emit sea spray aerosol and precursors for new particle formation (NPF) (Liss and Lovelock, 2008; Modini et al., 2015). Therefore, variations in sea ice coverage will likely lead to changes in the strength of aerosol particle sources. There are opposing trends in the ice sheet mass balance across Antarctica. Velicogna and Wahr (2006) and Shepherd et al. (2012, 2018) found that the ice sheets of West Antarctica and the Antarctic Peninsula had lost mass, whereas the East Antarctic ice sheet had gained mass. The gain of ice mass in East Antarctica is also confirmed by Martin-Español et al. (2017), however they found it to be smaller than losses in West Antarctica. As precipitation, which besides moisture is linked to the abundance of CCN and ice nucleating particles, is the only source of mass gain to the Antarctic ice sheet, it is necessary to study the properties of aerosol particles as well as their impact on cloud formation and precipitation, their sources, sinks and pathways in the changing environment of Antarctica.

Although Antarctica is a harsh environment where access for field work is difficult, various aerosol particle studies have been conducted at different Antarctic research stations during the last decades. A wide range of topics has already been investigated, including new particle formation (Koponen et al., 2003; Asmi et al., 2010; Kyrö et al., 2013; Fiebig et al., 2014; Weller et al., 2015), seasonal cycles of number and mass concentrations as well as size distributions (Koponen et al., 2003; Kim et al., 2017; Fiebig et al., 2014), chemical composition (Wagenbach et al., 1988; Teinila et al., 2000), hygroscopicity (Asmi et al., 2010; Kim et al., 2017; O'Shea et al., 2017) and optical properties of aerosol particles (Fiebig et al., 2014).

In general, there is a yearly trend in particle number concentrations, with maximum values in austral summer (Kim et al., 2017; Fiebig et al., 2014). Fiebig et al. (2014) conclude that these cycles are common across the Antarctic Plateau (including the Troll research station 235 km from the Antarctic coast but still 2000 km away from the South Pole), with free tropospheric air masses contributing to air detected at ground. The highest particle concentrations found in austral summer are frequently reported to be due to NPF events

(Asmi et al., 2010; Koponen et al., 2003; Kyrö et al., 2013; Weller et al., 2015; Kim et al., 2017). Particles formed during NPF events are likely related to sulfate and ammonia containing compounds that were found in the particulate phase in the submicron size range (Teinila et al., 2000; Wagenbach et al., 1988; Schmale et al., 2013). Precursor gases for NPF can originate from the Southern Ocean (e.g., DMS (dimethylsulfid), Weller et al., 2015; Schmale et al., 2013) and possibly also from e.g., cyanobacteria in freshwater melt ponds (Kyrö et al., 2013), microbiota from sea ice and the sea ice influenced ocean (Dall'Osto et al., 2017b) or the decomposition of excreta from fur seals, seabirds and penguins (Legrand et al., 1998; Schmale et al., 2013).

Newly formed particles were sometimes reported to grow to CCN size ranges at the Aboa research station, e.g., in Kyrö et al. (2013) and Koponen et al. (2003) (for the latter only in marine air masses), while Weller et al. (2015) report a maximum size of only 25 nm for particles grown from new particle formation for observations at the Neumayer research station. This difference was related to a difference in ground cover at the respective measurement sites, which was ice covered around Neumayer but featured melt ponds around Aboa (Weller et al., 2015).

Sodium chloride, supposedly from sea spray, was found in larger aerosol particle sizes (well above 100 nm) at Aboa, while the majority of particles was smaller than 100 nm (Teinila et al., 2000). A case of exceptionally high particle hygroscopicity, i.e., with a κ value of 1.13, was connected to air masses originating from a region with sea ice and open water at the coastal Antarctic research station Halley (O'Shea et al., 2017). Asmi et al. (2010) assumed that particles and nucleating and condensing vapors from the Southern Ocean contribute to particles observed at Aboa, and observed hygroscopic growth factors for particles of 25, 50 and 90 nm that were similar to those they reported for ammonium sulfate.

Furthermore, some studies have reported on Antarctic CCN properties, however the locations they cover are limited to the Antarctic Peninsula (DeFelice, 1996; DeFelice et al., 1997; Kim et al., 2017) or the area of the Weddell Sea on the Brunt Ice Shelf (O'Shea et al., 2017). Both locations are part of West Antarctica and especially the Antarctic Peninsula is mainly influenced by marine air masses that directly originate from the Southern Ocean. To create a more detailed picture of Antarctic CCN, further measurements that can be used to characterize CCN in the eastern and especially in the central part (inland plateau) of Antarctica, are needed.

To match the above outlined needs for CCN related measurements in the Arctic and on Antarctica, we carried out measurements in North-West Canada and at East Antarctica. The first data set presented in this thesis was recorded in the Arctic during the RACEPAC (Radiation-Aerosol-Cloud Experiment in the Arctic Circle) project, which took place in Inuvik (Canada) during April and May 2014. It was mostly an airborne campaign that

aimed to measure all components required to describe the interaction of aerosol particles, clouds and radiation in the Arctic. In this framework an additional ground based station in Tuktoyaktuk (≈ 130 km north of Inuvik) was installed and operated by the Max Planck Institute (MPI) for Chemistry to measure Arctic CCN and aerosol properties. The data set contains concentrations of condensation nuclei (CN) as well as of CCN, particle number size distributions (*PNSD*) measured at the station in Tuktoyaktuk and inferred particle hygroscopicity values (κ). Further a comparison of *PNSDs* measured at the ground based station and on the research airplane Polar 6, operated by the Alfred Wegener Institute for Polar and Marine Research (AWI, Germany), is presented.

The second data set that is part of this thesis contains measurements conducted at the Belgian Antarctic research station Princess Elisabeth (PE), in Dronning Maud Land. For three austral summer seasons (2013-2016, always from December to February) a Condensation Particle Counter (CPC), a Cloud Condensation Nucleus counter (CCNC) and a Laser Aerosol Spectrometer (LAS) were used to measure simultaneously aerosol particle and CCN properties inside the East Antarctic boundary layer. In addition, the present study introduces meteorological data, collected by an automatic weather station, as well as the history of the measured air masses, calculated by means of the Numerical Atmospheric-dispersion Modelling Environment (NAME) and the NOAA HYSPLIT trajectory model. This data set has enabled the study of the variability of the CN and CCN number concentrations, to identify their sources, sinks and transport pathways and to analyze the particle hygroscopicity during austral summer in East Antarctica. The special location of the PE station in the escarpment zone with catabatic winds coming from the Antarctic inland ice sheet, further allows an insight into the state of aerosol particle and CCN properties of continental Antarctica.

At the end of this introduction, I will now give a brief overview on the content of the following sections. In Section 2, the methods to measure the total particle number concentration, the *PNSD* and the number concentration of CCN are described. Further, it is explained how the particle hygroscopicity and the history and the origin of air masses were determined. In section 3, the results of the Arctic RACEPAC campaign and the measurements that were conducted at PE in Antarctica are presented and discussed. To end with, the summary of the most important results as well as conclusions and an outlook is given in chapter 4.

2. Experimental

2.1. Measured Properties

In this thesis physical properties of Arctic and Antarctic aerosol particles were determined, i.e., the total aerosol particle number concentration (N_{CN}), the aerosol particle number size distribution ($PNSD$) and the number concentration of cloud condensation nuclei (N_{CCN}) at different supersaturations (SS). The instruments that were used to measure N_{CN} , $PNSD$ and N_{CCN} are explained in the following sections and summarized in Table 2.1.

aerosol particle property	instrument
N_{CN} $d_{50} = 10 \text{ nm}$ $d_{50} = 3 \text{ nm}$ $d_{50} = 3 \text{ nm}$	CPC, TSI model 3010 CPC, TSI model 3776 CPC, TSI model 3025 (used in the SMPS system)
$PNSD$ $13.6 \text{ nm} < d_p < 736.5 \text{ nm}$ $90 \text{ nm} < d_p < 6.8 \mu\text{m}$	SMPS, TSI model 3936 LAS-X, TSI model 3340
N_{CCN} $0.1 \% < SS < 1 \%$	CCNC-100, DMT

Table 2.1.: **Instruments**

Overview about the instruments used for the thesis. d_{50} is the diameter at which 50 % of the particles are detected and d_p is the diameter of dry aerosol particles.

2.1.1. Total Particle Number Concentration

The number of aerosol particles that are contained in a certain volume of air is one of the most basic aerosol property. However, the measurement of this property is challenging because aerosol particles extend over a large size range from some nanometers up to hundreds of micrometers. To be able to optically detect aerosol particles down to sizes of some nanometers, they are enlarged via a vapor, condensing on their surface. The Condensation Particle Counters (CPC) applied in the framework of this thesis use butanol as a working fluid and are able to count single aerosol particles based on using a continuous flow principle.

First, the sampled aerosol particles are led into a heated saturator, where butanol is added

to the aerosol flow. In the following condenser the temperature is decreased, so that supersaturated butanol vapor condenses on the surface of the aerosol particles and forms droplets of several μm in diameter. A nozzle is used to focus the droplet flow, which is introduced into an optical detector. In the optical detector the enlarged droplets pass a laser beam, so that each single droplet creates a scattered light pulse that is detected by a photodiode. The known aerosol flow rate and the number of detected pulses give the final aerosol particle number concentration. This method, which was developed by Aitken in 1888, can be used to detect aerosol particles down to 3 nm in diameter. The lower detection limit is given by d_{50} , i.e., the diameter at which 50 % of the particles are detected. The measurements presented in this thesis were conducted using the TSI CPC model 3776 and 3025, both with a d_{50} of 3 nm and a TSI CPC model 3010 with a d_{50} of 10 nm.

2.1.2. Particle Number Size Distribution

An important physical property for the classification of aerosol particles is the aerosol particle size. As already mentioned above, aerosol particles span up a size range between a few nanometers and several micrometers. It is common to classify aerosol particles according to different modes. Figure 2.1 gives an overview about the modes, the processes and typical aerosol particle species that belong to the nucleation, Aitken, accumulation and coarse mode. A more detailed description of these modes, especially in terms of Arctic and Antarctic aerosol particles, is given in the introduction.

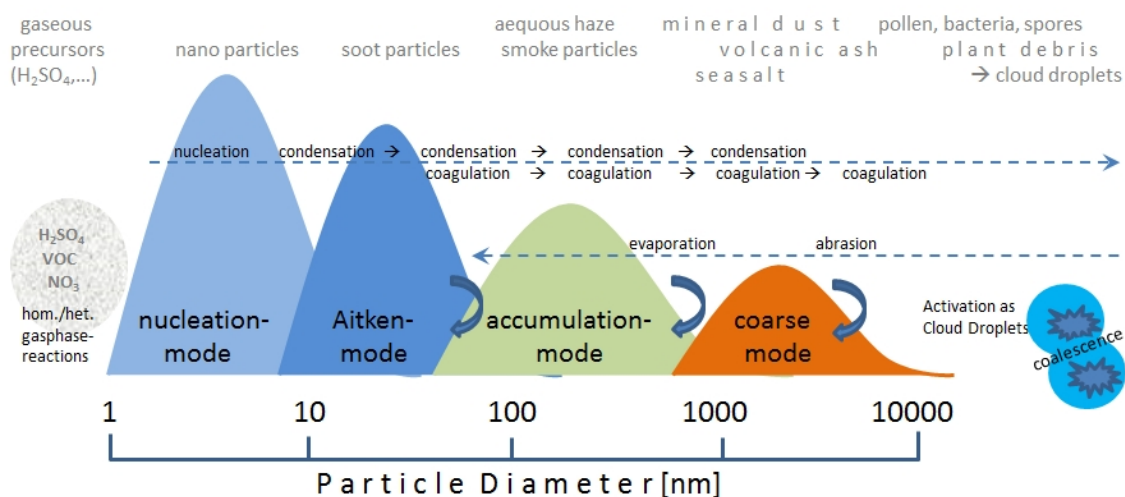


Figure 2.1.: **Aerosol particle modes**

Overview of the different aerosol particle modes including the processes and exemplary aerosol particle species for each mode. This picture is taken from Deutscher Wetterdienst (DWD): "Schematische multimodale Partikel-Größenverteilung mit typischen Transformationen beispielhaften Partikeltypen der einzelnen Moden." *reference: https://www.dwd.de/DE/forschung/atmosphaerenbeob/zusammensetzung_atmosphaere/aerosol/inh_nav/groessenverteilung.html* (last downloaded 21.02.2019).

To obtain a *PNSD* of an ambient aerosol sample the particle number concentration N of contiguous size bins needs to be measured. Usually the width of the size bins is not uniform, i.e., it differs for different instruments and often it increases with increasing diameter for measurements that are done with the same instrument. Hence, the resulting discrete *PNSD* usually looks uneven. In order to achieve an interpretable and comparable *PNSD*, N_i , the particle number concentration of a certain size bin i , is normalized by the width of the size bin i .

Most of the atmospheric aerosol particles are non spherical and irregular. To be able to categorize them in size bins, equivalent diameters are used. In the framework of this thesis two measurement techniques with different equivalent diameters were applied, i.e., a Scanning Mobility Particle Sizer (SMPS) and a Laser Aerosol Spectrometer (LAS) as well as an Ultra-High Sensitivity Aerosol Spectrometer (UHSAS), which select particles according to their electrical mobility diameter and optical diameter, respectively. The SMPS is described in detail in the next section followed by a section describing the similar working principle of the two optical aerosol particle sizers, the LAS and the UHSAS.

Scanning Mobility Particle Sizer - SMPS

The working principle of a SMPS system is based on the connection between the trajectory of a charged aerosol particle in an electrical field and the electrical mobility of the aerosol particle. The electrical mobility of an aerosol particle mainly depends on the aerosol particle size and its electrical charge. In this framework, knowing the electrical charge of an aerosol particle allows to determine its size. A SMPS can be used to measure the electrical mobility distribution, which can be converted to a *PNSD*. To measure *PNSDs* of ambient aerosol particles presented in this work a TSI SMPS model 3936 was used.

Figure 2.2 shows the schematic of the TSI SMPS model 3936, which works as follows. First, the polydisperse ambient aerosol sample is led through a neutralizer, which brings the aerosol particles to a defined bipolar charge equilibrium. This polydisperse aerosol enters a Differential Mobility Analyzer (DMA) together with an aerosol free sheath air flow. The DMA basically acts as a cylindrical electrical capacitor with an inner and an outer electrode. Different electrical charging states of the two electrodes create an electrical field in the analyzer column between the rods. The charged aerosol particles enter this analyzer column in perpendicular direction to the electrical field. The aerosol particles experience an electrostatic force, which accelerates the aerosol particles perpendicular to their initial trajectory. Aerosol particles that have the opposite charge of the inner wall move towards the center. Most particles impact on the inner rod, but particles with a selectable mobility can leave the analyzer column through a small sampling slit. At a specific voltage only aerosol particles with a certain electrical mobility catch the slit, so that the DMA output flow contains a quasi monodisperse aerosol sample. In the last step

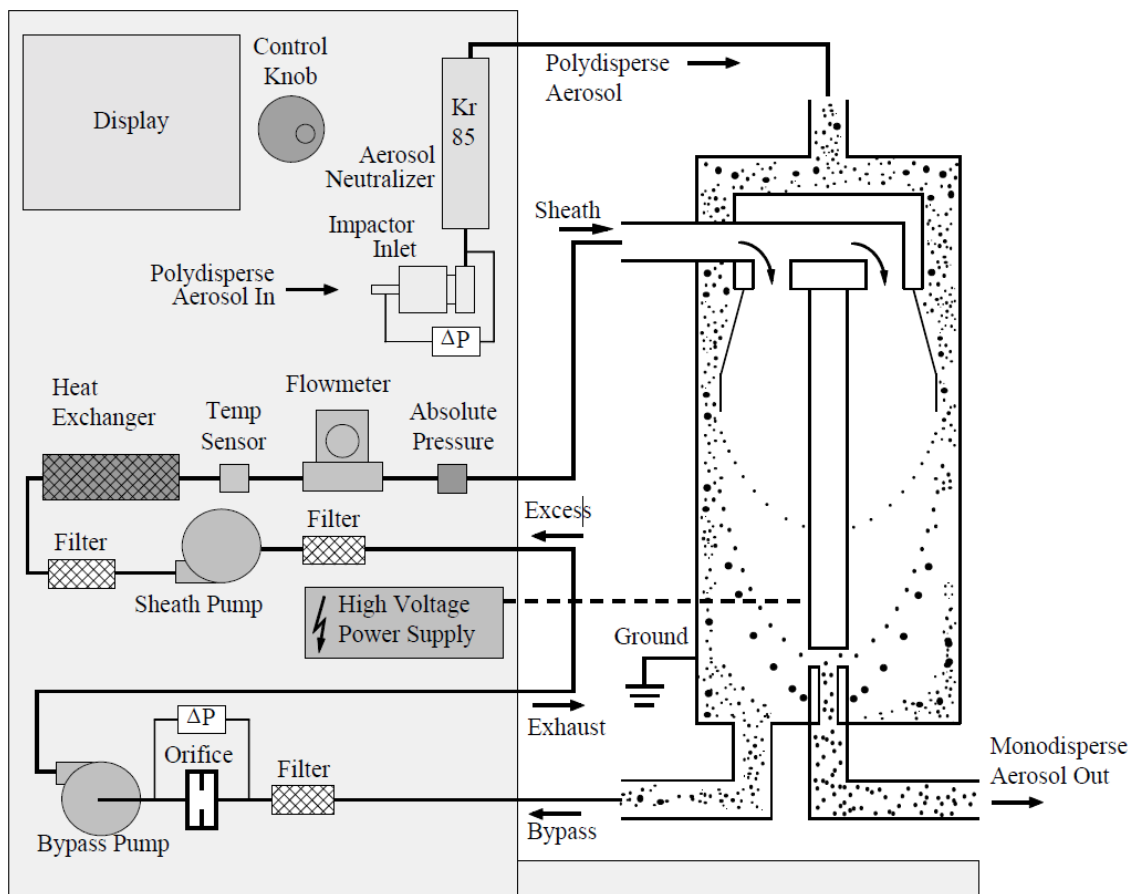


Figure 2.2.: **Schematic of the TSI SMPS model 3936**

A neutralizer charges the polydisperse aerosol particles that enter a DMA. The DMA selects the quasi monodisperse aerosol particles, that are counted by means of a CPC. The picture is taken from the TSI SMPS model 3936 manual (TSI, 2001). Original title: Schematic Flow Diagram of the Classifier with LDMA

the aerosol particle number concentration downstream of the DMA is measured by means of a CPC. In the SMPS mode this set-up continuously scans the voltage of the DMA, so that the electrical mobility and the aerosol particle number concentration is a function of time. This enables a high sampling rate i.e. a few minutes to scan the size range of some nanometers to one micrometer, which is an advantage for ambient measurements.

A further evaluation of the electrical mobility distribution has to be done by applying an inversion algorithm. The inversion algorithm contains a function that transfers the electrical mobility distribution to a size distribution (Knutson and Whitby, 1975), which is then corrected for multiply charged aerosol particles (Wiedensohler, 1988).

In this work the TSI SMPS model 3936 was used for measurements in the Arctic. It was equipped with a neutralizer model 3077A, a Long DMA model 3081 and a CPC model 3025, that was operated with a low flow rate. The aerosol and the sheath flow rate were 0.3 and 3 L/min, respectively, resulting in a flow ratio of 1 to 10. The ambient *PNSD* were measured for diameters from 13.6 nm up to 736.5 nm in 112 size channels (note, the

electrical mobility channels are log-distributed) with a time resolution of 5 minutes. Prior to the SMPS system an impactor with a cut off diameter of $1\ \mu\text{m}$ was used to minimize the fraction of multiply charged aerosol particles in the measured size range.

Optical aerosol particle sizers

The TSI LAS model 3340 and the DMT UHSAS used in this work are optical aerosol particle sizers with a similar working principle and set up. The main working principle is that the amount of electromagnetic radiation which is scattered by an aerosol particle within an active laser cavity strongly correlates with the particle size. The intensity of the scattered light is measured by a detector and can be transferred to an optical equivalent diameter. This optical equivalent diameter is the diameter of a sphere which would scatter the same light intensity than the aerosol particle. In the following, the theory of operation is explained on the basis of the LAS, however differences between the LAS and the UHSAS are mentioned.

Both instruments are composed of five subsystems: (1) a flow system, (2) an optical system, consisting of a laser and a detection system, (3) an analog as well as (4) a digital system and (5) a support PC. Figure 2.3 shows the schematic of the TSI LAS model 3340 flow system. The aerosol sample is introduced into a particle free sheath air flow. A nozzle is used to focus the aerosol particle sample stream to a diameter that is smaller than the laser beam diameter in order to avoid edge effects. The laser, that is in perpendicular orientation to the sample flow, is a Helium-Neon gas laser with a wavelength of 633 nm. The UHSAS is equipped with a solid state laser that emits light with a wavelength of 1054 nm. As aerosol particles cross the laser beam they scatter laser light pulses into the detection system. The detection system consists of two collection optics and two different photodiodes, an avalanche photodiode (APD) and a low gain positive intrinsic negative (PIN) photodiode. The APD and the PIN diode detect the lower and the upper size range of the aerosol particles, respectively. An analog and a digital electronic system amplify and convert the photocurrent of the detector photodiodes to a voltage and analyze the pulse height of each scattering event. The aerosol particle sizes, that are detectable due to this configuration range from 90 nm ($\geq 50\%$ detection efficiency) to $6.8\ \mu\text{m}$ for the LAS and from 60 nm ($\geq 50\%$ detection efficiency) to $1\ \mu\text{m}$ for the UHSAS. Differences in the detectable size ranges between the LAS and the UHSAS are due to differences in the amplification of the detected photocurrents. Both, the LAS and the UHSAS are equipped with an on-board PC to control the instruments.

In this work the LAS was operated with a sample flow rate of 0.07 L/min and with a sheath flow of 0.7 L/min. The UHSAS was operated with a sample flow rate of 0.05 L/min and with a sheath flow of 0.6 L/min. In both cases the *PNSD* was measured in 99 log-distributed channels.

The LAS was compared to a SMPS system (DMA type Medium Hauke; CPC, TSI

2.1. Measured Properties

model 3010) at the cloud laboratory of the Leibniz Institute for Tropospheric Research (TROPOS). 18 selected sizes (80, 90, 100, 110, 120, 130, 140, 150, 175, 200, 250, 300, 350, 400, 500, 600, 700, 800 nm) of ammonium sulphate particles and 4 sizes (100, 500, 700, 800 nm) of polystyrene latex (PSL) particles were used to validate the counts of the LAS. Necessary corrections with respect to the measured concentrations were high in the two LAS channels below 100 nm (around +70 %), distinct in the two channels around 100 nm (+ 10 %) and low in the other size ranges up to 800 nm (between 1 to 5 %, negative and positive corrections). These corrections were applied to the LAS data set used for this work.

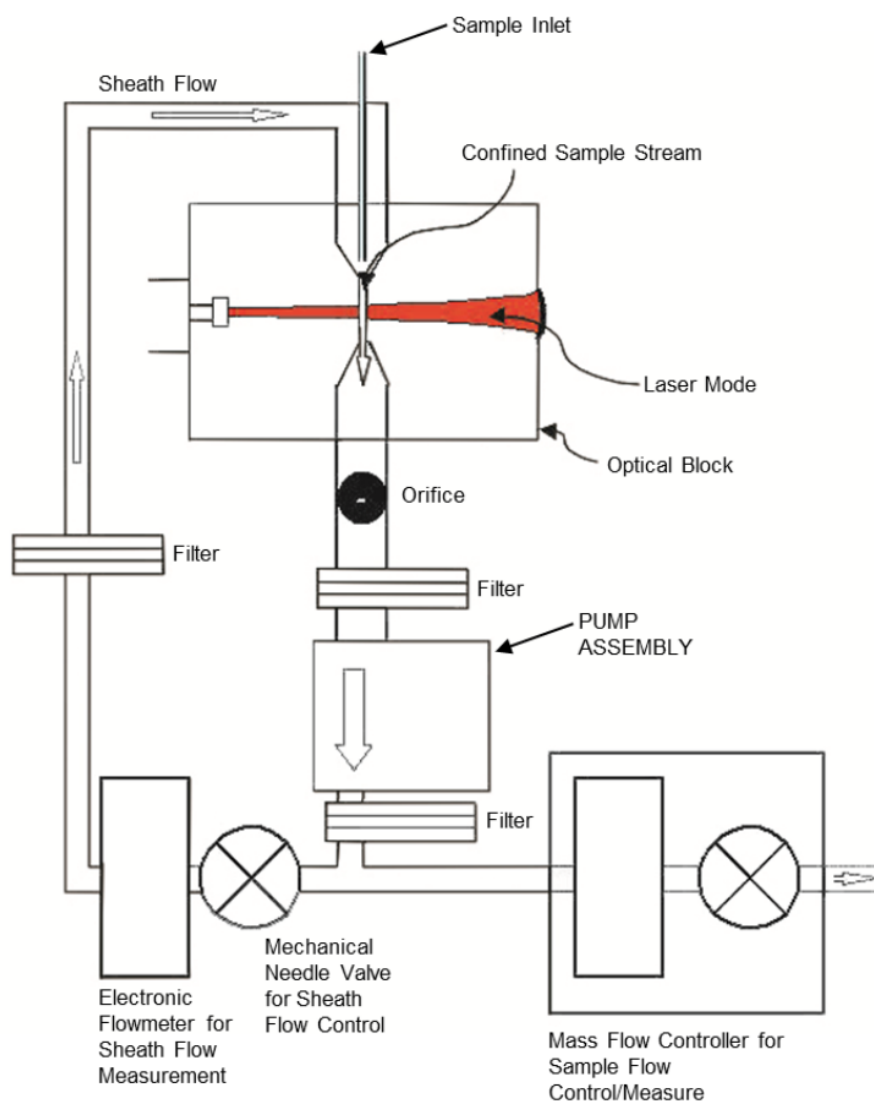


Figure 2.3.: **Schematic of the TSI LAS-X model 3340**

Schematic overview of the flow system of the TSI LAS-X model 3340. The picture is taken from the TSI LAS-X model 3340 manual (TSI, 2015). Original title: Schematic Diagram of Flow System

2.1.3. Total Concentration of Cloud Condensation Nuclei

Cloud Condensation Nuclei (CCN) are aerosol particles that have the ability to form cloud droplets. This activation process mainly depends on the size and the chemical composition of an aerosol particle as well as on the surrounding supersaturation (SS). The interaction of these properties is described by the Köhler theory (Köhler, 1936) and presented in Section 2.2.1. Measurements of the CCN number concentration presented in this work were all done with a CCN counter (CCNC) by Droplet Measurement Technologies (DMT) model 100 (Roberts and Nenes, 2005). It is a continuous-flow thermal-gradient diffusion chamber in which the SS can be varied to study the activation behavior of aerosol particles.

The main part of the CCNC is a 50 cm long ceramic tube in which a particle free sheath air flow and a centered aerosol particle flow pass through. How SS in the center of the flow tube is achieved can be explained when looking at Figure 2.4. The inner wall of the flow tube is continuously wetted with water and thus is at 100 % relative humidity (RH) with respect to water. Along the wall a temperature gradient is applied with an increasing temperature along the flow direction. Heat and water vapor diffuses to the center of the flow tube. As water molecules are smaller and lighter than air molecules (mainly O₂ and N₂) water vapor diffuses faster than heat. Figure 2.4 shows how the heat and the water

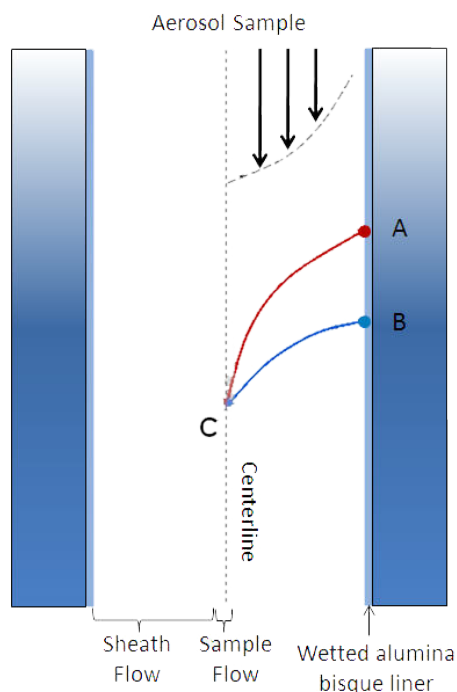


Figure 2.4.: **Working principle of the DMT CCNC-100**

Cross-section of the CCNC flow tube. SS at the center line of the flow tube is achieved due to the different speed of the water vapor and heat diffusion from the wetted wall to the center. This picture is taken from the CCNC manual for single-column CCNCs (DMT, 2012). Original title: Supersaturation Being Generated in the CCN Colum

vapor at point C on the center line originates from point A and B at the wall, respectively. From the fact that the temperature at point B is higher than at point A and both have a RH of 100 % follows, that the saturation vapor pressure with respect to water $e_{s,w}$ at point B is larger than at point A. Hence, at point C we have $e_{s,w}$ of point B but only the lower temperature of point A, which leads to a supersaturated environment at the center line. The SS at the center line can be adjusted via the temperature gradient along the wall of the flow tube. A higher temperature gradient leads to a higher SS. In the supersaturated environment of the center line, water vapor condenses on the surface of aerosol particles and can activate them to droplets. Downstream of the chamber an optical particle counter (OPC) detects all particles as CCN that are larger than $1 \mu\text{m}$ in diameter.

In this work the CCNC was operated with an inlet flow rate of 0.5 L/min, that splits into a sample and sheath flow of 0.05 L/min and 0.45 L/min, respectively. The CCNC was operated as recommended in Gysel and Stratmann (2013) for polydisperse CCN measurements. The ambient CCN measurements presented in this work were done at a SS of 0.1 %, 0.2 %, 0.3 %, 0.5 % and 0.7 %. Measuring each SS for 12 minutes lead to one data point per SS per hour. The data processing procedures differ for the two CCN data sets presented in this work and are explained in the corresponding sections (3.1.1 and 3.2.1). The SS-calibration of the CCNC was done at the home laboratory of the Leibniz Institute for Tropospheric Research. The procedure is described in the Appendix A.1.

2.2. Determination of the CCN hygroscopicity

The formation of cloud droplets on the surface of an aerosol particle is described by the Köhler theory (Köhler, 1936) and mainly depends on the properties of the aerosol particle and the surrounding SS. Petters and Kreidenweis (2007) introduced a modified version of the Köhler theory, in which the single hygroscopicity parameter κ represents the chemical composition of the aerosol particle. Applying the κ -Köhler theory, N_{CCN} and $PNSD$ measurements can be used to infer κ of ambient aerosol particles. In the following section the Köhler theory is shortly summarized followed by a presentation of the κ -Köhler theory and its application to infer the κ values presented in this work.

2.2.1. Köhler theory

The Köhler theory describes the equilibrium between a deliquesced aerosol particle and its surrounding water vapor up to the point at which an aqueous solution droplet is activated to a cloud droplet. This theory is based on two effects that are described by the Kelvin equation and Raoult's law and can be summarized according to Seinfeld and Pandis (1998) as follows.

The saturation of air with respect to water S_w is defined by the ratio of the water vapor

2. Experimental

pressure e_w to the saturation water vapor pressure $e_{s,w}$

$$S_w = \frac{e_w}{e_{s,w}} \quad (2.1)$$

$$SS_w = RH_w - 100 = (S_w - 1) \cdot 100. \quad (2.2)$$

If S_w is given in percent, it becomes the relative humidity RH_w which subtracted by 100 gives what is termed as supersaturation (SS) throughout the whole work. The Köhler theory expresses the saturation ratio S_w over the surface of a solution droplet with the diameter D as follows:

$$\ln S_w = \frac{A}{D} - \frac{B}{D^3} \quad (2.3)$$

with

$$A = \frac{4M_w\sigma_s/a}{RT\rho_w} \quad (2.4)$$

and

$$B = \frac{6M_w n_s}{\rho_w \pi}, \quad (2.5)$$

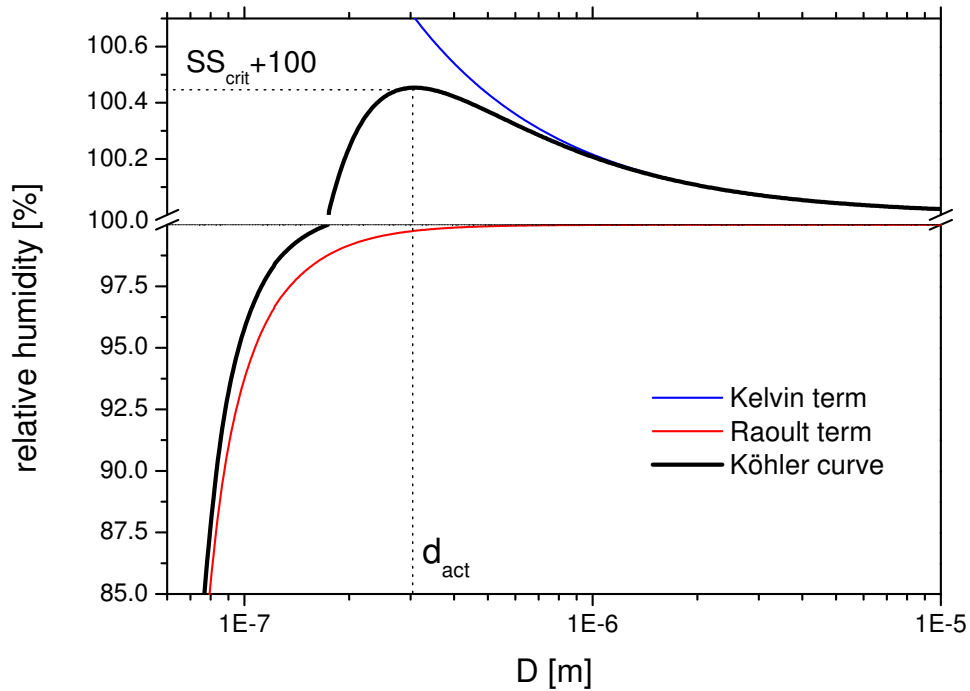


Figure 2.5.: **Köhler curve of an ammonium sulphate particle**

Köhler curve, Kelvin term and Raoult term calculated with the Köhler equation 2.3 for an ammonium sulfate particle with a dry diameter of 50 nm.

where M_w and ρ_w are the molar mass and density of water, while R and T are the ideal gas constant and the absolute temperature, respectively. $\sigma_{s/a}$ is the surface tension of the solution droplet and n_s the number of moles of the solute. The Köhler equation expresses the influence of the Kelvin effect (first term in Equation 2.3) and the Raoult effect (second term in Equation 2.3) on the vapor pressure over the surface of a solution droplet. The Kelvin effect is a surface effect which states that the vapor pressure over a curved surface is larger than over a flat surface, i.e., the vapor pressure decreases with increasing D . In contrast to this, the Raoult effect is a volume effect stating that the vapor pressure increases with increasing D as the solution droplet becomes more diluted due to water vapor condensing on its surface. Figure 2.5 shows an example of the Köhler curve, the Kelvin term and the Raoult term for an ammonium sulfate particle with a dry diameter of 50 nm. The combination of the competing surface and volume term results in a maximum of the saturation ratio in the Köhler curve with a corresponding critical activation diameter d_{act} and a critical saturation ratio SS_{crit} . A solution droplet that grows up to this point gets activated and becomes a cloud droplet.

The supersaturation adjusted in the CCNC for N_{CCN} measurements presented in this work is equivalent to SS_{crit} of the Köhler curve. All particles that are measured as a CCN reached d_{act} in the measurement column of the CCNC and got activated to cloud droplets.

2.2.2. The hygroscopicity parameter κ and the critical diameter d_{crit}

The κ -Köhler theory (Petters and Kreidenweis, 2007) is a parametrization that expresses the Raoult term of the Köhler theory with the single hygroscopicity parameter κ . The κ value simply is an expression of the affinity of a material for water. Based on Petters and Kreidenweis (2007) the κ values for ambient aerosol particles reported in this study were calculated as follows, assuming the surface tension of the examined solution droplets ($\sigma_{s/a}$) to be that of pure water:

$$\kappa = \frac{4A^3}{27d_{crit}^3 \ln^2 S_w} \quad (2.6)$$

where d_{crit} is the critical dry particle diameter at which a particle is just large enough to be activated to a cloud droplet when exposed to a certain saturation ratio. Assuming that all particles have an identical chemical composition, i.e., the aerosol particles are internally mixed, and no aerosol particle interactions take place the κ value of these particles can be seen as a volume fraction weighted average κ :

$$\kappa = \sum_i \varepsilon_i \kappa_i \quad (2.7)$$

with κ_i and ε_i representing the hygroscopicity and the volume fraction of an individual

chemical species.

This average κ value of an ambient aerosol particle sample can be inferred by determining d_{crit} from simultaneously N_{CCN} and $PNSD$ measurements. d_{crit} is the diameter at which N_{CCN} is equal to the value of the cumulative $PNSD$, with the integration being done from the largest measured diameter of the $PNSD$ to lower diameters. The connection between the $PNSD$, a corresponding N_{CCN} and the resulting d_{crit} is exemplified in Figure 2.6. The derived d_{crit} can then be used, together with the corresponding S_w (i.e., the calibrated SS at which N_{CCN} was measured) to derive κ for the ambient particles, based on Equation 2.6. The inferred κ values correspond to particles with sizes of roughly d_{crit} . The uncertainty in κ which results from the uncertainties of the $PNSD$ measurements and the SS of the CCNC, was determined by applying a Monte Carlo simulation in a similar fashion as done by Kristensen et al. (2016). A detailed description of this method is given in Appendix A.2.

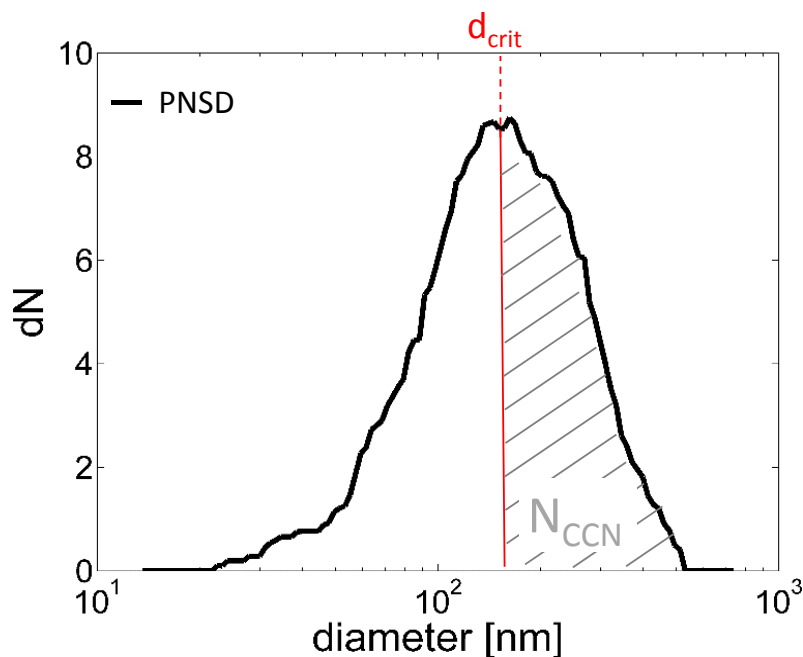


Figure 2.6.: **Determination of d_{crit}**

The critical diameter d_{crit} is determined by the integration of a $PNSD$ starting from the largest diameter til it is equal to the value of a simultaneous measured N_{CCN} .

For atmospheric particles, κ can range between almost 0 for insoluble (e.g. soot and some organics) and 1.4 for very hygroscopic (e.g. sodium chloride) particles (Petters and Kreidenweis, 2007). A generally good estimate for a continental κ of around 0.3 is given by Andreae and Rosenfeld (2008). Wex et al. (2010) report that the hygroscopicity of marine aerosol particles can cover a broad range from κ values below 0.1 up to above 1, with a dominating κ value of 0.45.

2.3. Determination of the Air Mass Origin

One major goal of this thesis was to investigate the connection between the air mass history and N_{CN} and N_{CCN} properties as well as to identify regions that have the potential to act as a source region for aerosol particles and CCN. For this purpose air mass back trajectories were calculated by means of the LAGRANTO Lagrangian analysis tool, the NAME atmospheric dispersion model and the NOAA HYSPLIT trajectory model. The LAGRANTO backward trajectories were used to perform a simple analysis of the air mass history i.e., to visualize the track of the air masses back in time for the Arctic data set (Section 3.1.3). In contrast to this the air mass back trajectories of the NAME atmospheric dispersion model and the NOAA HYSPLIT trajectory model were used to apply a more advanced residence time analysis and the Potential Source Contribution Function (PSCF), respectively. The residence time analysis based on the NAME dispersion model was performed for the Antarctic data set, whereas the PSCF model was used for both, the Arctic and Antarctic data set. The following two sections explain the residence time analysis and the PSCF model in detail.

2.3.1. The NAME Dispersion Model

The atmospheric dispersion model NAME (Jones et al., 2007) is a Lagrangian particle-trajectory model that is operated by the UK Meteorological Office. For the data presented

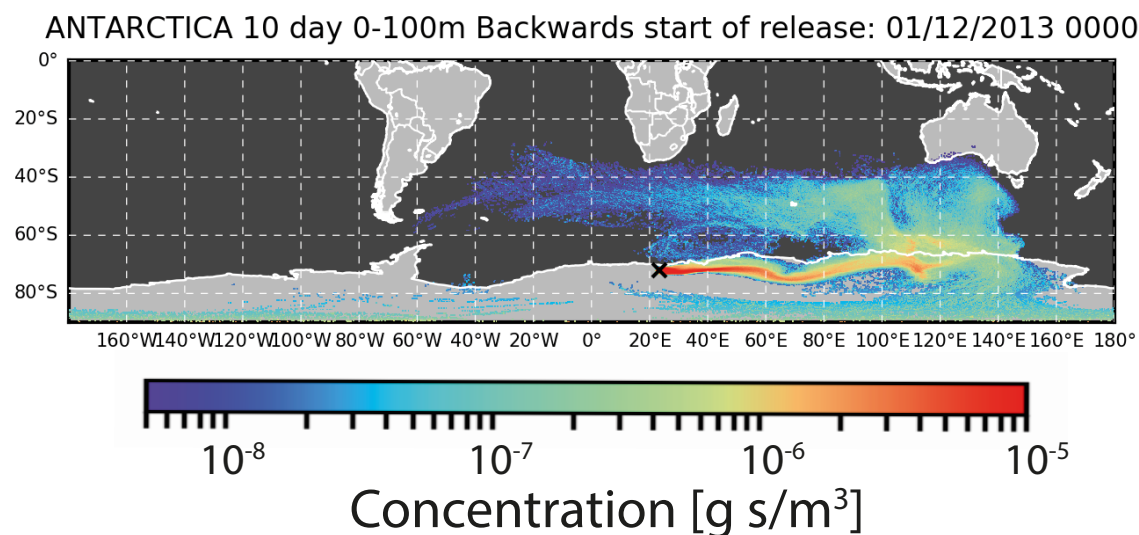


Figure 2.7.: **NAME footprint**

NAME dispersion model 10 day backwards footprint. The color indicates the concentration of the released particles in the surface layer (0-100 m) in each grid box over the integrated time of 10 days (this results in the unit g s/m^3) and the cross displays the location of the Princess Elisabeth research station in Antarctica.

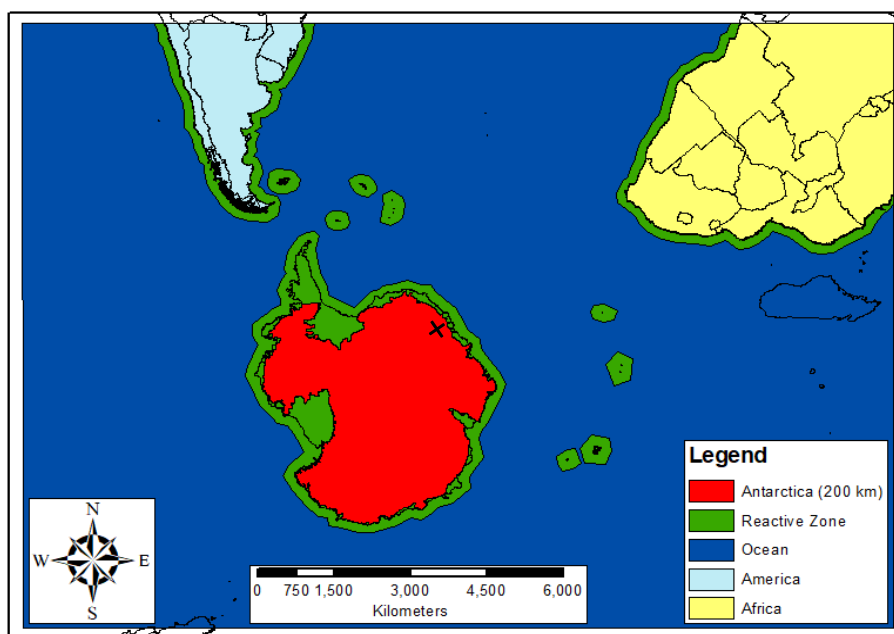


Figure 2.8.: **NAME regional analysis**

5 different regions (Antarctic inland plateau, Southern Ocean, Reactive Zone, South America and Africa) that are used to track the percentage residence time in each region before arriving at PE from the NAME footprints.

in this thesis 10000 abstract particles per hour were released at an altitude of 10 m above the location of the Princess Elisabeth research station in Antarctica. On the basis of the Meteorological Office Unified Model (UM) meteorological field data, 10-day back trajectories for these particles were calculated. Summing up the concentration of these particles at time steps of 15 minutes back in time (in total 960 time steps) results in a footprint that shows the history of the air masses during the last 10 days. For this procedure only particles that are located within the surface layer (0-100 m) are taken into account. An example footprint of the first of December 2013 (midnight) is shown in Figure 2.7. Footprints were derived every three hours, resulting in a total number of 2019 NAME footprints used in this study. To further analyze the impact of different surface properties on the measured aerosol particle properties, the area around Antarctica was divided into the following 5 different regions (see also Figure 2.8): the Antarctic inland plateau (continental area at or above 200 m above the sea surface level), Southern Ocean, South America, Africa and Reactive Zone. The Reactive Zone includes the following regions that are known to have the potential to emit either primary particles or precursors for secondarily formed particles:

- The Antarctic continental area below 200 m above the sea surface level and 8 islands in the Southern Ocean (South Georgia, South Sandwich, Falkland, South Orkney, Prince Edward, Crozet, Kerguelen, Heard and McDonald Island). These regions are included because they are habitats for numerous different types of penguins. Bird guano (Croft et al., 2016b) and in this special case penguin guano (Legrand et al.,

1998), acts as a source of ammonia and may contribute to the formation of new particles in coastal Antarctic areas.

- The permanent and seasonally covered sea ice areas. These are known to have the potential to act as source of organic nitrogen that contributes to secondarily formed aerosol particles (Dall'Osto et al., 2017b) or to emit primary sea salt particles (Huang and Jaeglé, 2017; Yang et al., 2008; Wagenbach et al., 1998).
- The marine area up to 200 km from the coasts of the islands and continents (for Antarctic, continent plus ice shelves). These areas are included due to an enhanced chlorophyll concentration in the coastal areas of the Southern Ocean. Chlorophyll can be used as a proxy for dimethyl sulfide (DMS) (Vallina et al., 2006), which in turn plays a role in new particle formation (Liss and Lovelock, 2008).

The proportional residence time that the air masses spent over the 5 different regions during the last 10 days was determined in order to assess to what extent these regions influence the aerosol particle and CCN properties. This type of a residence time analysis was already used for an Antarctic site by O'Shea et al. (2017).

2.3.2. Potential Source Contribution Function

The Potential Source Contribution Function (PSCF) is a receptor modeling method that originally was developed by Ashbaugh et al. (1985). It is one of the most used receptor modeling methods and it was applied in several studies before that cover a wide range of geographical scales and also include high latitude regions e.g., Dall'Osto et al. (2017b) (Antarctic) and Yli-Tuomi et al. (2003) (Arctic). The PSCF model, that is commonly used to identify regions that have the potential to contribute to high values of measured concentrations at a receptor site, is based on air mass back trajectories. In the framework of this thesis the PSCF analysis is applied to identify regions that contribute to high N_{CN} and N_{CCN} values and thus can be considered as potential source regions.

To apply the PSCF analysis the NOAA HYSPLIT trajectory model (Stein et al., 2015) was used to calculate hourly resolved 10-day back trajectories based on $1 \times 1^\circ$ GDAS (Global Data Assimilation System) meteorological data. To account for uncertainties in back trajectory analysis it is a common procedure to increase the number of back trajectories by varying the initial conditions. In this work the position of the receptor location was varied in the following way. Back trajectories were calculated at three different altitude levels, i.e., 100 m, 200 m and 300 m above the surface level, and at 5 different plane locations, i.e., one exactly at the location where the measurements were conducted and 4 in close proximity around it by adding and subtracting 0.25° . This results in a set of 15 back trajectories per time step. Each back trajectory consists of trajectory segment endpoints, which represent the central geographical position of the air parcel at a particular time. To

calculate the PSCF the whole region that is covered by these trajectory segment endpoints is divided into an array of 5x5 degree grid cells (i,j). The approach is that aerosol particles that are emitted in such a cell can be incorporated into the air parcel and are transported to the receptor site. The PSCF can be calculated as follows:

$$PSCF_{i,j} = \frac{m_{i,j}}{n_{i,j}}, \quad (2.8)$$

where $n_{i,j}$ is the total number of trajectory segment endpoints that fall into a cell and $m_{i,j}$ is the number of trajectory segment endpoints that fall into a cell and exceed a given criterion value. In this thesis the 75 % percentile is used as threshold.

According to Hopke (2016): “Cells containing emission sources would be identified with conditional probabilities close to 1 if trajectories that have crossed the cells effectively transport the emitted contaminant to the receptor site. The PSCF model thus provides a means to map the source potentials of geographical areas. It does not apportion the contribution of the identified source area to the measured receptor data.” As it is probable that small values of $n_{i,j}$ would lead to uncertain and high PSCF values it is necessary to apply a weighting function. For this study a discrete weighting function based on $\log(n + 1)$, which is a measure of the back trajectory density, was applied (Waked et al., 2014):

$$W = \begin{cases} 1.00 & \text{for } n_{i,j} > 0.85 \cdot \max(\log(n + 1)) \\ 0.725 & \text{for } 0.6 \cdot \max(\log(n + 1)) < n_{i,j} \leq 0.85 \cdot \max(\log(n + 1)) \\ 0.35 & \text{for } 0.35 \cdot \max(\log(n + 1)) < n_{i,j} \leq 0.6 \cdot \max(\log(n + 1)) \\ 0.1 & \text{for } 0.35 \cdot \max(\log(n + 1)) > n_{i,j} \end{cases} \quad (2.9)$$

The measured concentration of total particles and CCN is also affected by losses that occur along the path of the air parcel between the source and the receptor site. As precipitation, which is known to be one of the major sinks for aerosol particles, in particular for CCN, is an output parameter of the calculated NOAA HYSPLIT back trajectories, it can be taken into account. Hence, the PSCF model was run with a precipitation filter. Back trajectories were cut off, and not considered for the PSCF analysis, as soon as a trajectory segment endpoint shows a precipitation of 0.1 mm/h and the total precipitation (sum of precipitation of 240 segment endpoints) of this back trajectory exceeds a value of 5 mm/10d. The second criterion was added as it seemed not to be reasonable to discard a trajectory only because of showing a low precipitation of some mm/h at some segment endpoints. Note, the filter criteria as well as the criteria of the weighting function are empirical.

3. Results and Discussion

3.1. Measurements of aerosol and CCN properties in the Mackenzie River delta (Canadian Arctic) during Spring-Summer transition in May 2014

3.1.1. Campaign overview

The data set presented in this section was recorded during the RACEPAC (Radiation-Aerosol-Cloud Experiment in the Arctic Circle) project, which took place in Inuvik during April and May 2014. It was mostly an airborne campaign that aimed to measure all components required to describe the interaction of aerosol particles, clouds and radiation in the Arctic. In this framework an additional ground based station in Tuktoyaktuk (≈ 130 km north of Inuvik) was installed by the Max Planck Institute (MPI) for Chemistry where measurements used in this thesis were made, aiming at providing a basic characterization of the Arctic aerosol particle and CCN properties. The data set presented here contains concentrations for condensation nuclei (CN) as well as for CCN, particle number size distributions (*PNSD*) and inferred particle hygroscopicity values (κ) measured at the station in Tuktoyaktuk. Further a comparison of *PNSDs* measured at the ground based station and on the research airplane Polar 6, operated by the Alfred Wegener Institute for Polar and Marine Research (AWI, Germany), is presented.

Measuring site and meteorology

Tuktoyaktuk is a town of less than 1000 inhabitants in the Inuvik Region of the Northwest Territories, Canada. Figure 3.1 shows a map of Alaska and the western part of Canada together with the Sea Ice extent layer and the Corrected Reflectance layer of MODIS (Moderate Resolution Imaging Spectroradiometer). Tuktoyaktuk is situated north of the Arctic circle ($69^\circ 26'$ N and $133^\circ 01'$ W) on the shore of the Beaufort Sea and 5 m above sea level. The area around Tuktoyaktuk has a low population density. The Beaufort Sea is located directly to the north of Tuktoyaktuk, and it is typically covered with ice from October to June. The pink color in Figure 3.1 shows the extent of the sea ice on the 15th of May 2014. The area of the frozen sea surface covers the entire Beaufort Sea and extends to the south to the Bering strait. Hence, it can be excluded that aerosol particles of

3.1. Measurements of aerosol and CCN properties in the Mackenzie River delta (Canadian Arctic) during Spring-Summer transition in May 2014

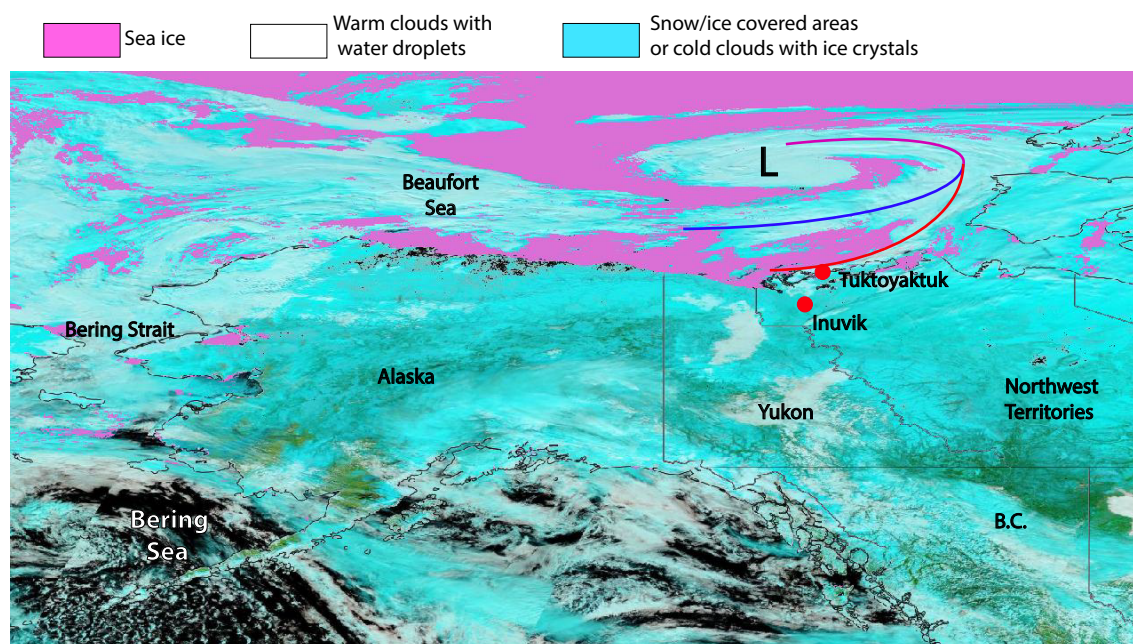


Figure 3.1.: **RACEPAC - overview map**

Map of Alaska and the western part of Canada showing the position of Tuktoyaktuk and Inuvik together with two additional layers of the MODIS instrument (installed on TERRA, NASA). The Sea Ice extent layer shows the frozen ocean surface in pink. The Corrected Reflectance (Bands 7,2,1) layer shows liquid water in dark blue or black. Ice on the surface or in form of ice crystals in cold clouds will appear turquoise whereas small water droplets in warm clouds will appear white. A low pressure system, which was relevant for the measurements in Tuktoyaktuk, and its corresponding fronts are marked. The map was created for the 15th of May 2014 using NASA Worldview [reference:https://worldview.earthdata.nasa.gov/?map=-126.907471,36.373535,-117.415283,42.815918&products=baselayers,MODIS_Aqua_CorrectedReflectance_TrueColor~overlays,MODIS_Fires_All,sedac_bound&time=2012-08-23&switch=geographic](https://worldview.earthdata.nasa.gov/?map=-126.907471,36.373535,-117.415283,42.815918&products=baselayers,MODIS_Aqua_CorrectedReflectance_TrueColor~overlays,MODIS_Fires_All,sedac_bound&time=2012-08-23&switch=geographic)

marine origin are formed locally during the measuring period. The landscape surrounding the measurement station is comprised by flat Arctic tundra with a subarctic climate. The characteristic precipitation is less than 300 mm per year and the mean annual surface temperature is below 0°C.

The time series of the meteorological parameters temperature, relative humidity, pressure, wind speed and wind direction (Figure 3.2) give an overview with respect to the ambient weather conditions during the whole sampling period. The measured temperature shows an increasing trend typical for the transition from Arctic spring to summer. This transition is driven by the increase of the daily incoming solar radiation and leads to a change in sea ice and snow cover and consequently also to a change of Arctic aerosol particle sources. During this transition from spring to summer, the polar front is moving towards the north resulting in a more frequent passage of low pressure systems as well as enhanced dynamics and mixing in the boundary layer of subarctic areas. This can be seen in the high variability of the measured temperature (from -10°C up to 15°C) and the relative humidity (from 45% up to 95%). Furthermore, sharp changes in all meteorological parameters

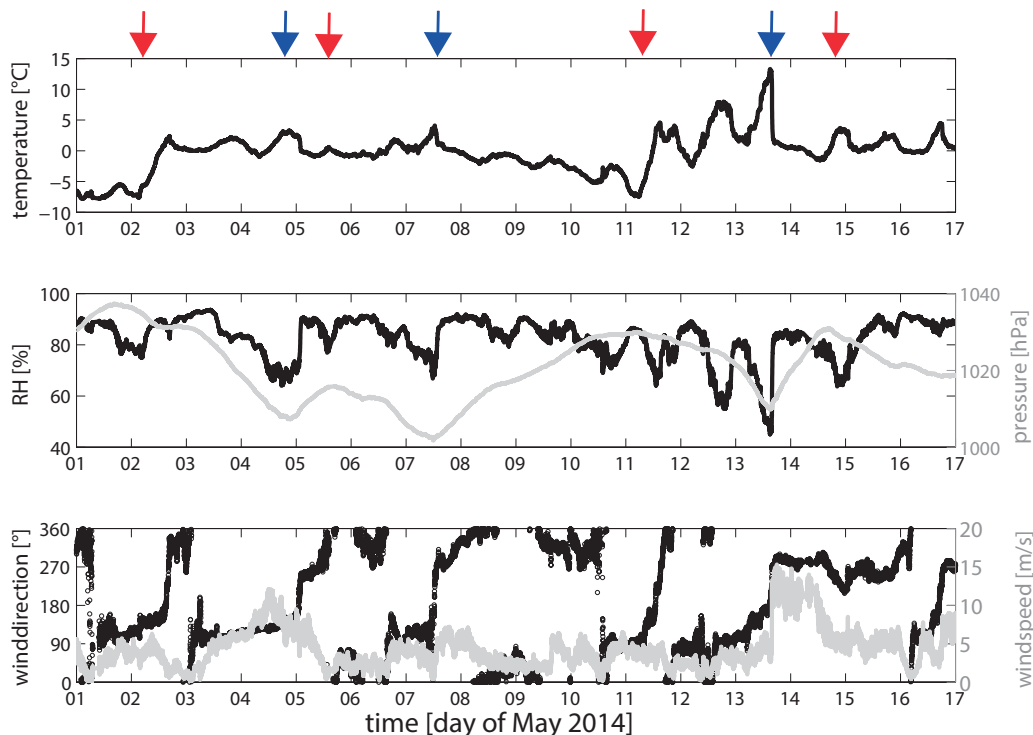


Figure 3.2.: **RACEPAC - time series of meteorological parameters**

Time series of temperature, pressure, relative humidity as well as wind speed and direction measured directly at the aerosol inlet at an altitude of 3.5 m above ground level covering the entire measurement period in May 2014. The passages of cold and warm fronts are marked with blue and red arrows, respectively.

indicate the passage of local low pressure frontal systems (e.g. the pressure drop and the wind shift at the 13th of May that correspond to a cold front. Cold and warm fronts are marked with blue and red arrows in Figure 3.2, respectively, indicating a fast air mass change. In Figure 3.1 a low pressure system, which was located over the Beaufort Sea, is visible due to the Corrected Reflectance layer. The corresponding warm front is also visible in the meteorological parameters of Figure 3.2.

Instrumentation and data processing

The experimental setup used to conduct the ground based measurements during the campaign is shown in Figure 3.3. An aerosol inlet with a PM_{10} sampling head was installed on top of a measurement container at a height of 3.5 meter above ground level. Along a vertical tube (inner diameter of 2.5 cm) the aerosol was transported into the measurement container. Downstream horizontal tubes (inner diameter of 1 cm and 0.53 cm) distributed the aerosol to the instruments.

The total aerosol particle number concentration (N_{CN}) was measured by a Condensation Particle Counter (CPC, TSI Model 3010) which was operated at a total flow rate of

1 l/min. In parallel the particle number size distribution was measured by means of a Scanning Mobility Particle Sizer (SMPS, TSI model 3936 with CPC Model 3025). Upstream of the SMPS an impactor with 1 μm cutoff diameter was installed and prior to the CPC and the SMPS the aerosol was dried using a diffusion dryer with silica gel. Airborne *PNSD* measurements on board of the Polar 6 research aircraft were conducted by means of an Ultra-High Sensitivity Aerosol Spectrometer (UHSAS) that measured in a size range from 70 nm up to 1 μm .

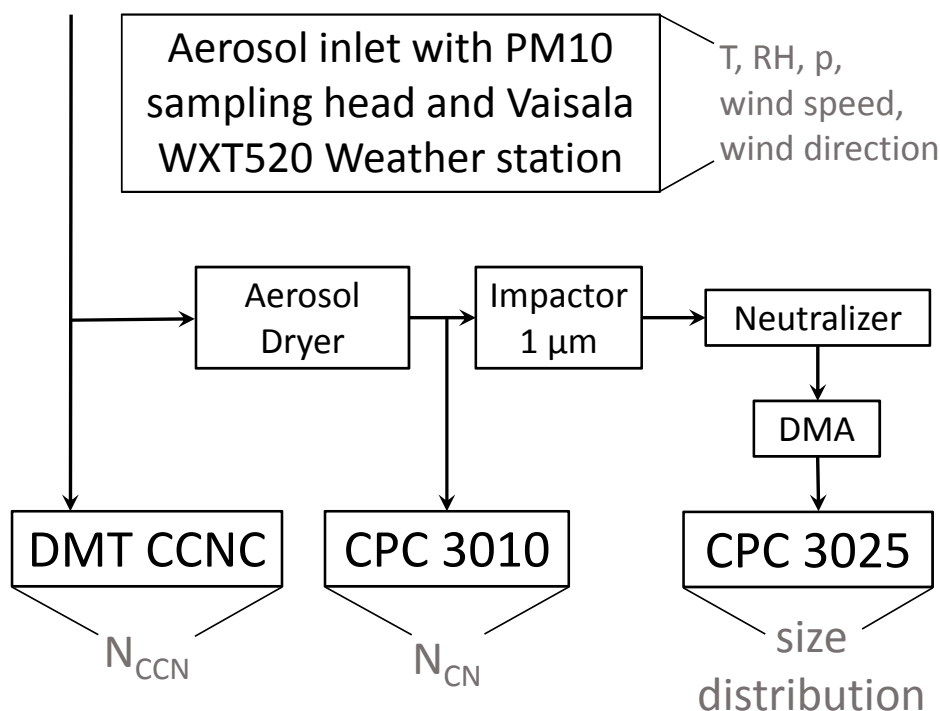


Figure 3.3.: **RACEPAC - measuring set up**

Schematic depiction of the measuring set-up implemented in the Tuktoyaktuk ground based (container) station.

The number concentration of cloud condensation nuclei (N_{CCN}) was measured using a Cloud Condensation Nuclei counter (CCNC, Droplet Measurement Technologies (DMT), Boulder, USA). By stepping the temperature gradient every 12 minutes the supersaturation (SS) was varied between 0.1 %, 0.2 %, 0.3 %, 0.5 % and 0.7 %. To ensure stable column temperatures, the first 5 min and the last 30 sec at each SS setting were excluded from the data analysis. The remaining data points were averaged.

Ground based measurements of N_{CN} , N_{CCN} and *PNSD* were contaminated due to local particle sources, so that a filter routine had to be applied, which will shortly be described in the following. The filter completely removes data points at time periods during which the pollution occurred. N_{CN} is the parameter that is most sensitive to the pollution since it was detected with the lowest time resolution (1 s) and pollution occurred in a size range

smaller than 150 nm in diameter, which is covered by the CPC-3010. Pollution events were identified due to a fast (some seconds) and intensive increase of N_{CN} , which is well visible in the N_{CN} time series (Figure 3.4) presented in the following section. The gradient in the N_{CN} time series was used as a filter criterion. Peaks that occurred due to local pollution events could be identified best by searching for an absolute gradient between two N_{CN} measuring points of at least $\pm 20 \text{ cm}^{-3} \text{ s}^{-1}$. For further analysis, N_{CCN} and $PNSD$ that were measured in a time span of 400 s before and after a pollution peak occurred were neglected. The 400 s originated from the sampling frequency of N_{CCN} (400 s) and $PNSD$ (300 s).

During the measurement period technical problems occurred with the CPC-3025 which was a part of the SMPS system. This resulted in a non-uniform consistency between N_{CN} measured with the CPC-3010 and the N_{CN} of the integrated $PNSD$ measured with a CPC-3025. Hence, the $PNSDs$ were variably corrected so that the integrated total number concentration was consistent with N_{CN} measured with the CPC-3010.

3.1.2. Overview of N_{CN} , N_{CCN} and $PNSD$ data for the entire measurement period

The measurements of all aerosol parameters recorded during the RACEPAC-campaign were temporarily influenced by local anthropogenic sources. Local emissions from ground based sources such as industrial combustion, oil heating and the generator for the container power as well as occasional air traffic led to intensive short term peaks in the measured time series of N_{CN} , N_{CCN} at SS above 0.1 % and the $PNSDs$.

The gray line in Figure 3.4 shows the time series of the measured raw total aerosol particle number concentration, where it will be referred to these data using the parameter N_{CNraw} . Beside a clear baseline of concentrations between less than 100 and 1000 cm^{-3} , peaks up to more than 10000 cm^{-3} occur during the whole sampling period. These peaks had a typical temporal duration of 1 to 5 minutes. Consequently, the first step of the data analysis was the application of a filter routine to eliminate time periods where the measurements were affected by local pollution. The filtering procedure is described in Section 3.1.1. The black dots in Figure 3.4 are the remaining N_{CN} data points. Note that especially during phases of high ambient pressure the local pollution is more intensive and the filter eliminates most of the data during these periods. Hence, on the 2nd, 11th to 13th and on the 15th of May almost no N_{CN} data points remain. These are time periods that directly follow the maxima in the pressure time series of Figure 3.2. Typical for high pressure systems are temperature inversions near the ground level that can trap local emissions and cause an enhanced influence of local pollution. Furthermore, Figure 3.4 shows N_{CCN} measured at $SS = 0.1 \%$ ($N_{CCN,0.1}$) and number concentrations of particles larger than 150 nm (integrated $PNSD$, $N_{CNraw>150nm}$) for the entire measurement period. For

3.1. Measurements of aerosol and CCN properties in the Mackenzie River delta (Canadian Arctic) during Spring-Summer transition in May 2014

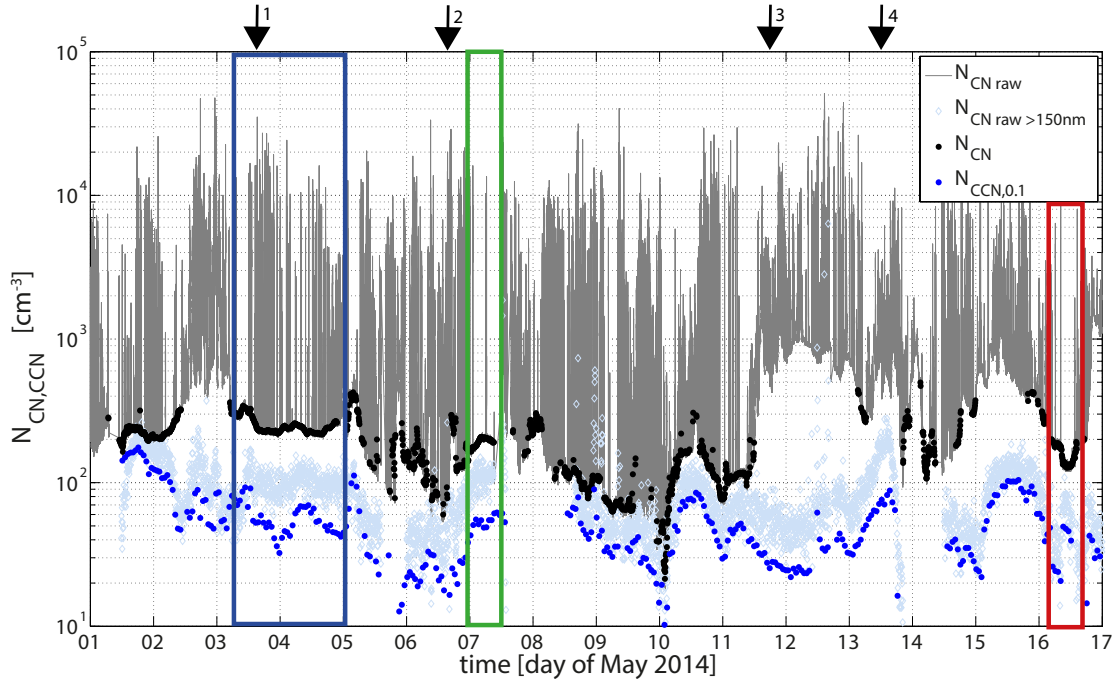


Figure 3.4.: **RACEPAC - time series of particle number concentrations**

Time series of N_{CNraw} (gray) and N_{CN} (i.e., the filtered data, black) as well as $N_{CNraw>150nm}$ (light blue) and $N_{CCN,0.1}$ (dark blue). The colored boxes mark the three periods of measurements that were used for further analysis. The arrows at the top indicate the four overflight times of the Polar 6 research aircraft.

$N_{CNraw>150nm}$ and $N_{CCN,0.1}$ the filter procedure was not applied. Generally, $N_{CNraw>150nm}$ and $N_{CCN,0.1}$ show similar trends, and both do not show pronounced peaks as those seen for N_{CNraw} . This indicates that the observed aerosol particles that were related to pollution occurred in the size range below 150 nm. This will be elaborated on below. It is, however, also worth noting that $N_{CNraw>150nm}$ scatters much more than $N_{CCN,0.1}$. This larger scatter originates in the higher frequency with which $N_{CNraw>150nm}$ was measured. Over the whole measurement period a mean N_{CN} of 188 cm^{-3} (and a median of 199 cm^{-3}) was observed when excluding the pollution periods. This is in good agreement with an Arctic long term study by Tunved et al. (2013) who report monthly mean N_{CN} for May (observed at Mt Zeppelin, Ny-Ålesund, Svalbard from March 2000 to March 2010) being slightly above 200 cm^{-3} . Generally they observed the highest concentrations between April and July which can be traced back to aged anthropogenic Arctic haze aerosol earlier in this time period and to new particle formation later (Tunved et al., 2013). That these two kinds of aerosols also play a major role in context of the present study is discussed in the following two sections by using air mass back trajectories and the $PNSDs$.

Figure 3.5 shows a comparison of the mean of all of those $PNSDs$ which were detected during time periods that were marked as clean ($PNSD_c$, corresponding to times when N_{CN} is shown as black dots in Figure 3.4) with the mean of all other $PNSDs$. The latter are those for which an influence of local pollution was assumed ($PNSD_p$). Also shown in

Figure 3.5 are error bars that indicate the range between the 25 % and 75 % percentiles. Both, $PNSD_c$ and $PNSD_p$ are bimodal with an Aitken mode below 100 nm and an accumulation mode above 100 nm. Above 150 nm, the accumulation modes of both are almost equal, whereas the Aitken mode of $PNSD_p$ is more pronounced than that of $PNSD_c$. Similar influences of local emission on $PNSD$ were found at an urban background station in Helsinki by Wegner et al. (2012). They observed modes between 10 nm and 40 nm in median urban $PNSD$ caused by traffic, domestic and district heating, comparable to the here presented result, albeit at higher concentrations. The observations by Wegner et al. (2012) support our assumption made earlier that the observed high peaks in N_{CNraw} originate from local pollution. It also demonstrates the usefulness of the applied filter. As for N_{CN} , also $PNSD_c$ agrees well with the observations of Tunved et al. (2013). A $PNSD$ shown in Tunved et al. (2013), representing the monthly median $PNSD$ for May over a period of ten years in an Arctic environment, shows the same characteristic as $PNSD_c$ of this study as shown in Figure 3.5. Both are bimodal with a distinct accumulation mode and a smaller Aitken mode. The variability of $PNSD_c$ and the dependence on the air mass origin is discussed in Section 3.1.4.

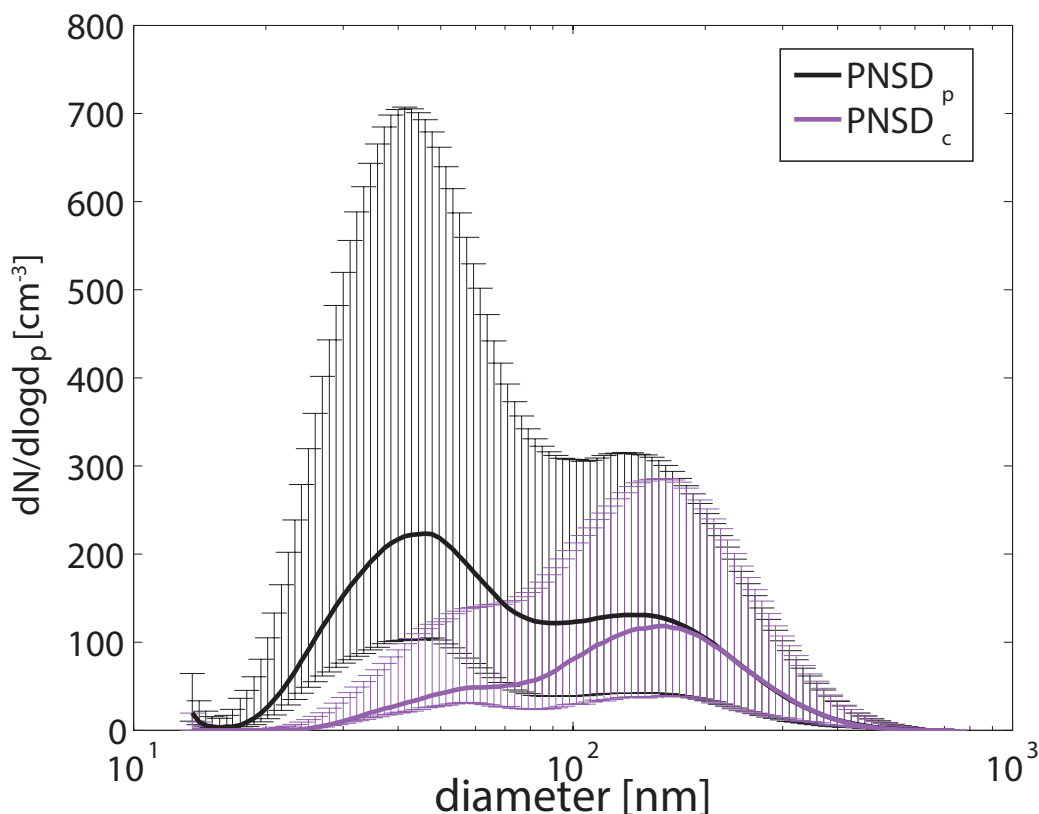


Figure 3.5.: **RACEPAC - clean and polluted $PNSD$**

Comparison of the median $PNSDs$ for times which were assumed to be clean ($PNSD_c$, purple) or polluted ($PNSD_p$, black). The thin vertical lines (same color code) indicate the range between the 25 % and 75 % percentiles.

After applying the filter to N_{CCN} and the $PNSDs$ only three distinct periods (Period 1: May 3 7:00 to May 5 0:00, Period 2: May 7 00:10 to May 7 9:00, Period 3: May 16 5:00 to May 16 12:15) of evaluable data remained, as these parameters were measured with a lower temporal resolution and were thus more prone to be effected by local pollution than N_{CCN} . The three periods are marked with a blue, green and red square in Figure 3.4. This color code is continuously used in the following figures. The arrows at the top of Figure 3.4 indicate the four overflights of the Polar 6 research aircraft. For these times a comparison of ground based and airborne $PNSDs$ of different altitudes was done, which is discussed in Section 3.1.6.

3.1.3. Identification of air mass origins and potential source regions

Two approaches to investigate the history of the measured air masses were applied on the data set measured at Tuktoyaktuk. First, the origins of the air masses for the three periods were identified by means of LAGRANTO backward trajectories. Second, the Potential Source Contribution Function (PSCF) is applied to identify regions that potentially act as source regions for aerosol particles measured throughout the whole campaign.

Origin of sampled air masses of the three periods

To assess the origin of the air masses of the three periods the Lagrangian analysis tool (Sprenger and Wernli, 2015) was used. The LAGRANTO backward trajectories were calculated based on analysis data from the European Center of Medium-Range Weather Forecasts (ECMWF). The data used have a horizontal grid resolution of 0.5° and 137 vertical hybrid sigma-pressure levels from the surface up to 0.01 hPa. Hourly 10-day back trajectories were started in the region around Tuktoyaktuk (69.43°N , 133.00°W) at a pressure level of 25 hPa below surface pressure. More specifically, trajectories at 13 receptor sites in the horizontal plane were initialized, accounting for the uncertainty introduced due to the relatively coarse horizontal grid and the release at an individual point. One receptor site was directly at the coordinates of the measurement station and 12 around the station. The upper panel of Figure 3.6 depicts the bundle of trajectories for the three time periods.

Two main air mass origins were observed. The air masses of Period 2 originated in the north east of Canada (in the province Nunavut). During May air masses from this area are typically highly contaminated due to high winter and springtime aerosol particle burdens which can be observed all over the Arctic (Shaw, 1995). In the following these air masses are termed “accumulation-type air mass“. The air masses of Period 3 originated in the southwest of Tuktoyaktuk (Eastern Russia, Kamchatka and the unfrozen North Pacific). In the following, these air masses are named “Aitken-type air mass“, and the naming of

the air masses will be explained in the next section, Section 3.1.4. Further the trajectories indicate that Period 1 includes both, accumulation- and Aitken-type air masses. The distribution of these two air masses during Period 1 is visible in the lower panel of Figure 3.6. The figure shows the number of trajectories per hour (for Period 1) that originated east ($N_{accumulation}$) or west (N_{Aitken}) of Tuktoyaktuk. It can be seen that during the first part of Period 1 (till 16:00 of 4 May 2014) the air masses in Tuktoyaktuk were a mixture of accumulation- and Aitken-type air masses. Until the 3rd of May Tuktoyaktuk was influenced by an anticyclone with a maximum pressure of 1035 hPa. The low pressure gradient of this anticyclone led to a low wind velocity and a baffling wind (see lower panel of Figure 3.2) which caused an alternation between the two air mass origins at

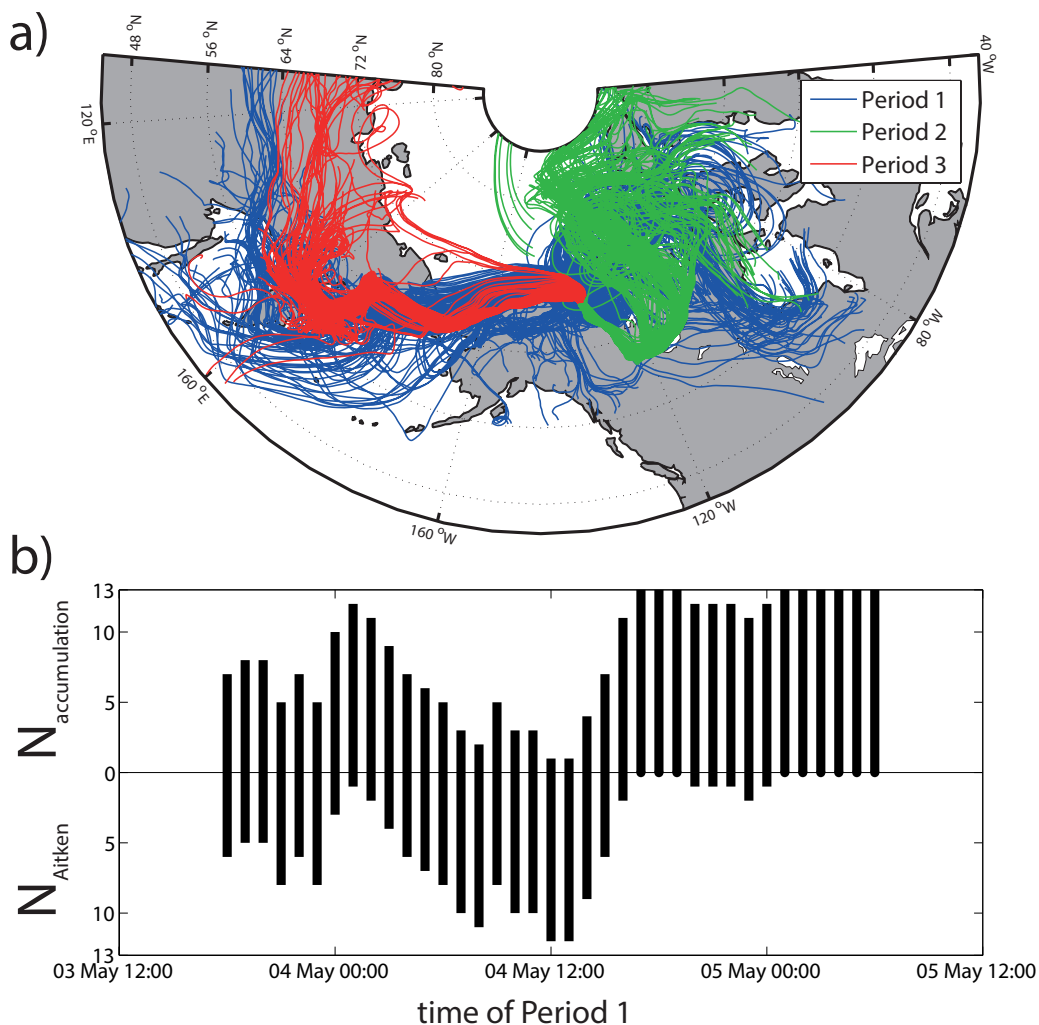


Figure 3.6.: **RACEPAC - backtrajectories of the three periods**

- a) 10 day back trajectories of the three periods started in and around Tuktoyaktuk at a pressure level of 25 hPa above the surface pressure.
- b) The total number of 13 trajectories per hour of Period 1 was split up into the number of trajectories that came from east ($N_{accumulation}$) or west (N_{Aitken}) to illustrate the alternation of the air mass origin.

the beginning of Period 1. The second part of Period 1 is characterized by a decreasing surface pressure and a constant easterly wind. With a temporal shift of less than one day also N_{Aitken} decreased which indicates that only accumulation-type air masses were present at Tuktoyaktuk.

PSCF analysis

The following PSCF results of N_{CN} were calculated as described in 2.3.2 on the basis of 6129 NOAA HYSPLIT back trajectories. The spatial distribution of the PSCF of N_{CN} is mapped in Figure 3.7. The map shows several areas of enhanced PSCF values, that can be linked to potential source regions. One of these spots of enhanced PSCF values is located in Central Canada, which potentially can be linked to biomass burning. To proof this possible connection, the MODIS Active Fire Product (MCD14ML) was used, to display the active wild fire spots that occurred between April 21th and May 17th in 2014 as magenta dots in the map. Due to the local proximity of these enhanced PSCF values and a spot of detected active fires south of them, it is possible, that high N_{CN} values were measured due to biomass burning in Central Canada.

Also active fires detected in Siberia show coincidence with a spot of enhanced PSCF values. From a detailed analysis on a daily basis follows, that especially this region of high PSCF values shows the occurrence of active fires throughout the whole time of analysis. Another spot in Siberia can be explained due to its proximity to Norilsk (red square in Figure 3.7) which is considered to be an Arctic point source for emissions due to nickel mining and aluminum plants. Although, improvement has been achieved since the '80s, Norilsk still remains one of the largest source of anthropogenic Arctic air pollution, mainly due to the emission of particulates and sulfur dioxide (AMAP, 2006).

Another point source of anthropogenic Arctic emissions is the Prudhoe Bay Oil Field in North Alaska, marked with a red diamond in Figure 3.7. As already mentioned in the introduction, Gunsch et al. (2017) and Kolesar et al. (2017) recently found the emissions of Prudhoe Bay Oil Field to cause increased N_{CN} values (13-746 nm) and have impact on growth events of nucleation and Aitken mode aerosol particles. Our PSCF analysis results in a spot of increased PSCF values in the vicinity of Prudhoe Bay Oil Field. This indicates that Prudhoe Bay Oil Field emissions potentially lead to enhanced N_{CN} values measured in Tuktoyaktuk.

The largest area of enhanced PSCF values is the area of the North-West Pacific. This region seems to overall cause relatively high N_{CN} values measured at Tuktoyaktuk, most likely due to marine emissions. A detailed discussion about the impact of marine emissions on the aerosol particles measured in Tuktoyaktuk is presented in the following section.

The above discussed PSCF results give a rough idea about the location of possible aerosol particle sources for our measurements at Tuktoyaktuk. However, in our case, the precision

of the PSCF method is limited due to the small amount of data.

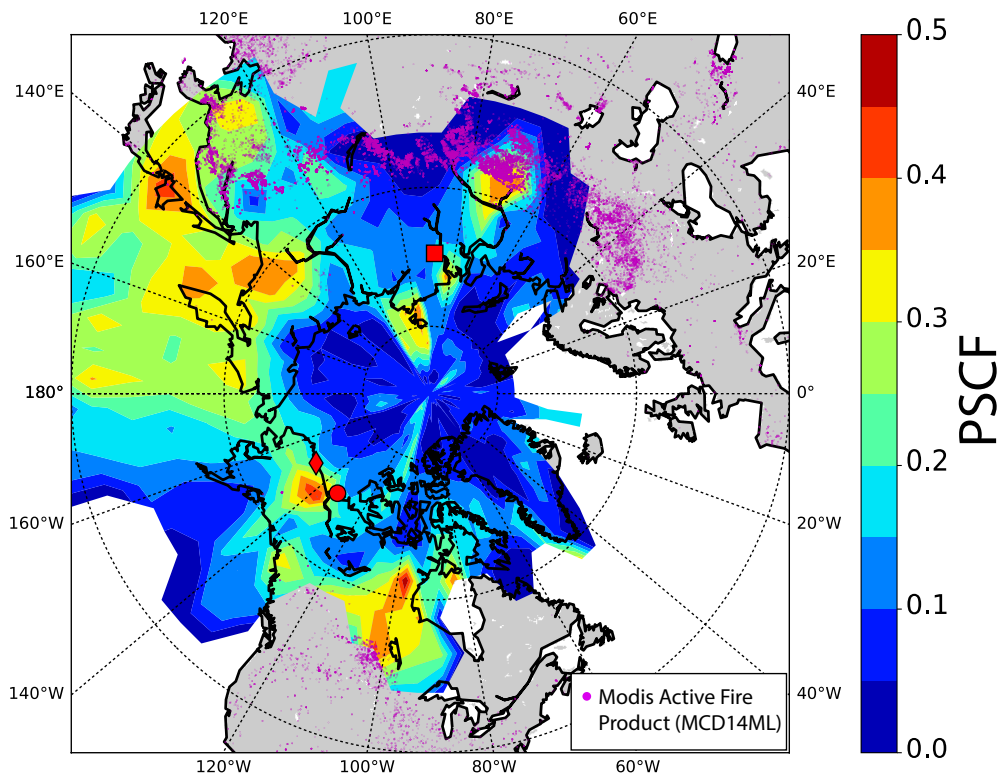


Figure 3.7.: **RACEPAC - PSCF analysis**

Map showing the PSCF function of N_{CN} , calculated on the basis of concentrations exceeding the 75 % percentile. The colorbar indicates the PSCF value and the red dot, the diamond and the square indicate the position of Tuktoyaktuk, Prudhoe Bay (Alaska, USA) and Norilsk (Russia), respectively. The purple dots display the location of active fire spots that occurred between April 21th and May 17th in 2014, detected by MODIS (Active Fire Product - MCD14ML).

3.1.4. $PNSD$ of the three periods

Figure 3.8a shows the median of the $PNSD_c$ of the three periods discussed in Section 3.1.3, together with the 25 % and 75 % percentiles. They were computed to examine their dependence on the origin of the air mass. The $PNSD_c$ of Period 1 ($PNSD_{c1}$) and Period 3 ($PNSD_{c3}$) are bi-modal with an Aitken mode below 100 nm and an accumulation mode above 100 nm whereas that of Period 2 ($PNSD_{c2}$) only shows the accumulation mode. The large variability observed in the shape of the $PNSD$ is typical for the transition period from Arctic spring to summer, i.e. higher variation of source regions during the Arctic summer. As described in more detail in the introduction, although there is a pronounced annual cycle in $PNSDs$ in the Arctic, common features concerning $PNSDs$ are shared

3.1. Measurements of aerosol and CCN properties in the Mackenzie River delta (Canadian Arctic) during Spring-Summer transition in May 2014

across the Arctic (Freud et al., 2017), and $PNSD$ s reported in Tunved et al. (2013) were used for comparison with our data in the following, as these were the first long term data describing the annual cycle.

$PNSD_{c2}$ is similar to the $PNSD$ that Tunved et al. (2013) observed for March and April on

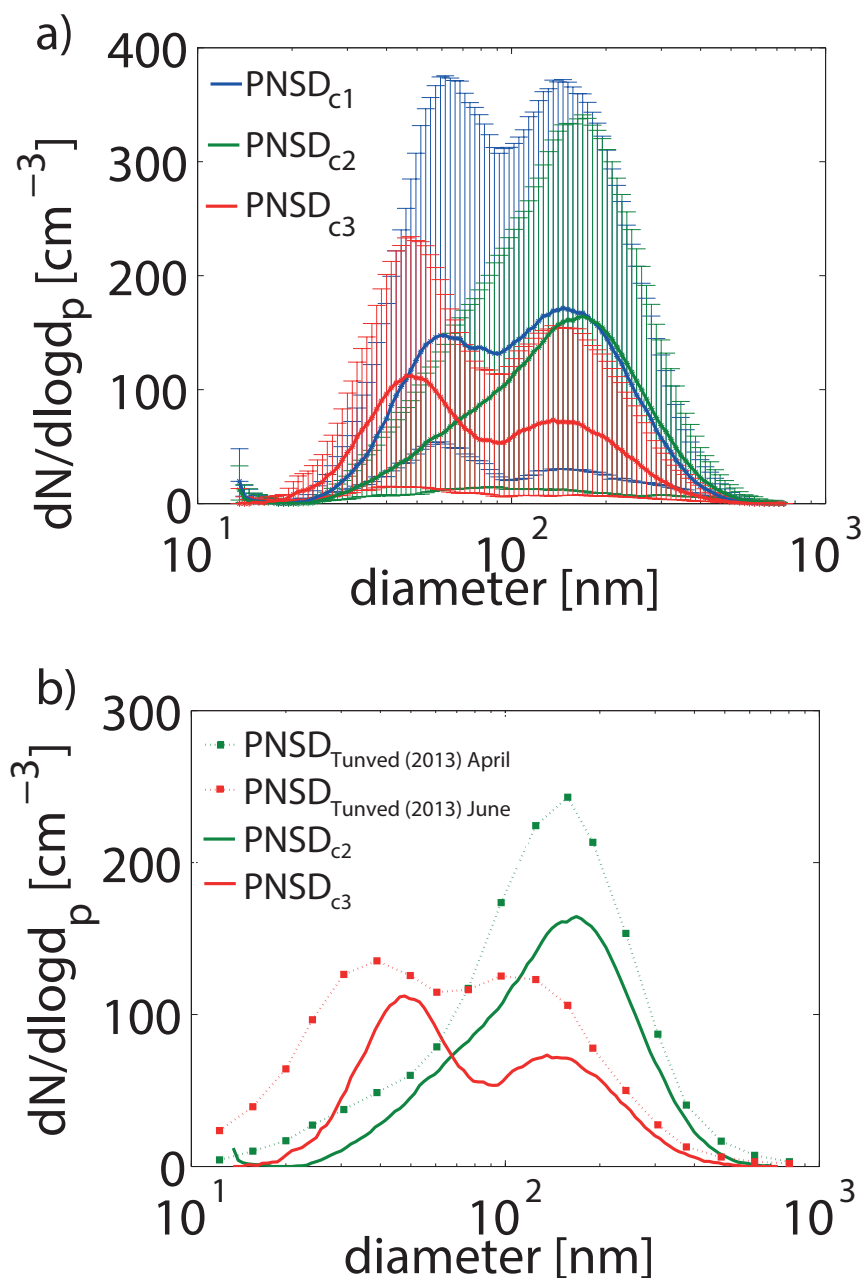


Figure 3.8.: **RACEPAC - $PNSD$ s of the three periods**

a) Thick lines show the median $PNSD$ of Period 1 (blue), Period 2 (green) and Period 3 (red). The thin vertical lines (same color code) indicate the range between the 25 % and 75 % percentiles.

b) Comparison of the median $PNSD$ of Period 2 and 3 with 10 year median $PNSD$ of April and June observed by Tunved et al. (2013) on Svalbard. The $PNSD$ s observed by Tunved et al. (2013) for April and June are comparable in shape with $PNSD_{c2}$ and $PNSD_{c3}$, respectively.

Svalbard. A direct comparison of $PNSD_{c2}$ and the median April $PNSD$ of Tunved et al. (2013) is shown in Figure 3.8b. The mono-modal accumulation mode aerosol is characteristic for the Arctic haze which mainly consists of particulate organic matter (POM) and sulfate (Quinn et al., 2002). Single particle analysis of aerosol particles samples taken at the Zeppelin Station, Svalbard, that occurred before the transition to the Arctic summer showed a dominance of spherical organic like particles in the submicrometer range with an Eurasian influence (Behrenfeld et al., 2008). These Arctic haze aerosol particles typically are well aged (Heintzenberg, 1980; Quinn et al., 2002). Due to the shape of $PNSD_{c2}$, and since the air mass of Period 2 has its origin in a region where conditions in May are still winterly, it is very likely that a typical Arctic haze air mass was observed. In contrast, $PNSD_{c3}$ is comparable to $PNSDs$ that are reported by Tunved et al. (2013) for June and July. $PNSD_{c3}$ and the median June $PNSD$ of Tunved et al. (2013) are depicted in Figure 3.8b. In addition to the accumulation mode the bi-modal summer time Arctic $PNSD$ shows an Aitken mode which most likely originates from particles formed by new particle formation (Engvall et al., 2008; Wiedensohler et al., 2011). A common precursor gas for new particle formation is dimethylsulfide (DMS) emitted from oceanic phytoplankton. This precursor is known to be more abundant during the Arctic summer when the marine biological activity has its maximum. An indicator for the presence of DMS is its oxidation product methanesulfonic acid (MSA) (Quinn et al., 2007). MSA also could be directly detected as component of the particulate matter itself in remote marine background aerosol and in plankton bloom areas (Zorn et al., 2008). Quinn et al. (2007) report the concentration of MSA for several Arctic measurement stations (e.g. Barrow and Alert - Tuktoyaktuk is located between the two) during at least 7 years. The MSA concentration starts to increase in April and has two maxima during the summer time, where both maxima were observed in Alert as well as in Barrow (Quinn et al., 2007). The later maximum occurs in July and August and is due to the local productivity of phytoplankton while the surface water is free of ice. The earlier maximum that occurs around the time of our measurements, can be associated with long-range transport from marine source regions from the North Pacific (Li et al., 1993). This fits well to the source region that was found for the air mass of $PNSD_{c3}$ and can explain the presence of the Aitken mode particles. The minimum between the Aitken and the accumulation mode can be explained by previous cloud processing during which further material was added to activated droplets via aqueous phase oxidation. After the evaporation of cloud droplets this process creates the bi-modal $PNSD$ with the Hoppel-minimum (Hoppel et al., 1994). In our case the Hoppel-minimum can be found at around 90 nm. While cloud processing is a well known process for gaining particulate matter and growing particles to larger sizes, particles can also grow by generation of particulate matter directly from the gas phase as described recently for Arctic conditions in e.g., Willis et al. (2016), Burkart et al. (2017a) and Collins et al. (2017). The observed minimum in the $PNSD$ occurs when new particle

formation takes place, either by adding small particles to an already aged air mass or by mixing of different air masses with one air mass containing aged and the other one newly formed particles, where one could come from aloft. It should also be mentioned that it was recently described in Gunsch et al. (2017) and Kolesar et al. (2017), that emissions from Prudhoe Bay oil field, which is located at the northern shore of Alaska roughly 700 km west of our measurement location, influenced Arctic PNDSs by adding both high concentrations of small particles and particulate mass to larger particles. Summarizing there is a number of reasons that can add to the observed bi-modality of the size distribution, but small, comparably newly formed particles will make up the observed Aitken mode in all cases. Sources of the precursor gases forming these particles will differ from spring to summer, as mentioned above (Li et al., 1993).

In Section 3.1.3 it is described that the back trajectories for time Period 1 altered between the two source regions. This observation is supported by the shape of $PNSD_{c1}$ which suggests that both source regions contribute to the aerosol particles observed during this period. $PNSD_{c1}$ is bi-modal (similar to $PNSD_{c3}$) but with a less pronounced Hoppel-minimum and a distinct accumulation mode (similar to $PNSD_{c2}$). Due to the strongly alternating air mass origins during Period 1, the attempt to separate the two cases in $PNSD_1$ did not succeed, and the aerosol particle population reported for Period 1 in this study comprises a mixture between accumulation- and Aitken-type air masses. However, due to the absence of detailed information on the composition of the aerosol particles such considerations remain speculative.

3.1.5. Critical diameter d_{crit} and hygroscopicity parameter κ

In Section 2.2.2 it is described how the critical diameter d_{crit} and the hygroscopicity parameter κ can be determined based on the measured N_{CCN} and $PNSD$. d_{crit} and κ were derived for (i) the whole measurement period using unfiltered $N_{CCN,0.1}$ and corresponding $PNSD$ and (ii) the three selected periods described above, using filtered N_{CCN} at all SS and $PNSD_c$. Figure 3.9 shows the time series of N_{CN} and N_{CCN} (mean concentration with standard deviation as error bars) in the upper panel, d_{crit} in the middle panel and κ in the lower panel. Note, data concerning all SS are only available during the three selected periods. In Section 3.1.2 it is described that the pollution occurred in the size range below 150 nm. N_{CCN} measured at SS higher than 0.1 % are affected by local pollution due to the lower d_{crit} (d_{crit} is discussed in detail below) and thus are not analyzed for the whole measurement period except the three periods. The uncertainties for d_{crit} and κ as given by the error bars were determined by the use of a Monte Carlo simulation. A detailed description of this method is given in Appendix A.2. (The uncertainties for d_{crit} are typically smaller than the symbol size.)

During the whole measurement period the unfiltered $N_{CCN,0.1}$ covers a range between less

SS [%]	N_{CCN} [cm^{-3}]	d_{crit} [nm]	κ
0.1	45	191	0.18
0.2	118	107	0.28
0.3	139	89	0.21
0.5	164	64	0.23
0.7	197	50	0.26

Table 3.1.: **RACEPAC - CCN and hygroscopicity**

Median values of N_{CCN} , d_{crit} and κ for different SS. Values for SS=0.1 % are calculated using the unfiltered data that cover the entire measurement period, whereas the values for SS=0.2, 0.3, 0.5 and 0.7 % are calculated using the filtered data of Period 1, 2 and 3.

than 10 and 200 cm^{-3} with a median of 45.2 cm^{-3} . The median d_{crit} values as well as the median concentrations for the filtered N_{CCN} are presented in Table 3.1. The corresponding inferred values for κ are representative for aerosol particles with sizes close to d_{crit} and therefore can be assigned to the modes in the *PNSD*. Therefore, κ derived for SS = 0.1 % displays the hygroscopicity of the accumulation mode as d_{crit} for SS = 0.1 % is in the neighborhood of the maximum of this mode. κ values for SS = 0.2 % and SS = 0.3 % are representative for the size range close to the Hoppel-minimum whereas κ values for SS = 0.5 % and SS = 0.7 % are representative for the Aitken mode. The median κ values for SS=0.1, 0.2, 0.3, 0.5 and 0.7 % are 0.18, 0.28, 0.21, 0.23 and 0.26, respectively. These values are summarized in Table 3.1. For time Period 1,2 and 3, the κ values averaged over all SS are 0.22, 0.23 and 0.26, respectively. Following it will be discussed how these κ values relate to the measurement uncertainty.

Figure 3.10a shows the probability density function (pdf) of all κ values that are presented in the lower panel of Figure 3.9. The blue line displays the median of the inferred κ values which is 0.23 and the red lines are the 5 and 95 % percentiles. The width between these percentiles, $\sigma_{s,allSS}$, amounts to 0.23. To check whether these inferred κ values allow a physical interpretation of the variability of κ , the Monte Carlo simulation was used, as described in the Appendix A.2. In short, using Monte Carlo simulations, the uncertainty for each κ value was determined separately based on uncertainties in d_{crit} , N_{CCN} and S_{crit} . This uncertainty was again expressed as the width between the 5 and 95 % percentiles. The separate widths were averaged, yielding $\sigma_{MC,allSS}$, which was determined to be 0.16. To resolve physically driven changes, $\sigma_{s,allSS}$ should be significantly larger than $\sigma_{MC,allSS}$ (at least twice as large). But $\sigma_{s,allSS}/\sigma_{MC,allSS}$ only amounts to 1.44, which indicates that 70 % (= 1/1.44) of the variability in the observed κ values is related to measurement uncertainties of the *PNSD* and the SS in the CCNC. For corroboration, the same analysis was done based on a sub-set of all data. In Figure 3.10b the κ values at SS = 0.1 % are displayed as a probability density function with a median of 0.19 and a width between the 5 and 95 % ($\sigma_{s,0.1}$) percentiles of 0.23. The width between the 5 and 95 % percentiles of the Monte Carlo simulation ($\sigma_{MC,0.1}$, only for SS = 0.1 %) is 0.14 so that the ratio be-

tween both is 1.64. Hence 60% of the variability in the observed κ values at $SS = 0.1\%$ is related to measurement uncertainties. Summarizing, it can be stated that our observed κ values show no significant dependencies on the SS or the air mass origin that can be resolved with our set up and method.

Kammermann et al. (2010) measured N_{CCN} and inferred d_{crit} and κ in a subpolar environment during a ground based measurement campaign in north Sweden for SS from 0.1 to 0.7% in July 2007. They report κ values in the range of 0.07 to 0.21. Moore et al. (2011) and Latham et al. (2013) report κ values from airborne measurements in Alaska (April 2008) and North Canada (June to July 2008), respectively. Both observed values between 0.05 and 0.3 within a SS range of 0.1 to 0.6%. Lower κ are likely to indicate a higher organic fraction in these environments, and particularly for Kammermann et al. (2010), the lowest values can be explained by the local proximity to the Stordalen mire which is known to emit biogenic precursors of organic aerosol particles. In a modeling study by Pringle et al. (2010), the annual mean κ values at the surface in the region around Tuktoyaktuk were approximately 0.3. Overall the κ values derived in this study are comparable to previously published values.

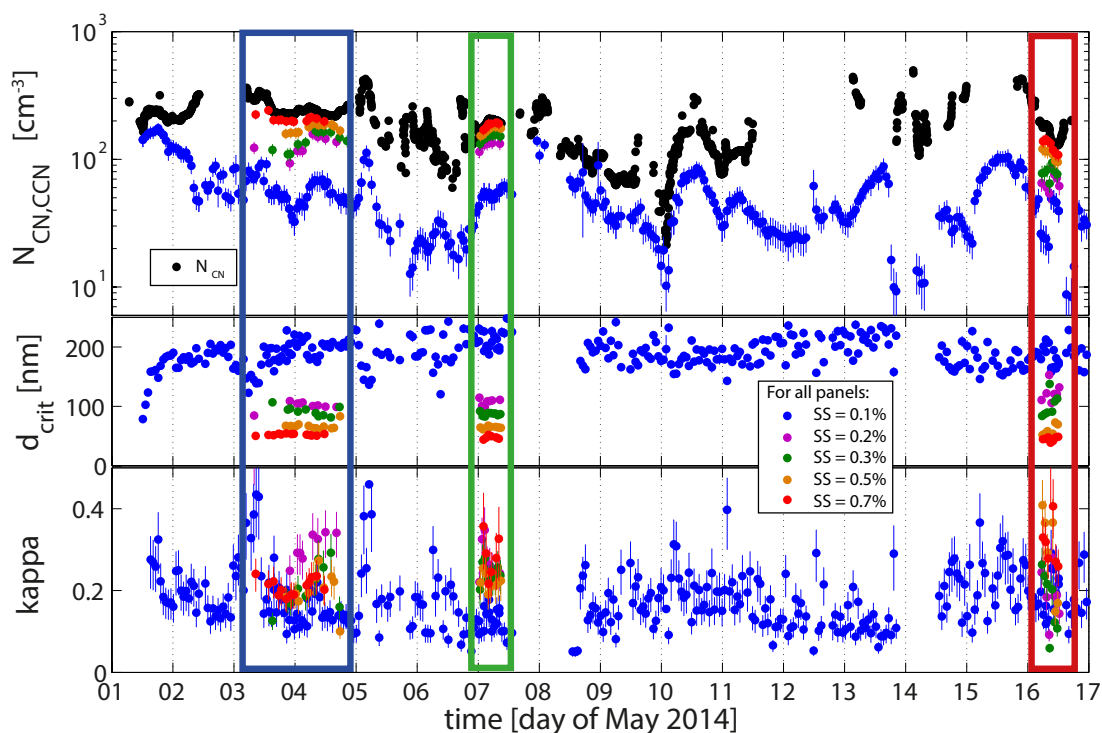


Figure 3.9.: **RACEPAC - CCN and hygroscopicity**

The time series of N_{CN} and N_{CCN} in the upper panel, d_{crit} in the middle panel and the inferred κ values in the lower panel. The error bars of N_{CN} and N_{CCN} show the standard deviation whereas the error bars of d_{crit} and κ show uncertainties that are determined by means of a Monte-Carlo simulation. The blue data points show the unfiltered data corresponding to $SS = 0.1\%$. The other colors correspond to the filtered data ($SS \geq 0.1\%$) of Period 1, 2 and 3, marked with the blue, green and red box, respectively.

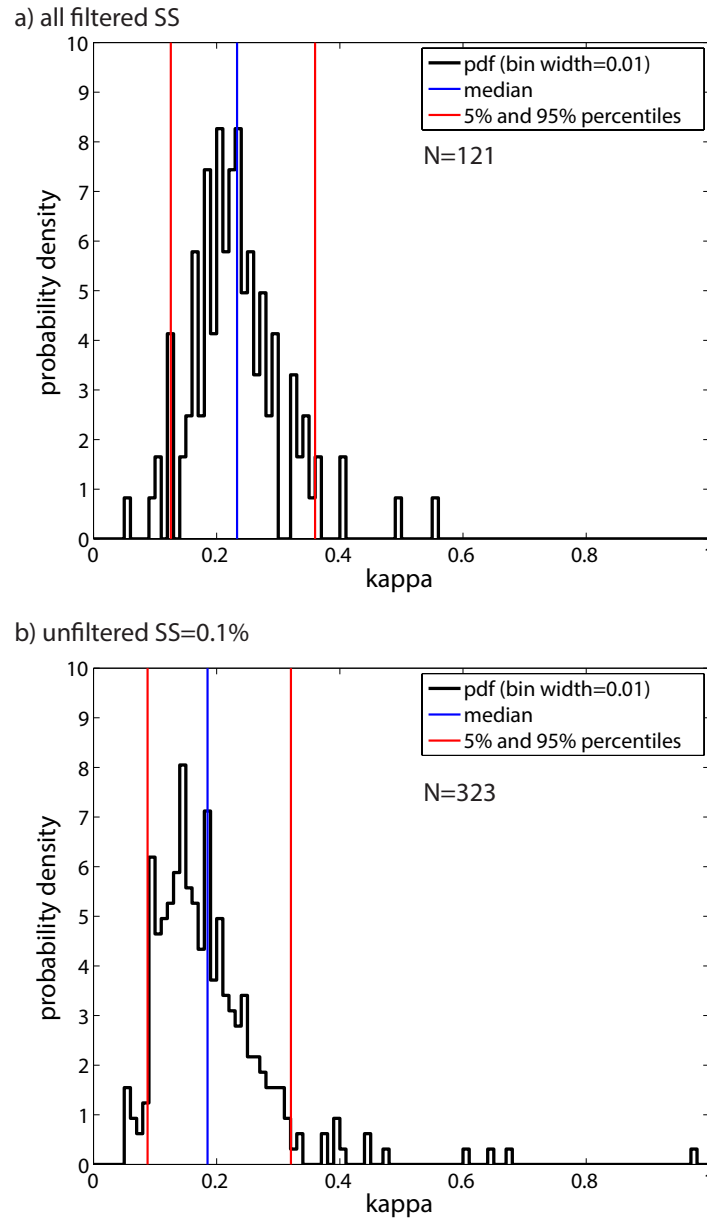


Figure 3.10.: **RACEPAC - κ PDF**

- a) Probability density function of all inferred κ values (filtered values of all supersaturations) of the lower panel of Figure 3.9.
- b) Probability density function for κ values at $SS = 0.1\%$ (inferred from the unfiltered CCN and $PNSD$ data of Figure 3.4). The blue line displays the median and the red lines show the 5 and 95 % percentiles of the probability density function.

3.1.6. Comparison of height resolved airborne and ground based $PNSDs$

During the campaign 4 overflights of the Polar 6 research aircraft were performed. Overflight 1 and 2 were single overflights at a constant altitude of 600 m and 200 m, respectively. During Overflight 3 and 4 eight legs in altitudes between 300 m and 3000 m were

flown. The comparison of the airborne and ground based measured $PNSDs$ of the four overflights is shown in Figure 3.11. Arrows in Figure 3.4 indicate the times when the four overflights took place. For Overflight 1 and 2 simultaneous measurements of filtered $PNSD_c$ exist. For Overflight 3 and 4 the closest filtered $PNSD_c$ measurements have a temporal distance of 7 and 6 hours to the time of overflight, respectively. Hence, for the comparison in case of Overflight 3 and 4 the unfiltered $PNSD_d$ measurements are used. The airborne $PNSDs$ measured by means of an UHSAS were recorded with a time resolution of 1 s and extrapolated to standard pressure (1013.25 hPa). In Figure 3.11 the UHSAS distributions are generally displayed as the median of 100 measured distributions. Additional bars that indicate the range between the 25 and 75 % percentiles are added to the distributions of Overflight 1 and 2. $PNSD_c$ and $PNSD_d$, which were measured at the ground, are shown for ambient pressure.

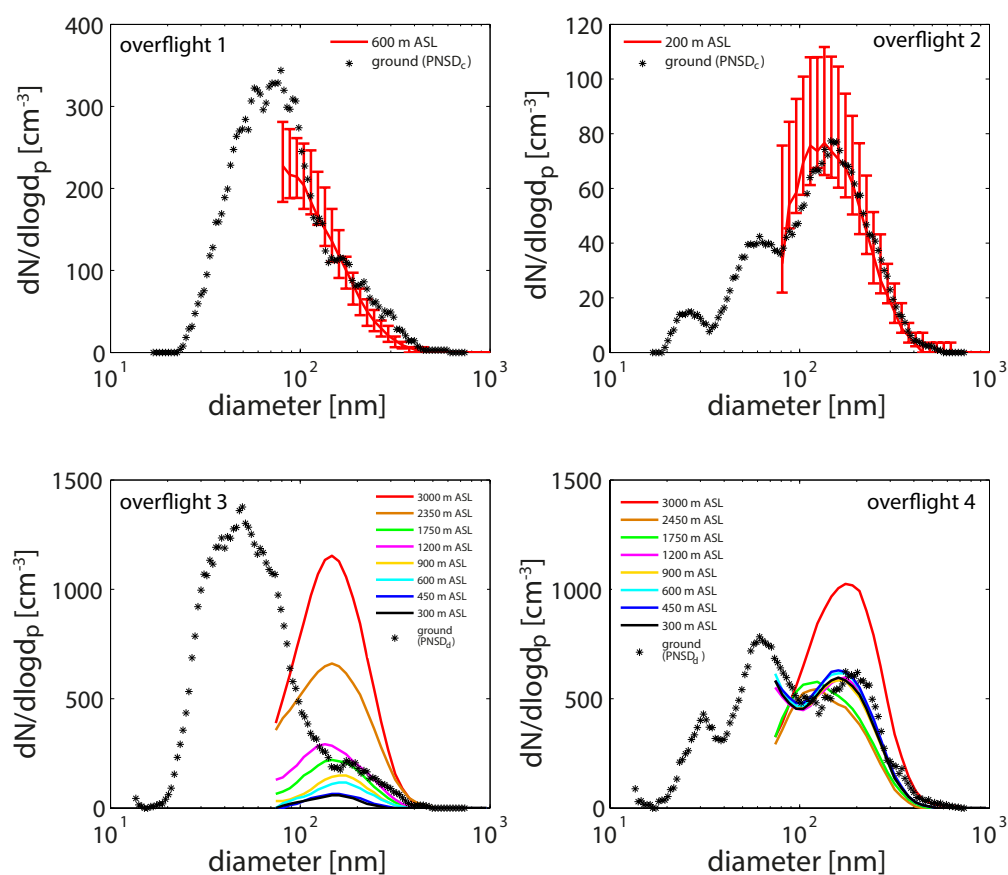


Figure 3.11.: RACEPAC - comparison of ground based and airborne $PNSDs$

$PNSDs$ measured at the ground based station and on the Polar 6 research aircraft during four overflights. Overflight 1 and 2 took place in 200m and 600m, whereas Overflight 3 and 4 were profile flights at altitudes between 300 and 3000 m. Airborne measurements from 70 nm up to 1 μ m were done using an UHSAS, while ground based $PNSD_c$ s and $PNSD_d$ s of aerosol particle diameters from 13.6 nm up to 736.5 nm were measured using a SMPS as indicated in the setup of Figure 3.3.

For Overflight 1 and 2, the ground based $PNSD_c$ s agree well with the airborne $PNSD$ in the overlapping size range of 70 nm to 736.5 nm, where airborne measurements were carried out at 600 m and 200 m, respectively. Vertical temperature profiles observed by radiosondes over Inuvik show temperature inversions at altitudes of 1500 m and 700 m for Overflight 1 and 2, respectively (not shown here). This indicates that during these two distinct time periods the ground based measurements of $PNSDs$ are representative for the atmospheric boundary layer.

For Overflights 3 and 4, the measured $PNSDs$ varied with respect to the particle number concentration and shape for the flights in different altitudes between 300 m and 3000 m. The airborne $PNSDs$ of Overflight 3 show the same shape at all eight heights with a clear decrease of the number concentration at lower heights. The integration of the $PNSD$ measured at 300 m (black line) gives a total particle number concentration of 24 particles per cm^3 , whereas it is 512 cm^{-3} at an altitude of 3000 m, i.e., twenty times higher. However the shape of the $PNSDs$ does not change with height as all distributions are mono-modal with a maximum at approximately 150 nm. The ground based $PNSD_d$ in the size range above 150 nm agrees best with the airborne $PNSD$ that was measured at 1200 m. At smaller sizes no comparison can be done, as the local pollution produces a large mode below 150 nm. The ambient temperature recorded at the Polar 6 aircraft during Overflight 3 indicates a temperature inversion near an altitude of 2000 m. For further investigation back trajectories at altitudes of 1000, 2000 and 3000 m were calculated to investigate the history of air masses at different altitudes. The trajectories arriving at altitudes of 1000 and 2000 m show an air mass origin in the area of the Northern Pacific, comparable to time Period 3 in Section 3.1.3. But the trajectory that arrived in 3000 m indicates an air mass origin in the central Arctic and over Greenland. Hence, the origin of the air masses and the relatively higher particle number concentration in the accumulation mode of the $PNSD$ may indicate that the typical aged Arctic spring aerosol, that was observed during Period 2, is present above the temperature inversion. This aerosol could be mixed down to lower layers accompanied by a dilution process, however, aerosol observed at the lower levels is likely mostly of a different origin. Overflight 4 shows that the airborne $PNSDs$ also may differ in shape depending on the height. The $PNSDs$ between 1750 and 3000 m are mono-modal with a maximum between 100 and 200 nm. Also a comparably high particle number concentration was measured at an altitude of 3000 m. The $PNSDs$ at lower heights imply a second mode below 100 nm. This Aitken mode is also present in the ground based $PNSD_d$ which fits the airborne $PNSDs$ that were measured below 1200 m. The air masses above 1750 m show characteristics of the typical aged Arctic accumulation-type aerosol (comparable to Period 2) whereas the air masses below 1200 m seem to consist of aerosol of marine origin (comparable to Period 3). For Overflight 4, two temperature inversions were recorded between 2500 and 3000 m. The temperature inversions and the different shapes of the $PNSDs$ are indicative of the pre-

sence of different air masses during Overflight 4, although air mass back trajectories that arrived at 1000, 2000 and 3000 m indicate an air mass origin over the Northern Pacific for all three heights. Stone et al. (2014) explain that layering of Arctic aerosol, as it was observed during Overflight 4, is a function of where the aerosol particle sources are located. Thereby the crucial factors are the different pathways of aerosol transport in the lower Arctic troposphere. The cold air of the lower Arctic troposphere is covered by surfaces of constant potential temperature and forms a dome over the Arctic (Law and Stohl, 2007). According to Stohl (2006) three transport pathways are possible: 1) low-level transport followed by ascent along the surfaces of constant potential temperature; 2) only low-level transport; 3) uplift outside the Arctic followed by transport in the upper troposphere and descent in the Arctic. It is likely that the aerosol particles observed in the upper levels of Overflights 3 and 4 were transported via pathway 1 or 3 whereas pathway 2 might be responsible for the occurrence of the bi-modal *PNSD* below 1200 m during Overflight 4. Note that the altitude resolved *PNSDs* presented here only represent a short snapshot in time. Hence, our observations do not describe how the transition from Arctic spring to summer affects the Arctic *PNSD* in the different lower layers of the troposphere. However, the measurements during all four overflights show that the ground based *PNSD* is similar to the airborne *PNSD* of the lowest tropospheric layers. Therefore it can be excluded that local natural sources contribute significantly to our measurements during the observed time period at least after removing signals from local pollution. It is more likely that aerosol particles or their precursor gases are advected via long range transport from lower latitudes in different height layers and mixed down in the lower Arctic troposphere.

3.2. Measurements of aerosol and CCN properties at the Princess Elisabeth Antarctica Research Station during three austral summers

3.2.1. Campaign overview

Measuring site and meteorology

The measurements presented here were all performed at the Belgian Antarctic research station Princess Elisabeth (PE, Figure 3.12a), in Dronning Maud Land, East Antarctica (71.95° S, 23.35° E, 1390 m asl., around 200 km away from the Antarctic coast). The PE station is located upon the granite ridge of Utsteinen Nunatak and lies north of the Sør Rondane Mountain Range, that has peaks up to an altitude of 3300 m asl. This area is located in the escarpment zone between the Antarctic inland plateau and the coast which can be seen in the topographic map of Antarctica in Figure 3.12b. A more detailed description of the measuring station and its near surrounding is given by Gorodetskaya et al. (2013). The PE station is designed as a zero emission station with power production mainly based on wind and solar energy (see www.antarcticstation.org). This reduces local emissions which makes the PE station an excellent base for conducting in situ aerosol particle measurements. Nevertheless, general station activities, traffic by skidoos or bulldozers, and irregular diesel generator operation times cause contamination which is however discarded in the final data (see section 3.2.1). The station is inhabited from November through the end of February. During the other months the station and most of its scientific instruments are operated under remote control. As the Cloud Condensation Nuclei counter used for this study needs an operator on site, mainly data collected from December to February during three subsequent austral summers (2013-2016) is presented. In the framework of this thesis, aerosol measurements at PE were supplemented with a Cloud Condensation Nuclei Counter (CCNC). Similar to data collected in the Arctic, the task was a basic characterization of the aerosol, including CN and CCN, and possible sources for the observed particles.

The basic meteorological parameters (temperature, pressure, relative humidity, wind speed and wind direction) were measured by means of an automatic weather station (AWS, Gorodetskaya et al., 2013) which was located 300 m east of PE. Precipitation was measured on the roof top of PE using a METEK MRR-2 radar. Details about the AWS and the precipitation radar can be found in Gorodetskaya et al. (2013) and Gorodetskaya et al. (2015), respectively. Generally, the meteorological situation at PE is characterized by either synoptic regimes, which usually correspond to strong easterly winds, or a katabatic regime, that is mostly associated with relatively weak south-southeasterly winds (Gorodetskaya et al., 2013). The two different meteorological situations can be identified

3.2. Measurements of aerosol and CCN properties at the Princess Elisabeth Antarctica Research Station during three austral summers

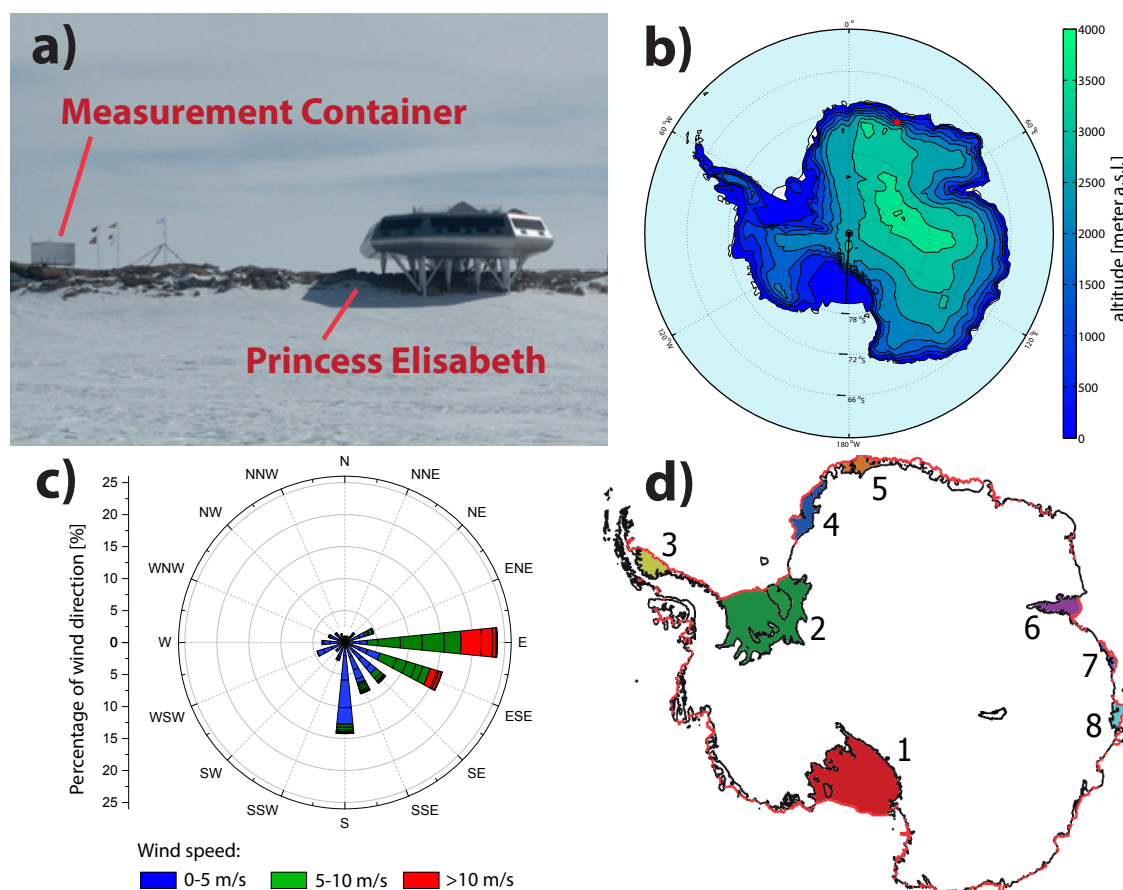


Figure 3.12.: **Antarctica - overview about the Princess Elisabeth Antarctica research station**

a) Picture of the Princess Elisabeth research station and the measurement container, where the aerosol measurements were performed, both located on the Utsteinen Nunatak ridge (view from ESE). b) Topographic map of Antarctica, the red dot shows the location of PE. This map was done using the Matlab mapping package *M_Map*. c) Wind direction and wind speed depicted as a wind rose for the third measurement period (December 18, 2015 to February 20, 2016). d) Map showing the location of the largest shelf ice regions in Antarctica: 1) Ross 2) Ronne-Filchner 3) Larsen C 4) Riiser-Larsen 5) Fimbul 6) Amery 7) West and 8) Shackleton shelf ice. The black line represents the coast line and the red line represents the ice edge. This map was created using Matlab and Antarctic Mapping Tools (Schaffer et al., 2016; Greene et al., 2017).

based on wind speed and wind direction, which are both depicted in the form of a wind rose in Figure 3.12c (exemplarily based on measurements between December 18, 2015 to February 20, 2016 in the third season). The more frequent easterly winds clearly correspond to higher wind speeds, mainly over 5 m/s, whereas the less frequently occurring southerly winds are usually below 5 m/s. Additional meteorological parameters for each year are shown in Figure 3.13 as a time series of hourly (gray lines) and daily averaged (red lines) values. Respective seasonal mean values together with the standard deviation, minimum and maximum for the period from December 1 to February 20 are shown in Table 3.2. The mean values as well as the fluctuation in the meteorological parameters show no large differences between the three measurement periods. Due to the shielding effect of the Sør Rondane Mountains to the South, blocking the katabatic winds from

the inland plateau, the climate at PE is relatively mild for the Antarctic escarpment zone (Gorodetskaya et al., 2013).

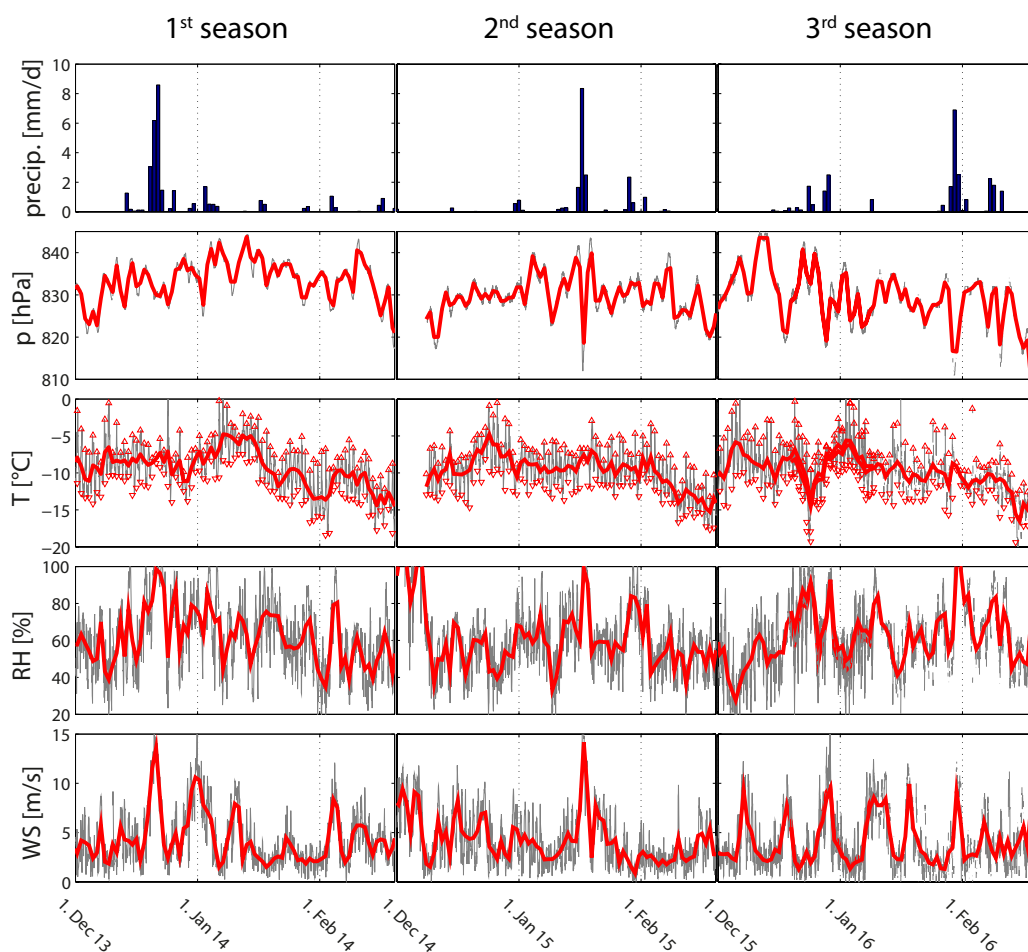


Figure 3.13.: **Antarctica - time series of basic weather parameters**

Time series of hourly (gray) and daily (red) mean values for temperature, pressure, relative humidity with respect to ice (RH) and wind speed (WS) measured by the AWS. Maximum and minimum temperature values are shown as triangles. The daily precipitation measured by the precipitation radar is shown as bars.

Instrumentation and data processing

The total particle number concentration (N_{CN}) was measured by a Condensation Particle Counter (CPC, TSI model 3776), which has a lower cut off at 3 nm and was operated at a total flow rate of 1.5 l/m. The CPC was first installed for continuous operation in November 2012. Due to several power outages in austral winter, data coverage of the winter months was not equal between the years and the CPC was restarted in the respective austral summers. The last data for this study was measured in May 2016. The inlet tubing for the CPC consisted of a 1 mm long vertical 0.5 in stainless steel tubing (not heated) installed tightly through the roof of the measurement container. Inside, 0.7 m of a 3/8 in

variable	2013/2014			2014/2015			2015/2016		
	Mean (std)	Min	Max	Mean (std)	Min	Max	Mean (std)	Min	Max
Air temperature [°C]	-9.4 (3.1)	-19.3	0.5	-9.7 (2.7)	-17.6	-0.5	-10.1 (2.7)	-20.5	2.3
Pressure [hPa]	833.4 (5)	817.3	844.3	829.7 (4.7)	812	843.5	828.6 (6.6)	807	845.3
RH [%]	61.9 (18.6)	13.1	100	58.9 (17.2)	14	100	64.3 (18.2)	14.7	100
Wind speed [m/s]	4.35 (2.87)	0.13	16.21	4.26 (2.89)	0.03	22.59	4.21 (2.99)	0	16.6
Precipitation [mm/d]	0.38(-)	-	8.6	0.24 (-)	-	8.3	0.35 (-)	-	6.9

Table 3.2.: **Antarctica - basic weather parameters**

Basic meteorological parameters (temperature, pressure, relative humidity with respect to ice, wind speed and precipitation) measured by the AWS and the precipitation radar. Shown are the mean, standard deviation, minimum and maximum values based on hourly mean values, in case of precipitation daily mean values, for the three measurement periods (each from 1 December to 20 February).

Parameter	Median concentration (10 %, 90 % percentile) [cm^{-3}]	Median concentration during CEs (10 %, 90 % percentile) [cm^{-3}]	N_{CN} (LAS)/ N_{CN} (CPC) or N_{CCN} / N_{CN} (CPC)
N_{CN} (CPC)	333 (206, 893)	292 (205, 474)	-
$N_{CN>90nm}$ (LAS)	20 (14, 29)	20 (14, 29)	0.06
$N_{CCN,0.1\%}$	14 (10, 23)	14 (10, 21)	0.04
$N_{CCN,0.2\%}$	81 (56, 110)	79 (58, 105)	0.24
$N_{CCN,0.3\%}$	121 (90, 168)	120 (95, 161)	0.36
$N_{CCN,0.5\%}$	177 (125, 260)	177 (133, 232)	0.53
$N_{CCN,0.7\%}$	212 (138, 326)	210 (150, 292)	0.64

Table 3.3.: **Antarctica - summary of measured properties**

Overview showing N_{CN} , $N_{CN>90nm}$ and N_{CCN} at different supersaturations, given as median (and 10 % and 90 % percentiles in brackets) in column 1 for all data, in column 2 for CEs (continental events, based on the regional analysis of the NAME model output). Column 3 shows the fraction of $N_{CN>90nm}$ and N_{CCN} to N_{CN} (based on the median values of column 1).

(0.19 in inner diameter) conductive flexible tubing made the connection to the CPC with only a smooth bend just before the inlet at the front of the CPC. On the roof of the container, 0.15 m of the same flexible tubing was connected to the stainless steel tubing in order to serve as inlet without a size cut-off. With this kind of inlet, there were never issues with inlets clogged by snow during storms, in particular important during the non-inhabited winter periods. Clogging of inlets caused by riming never happened due to the extreme dryness at the measurement site. The CPC was operated with a 4 l butanol reservoir bottle. Consumption of butanol was between 3 to 3.5 l for a complete year of measurements. Each austral summer the CPC was checked on leaks and the butanol was exchanged. The procedure to assure non-contaminated data is described further below.

In parallel to N_{CN} the particle number size distribution (*PNSD*) was measured by means of a Laser Aerosol Spectrometer (LAS, TSI model 3340) in the size range from 90 nm up to 6.8 μm (99 log-distributed channels). The inlet setup and tubing for the LAS is likewise the one for the CPC and installed directly next to that one. However, inside, first 0.5 m of a 1/8 in (inner diameter) and then 0.2 m of a 1/16 in (inner diameter) conductive flexible tubing made the connection (no bend) to the measurement chamber of the LAS. The LAS was maintained and re-calibrated in spring 2015 by TSI Inc. A comparison with a SMPS system was done at the cloud laboratory of the Leibniz Institute for Tropospheric Research.

The number concentration of cloud condensation nuclei (N_{CCN}) was measured using a Cloud Condensation Nuclei counter (CCNC, Droplet Measurement Technologies (DMT), Boulder, USA). The inlet tubing for the CCNC consisted of a 2.2 m long vertical conductive flexible tubing (likewise the one used for the CPC and LAS) with only a smooth bend just before the inlet of the CCNC. The inlet outside was directly next to the inlets of the CPC and LAS. The CCNC was operated as recommended by Gysel and Stratmann (2013) for polydisperse CCN measurements. The CCNC was operated at a constant total flow rate of 0.5 l/m and at 5 different supersaturations (*SS*; 0.1, 0.2, 0.3, 0.5 and 0.7 %), each for 12 minutes per hour. To ensure stable column temperatures, the data of the first 5 min at each *SS* setting were excluded from the data analysis. As a further stability criterion the temperature of the OPC was used. If the difference between the set and the read temperature of the OPC was larger than 1 K the data was excluded from the analysis. The remaining data points were averaged, so that the result is one N_{CCN} value per *SS* per hour. For consistency checks between N_{CN} and N_{CCN} also 1 % *SS* was adjusted at times (but data at that *SS* were not included in the analysis presented in here). All values (N_{CN} , N_{CCN} and *PNSD*) measured at the PE station are presented with respect to standard conditions, i.e., a pressure of 1013.25 hPa and a temperature of 293.15 K.

The container for the aerosol measurements is located 60 m south of the PE main station (Figure 3.12a). Given that the PE station is designed as a zero-emission station, the daily activities are concentrated in the W-NW sector, and the distribution of the wind direction

(Figure 3.12c), the container was most often exposed to non-contaminated air. The container is well-insulated and equipped with a small heater. Heating was hardly necessary in austral summer (due to 24 hour sun light). However, there is no air conditioning system (due to energy demand; remote control during austral winter; necessary filter systems and no exchange possible of them during austral winter). Therefore, in austral summer, the temperature inside the container varied between ≈ 10 and 40 °C. This range exceeds the recommended operating temperature range of the CPC and the LAS of 10 to 35 °C and 10 to 30 °C, respectively, as well as the temperature range for which the CCNC was calibrated, which is 20 to 30 °C. Therefore, N_{CN} , N_{CCN} and $PNSDs$ measured during time periods in which the temperature inside the measurement container was outside of the operating temperature ranges were excluded from the analysis presented herein.

Further, as mentioned in section 2.1, the data still contained values caused by emissions from the activities at the station. In order to identify hourly intervals with contamination, the following data sets were examined: i) the minute-CPC data; ii) simultaneously measured hourly data for the mass concentration of light-absorbing aerosol (Magee Sci. AE31, 7-wavelength aethalometer; set up in the same measurement container); iii) wind speed and wind direction measured by the AWS. As indicators for contamination abrupt peaks, outliers, and strong variations between higher and lower minute-CPC values and/or distinctly higher mass concentrations of light-absorbing aerosol (>50 ng/m³) were used. Because the PE station was designed as zero-emission station, there was no relationship between wind speed or wind direction with elevated values for N_{CN} or light-absorbing aerosol. However, each hourly interval with wind speed < 3 m/s and/or wind direction outside the sector 20° to 225° was examined again on conspicuous signals in its variation in time.

3.2.2. Total Particle and CCN number concentrations and regional analysis of the NAME model footprints

This section presents the measured N_{CN} , N_{CCN} and $PNSD$ as well as the proportional residence time of the air masses over the regions introduced in Section 2.3.1. Time series are given for the three austral summer seasons of 2013/2014, 2014/2015 and 2015/2016 in Figure 3.15, 3.16 and 3.17, respectively.

Measurements of N_{CN} throughout the whole year were performed between 2012 and 2016. Figure 3.14 shows a clear seasonal cycle with the lowest monthly median values during the austral winter and a maximum during late austral summer. The monthly 10 % and 90 % percentiles also indicate the highest variability of N_{CN} during February. Several studies at different Antarctic sites found that the physical and chemical aerosol particle properties are subject to a similar seasonality e.g., Hara et al. (2011), Weller et al. (2011),

Virkkula et al. (2009) and Kim et al. (2017). Just like N_{CN} , also N_{CCN} follows a seasonal cycle with a minimum in austral winter and a maximum in austral summer (Kim et al., 2017). Hence, our measurements during austral summer capture the season in which the aerosol production in Antarctica and the surrounding source regions is most active.

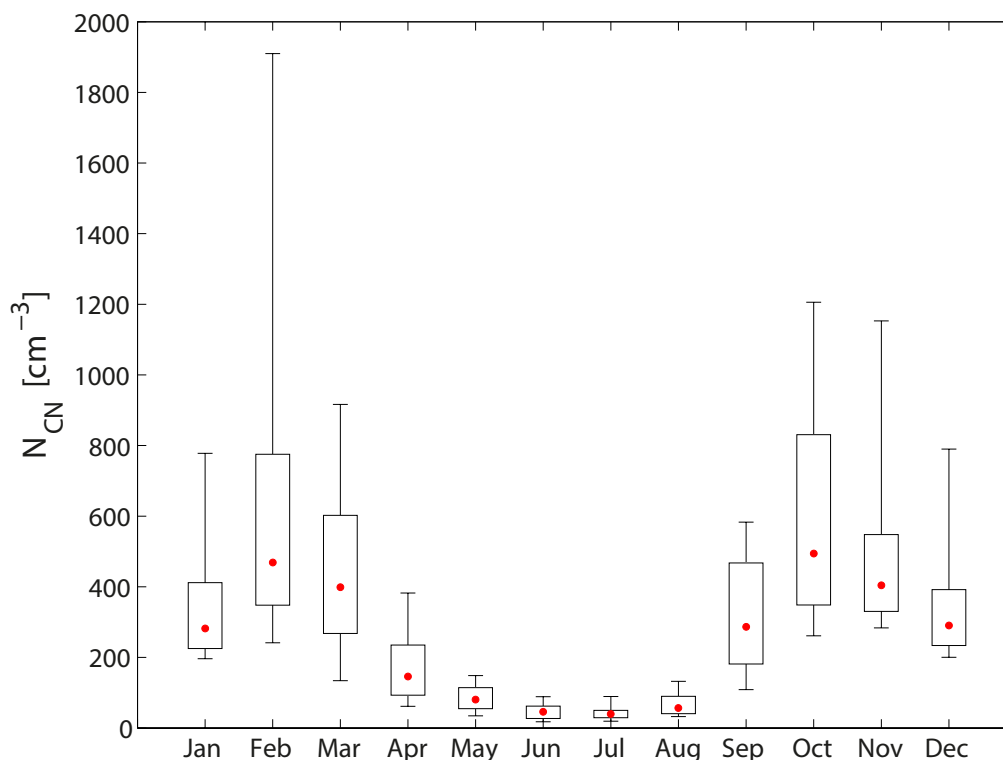


Figure 3.14.: **Antarctica - annual cycle of N_{CN}**

Box plot of monthly median values (red dots), interquartile range (black box) and 10 % and 90 % percentile (black bars) of N_{CN} measured at the PE station between 2012 and 2016.

N_{CN} (black dots in panel C Figure 3.15, 3.16 and 3.17) was found to cover a range between 40 and 6700 cm^{-3} (on the base of hourly averaged values) with a median value of 333 cm^{-3} . The measured N_{CCN} (bluish dots in panel C of Figure 3.15, 3.16 and 3.17) cover a range between less than 10 cm^{-3} at $SS=0.1\%$ to 1300 cm^{-3} for the highest SS of 0.7 %. The integration of the $PNSD$ over the whole size range ($N_{CN>90\text{nm}}$, red dots in panel C of Figure 3.15, 3.16 and 3.17) shows the aerosol particle number concentration in the size range between 90 nm and 6.8 μm . $N_{CN>90\text{nm}}$ has a median value of 20 cm^{-3} . The median, 10 and 90 % percentile values for N_{CN} , $N_{CN>90\text{nm}}$ and N_{CCN} at all measured SS are summarized in the first column of Table 3.3. O'Shea et al. (2017) and Kim et al. (2017) both also report N_{CCN} determined during austral summer, however, at coastal Antarctic locations. O'Shea et al. (2017) show N_{CCN} of approximately 20 cm^{-3} , 120 cm^{-3} and 250 cm^{-3} on average at 0.08 %, 0.2 % and 0.53 % SS , respectively, and

just under 200 cm^{-3} at 0.4 % SS are given in Kim et al. (2017). These N_{CCN} are roughly 50 % above those determined herein, across all supersaturations. This might be explained by our measurement site's larger distance to the Southern Ocean. As we will show below, air masses often traveled over Antarctica for extended times before reaching our measurement station, which might be connected to an increased wash out of particles by precipitation along the way.

The third column of Table 3.3 shows the ratio of $N_{\text{CN}>90\text{nm}}$ and N_{CCN} at different SS to N_{CN} (based on the median values of the first column in Table 3.3). The values of $N_{\text{CN}>90\text{nm}}/N_{\text{CN}}$ and $N_{\text{CCN},0.7\%}/N_{\text{CN}}$ are 0.06 and 0.64, respectively. This indicates, that the aerosol particles feature an Aitken mode dominance, as 94 % of the aerosol particles are smaller than 90 nm. Assuming a hygroscopicity parameter κ of 0.8 for the coastal area of East Antarctica, taken from Pringle et al. (2010), the critical diameter d_{crit} for SS = 0.7 % was determined by means of the κ -Köhler theory to be ≈ 35 nm. On the basis of this assumption 36 % of the aerosol particles are smaller than roughly 35 nm. That is indicative for a high amount of newly formed aerosol particles, which form from precursor gases emitted from the Southern Ocean and the Productive Zone as e.g., ammonia and DMS (see Section 2.3.1). The corresponding NPF events occurring during the passage of the air masses to the measurement site likely take place in the free troposphere (Fiebig et al., 2014; Quinn et al., 2017). Primary emitted natural aerosol particles that are known to occur in Antarctica from e.g., mineral dust (Wegner et al., 2015) or sea salt (Huang and Jaeglé, 2017; Yang et al., 2008; Wagenbach et al., 1998), are known to clearly exceed this size (Lamb and Verlinde, 2011). Unfortunately, we cannot examine the Aitken mode particles in much more detail, as our *PNSD* data is in the size range between 90 nm and $6.8 \mu\text{m}$ and hence only shows the accumulation and coarse mode particles. However, several other studies at coastal Antarctic sites report *PNSD* measurements that show pronounced and dominant Aitken modes during austral summer (e.g., Asmi et al., 2010; O'Shea et al., 2017; Kim et al., 2017).

Panel D of Figure 3.15, 3.16 and 3.17 shows the regional analysis of the NAME footprints, as described in Section 2.3.1. It can give insights on the influence of the air mass origin on N_{CN} and N_{CCN} . The regional analysis shows, that during the 10 days prior to the measurements, air masses only have been influenced by the Antarctic continent, the Southern Ocean and the Productive Zone region but not by South America or Africa. Thus, it can be assumed, that mainly pristine air masses and aerosol particles of a natural origin without much anthropogenic influence were examined.

The contributions from Antarctica, the Southern Ocean and the Productive Zone region show a large variability. During 61 % of the measurement times, the air masses spent ≥ 90 % of the 10 days prior to their arrival at the measurement site over the continental region. These times are called Continental Events (CEs) from now on. During CEs, only

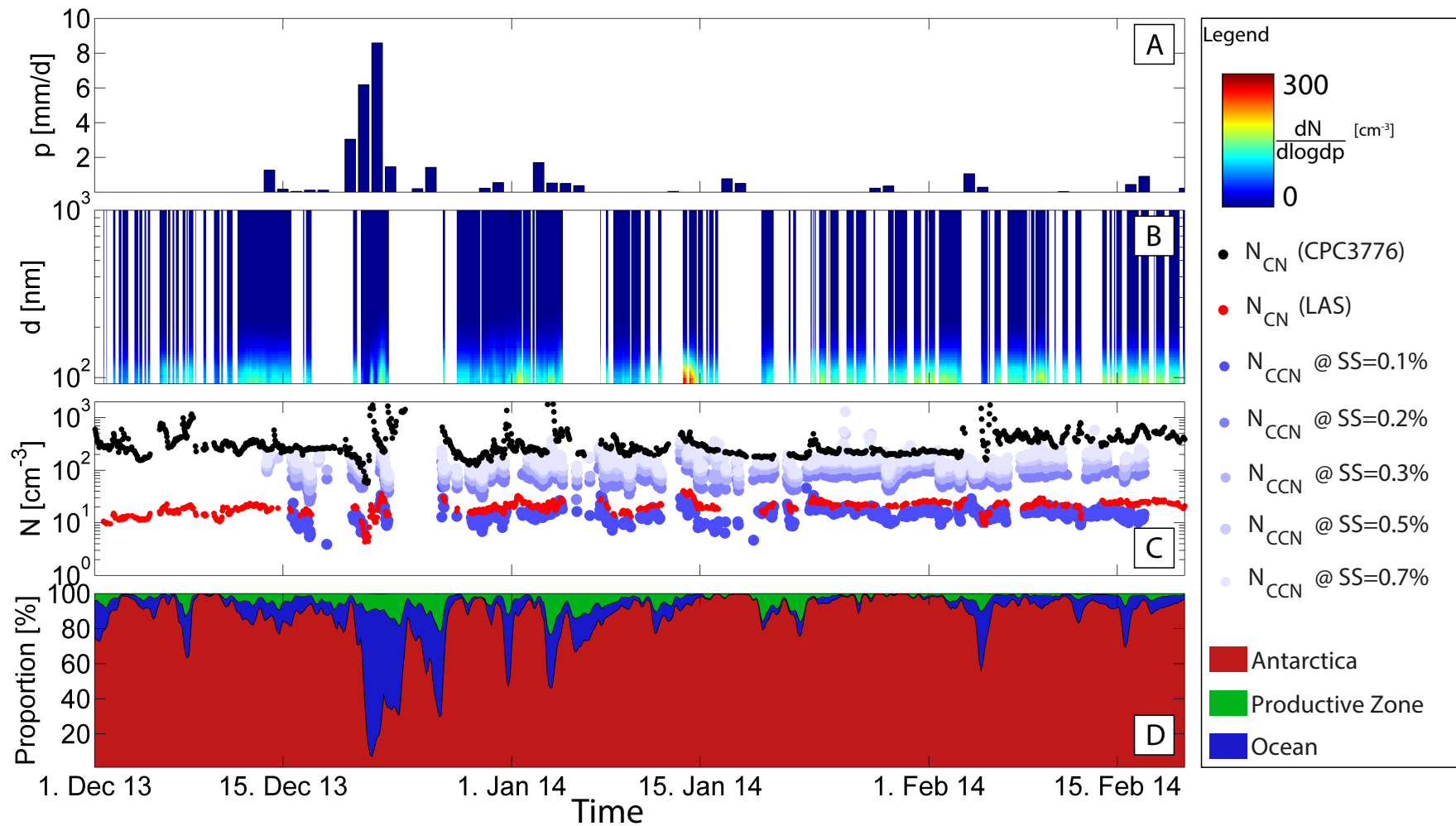


Figure 3.15.: **Antarctica - time series of measured properties 2013/14**

Time series of the first season (December 2013 to February 2014) of a) daily precipitation shown as bars (same data as in Figure 3.13), b) $PNSD$, depicted between 90 nm and 1 μm , c) N_{CN} measured by the CPC in black, N_{CN} measured by the LAS (integrated concentration between 90 nm and 6.8 μm) in red and N_{CCN} measured by the CCNC at SS between 0.1 and 0.7% in different blue colors, d) proportion of residence of the air masses over the Antarctic continent (red area), the Reactive Zone (green area) and the Southern ocean (blue area) areas during the past ten days (based on the NAME model footprints).

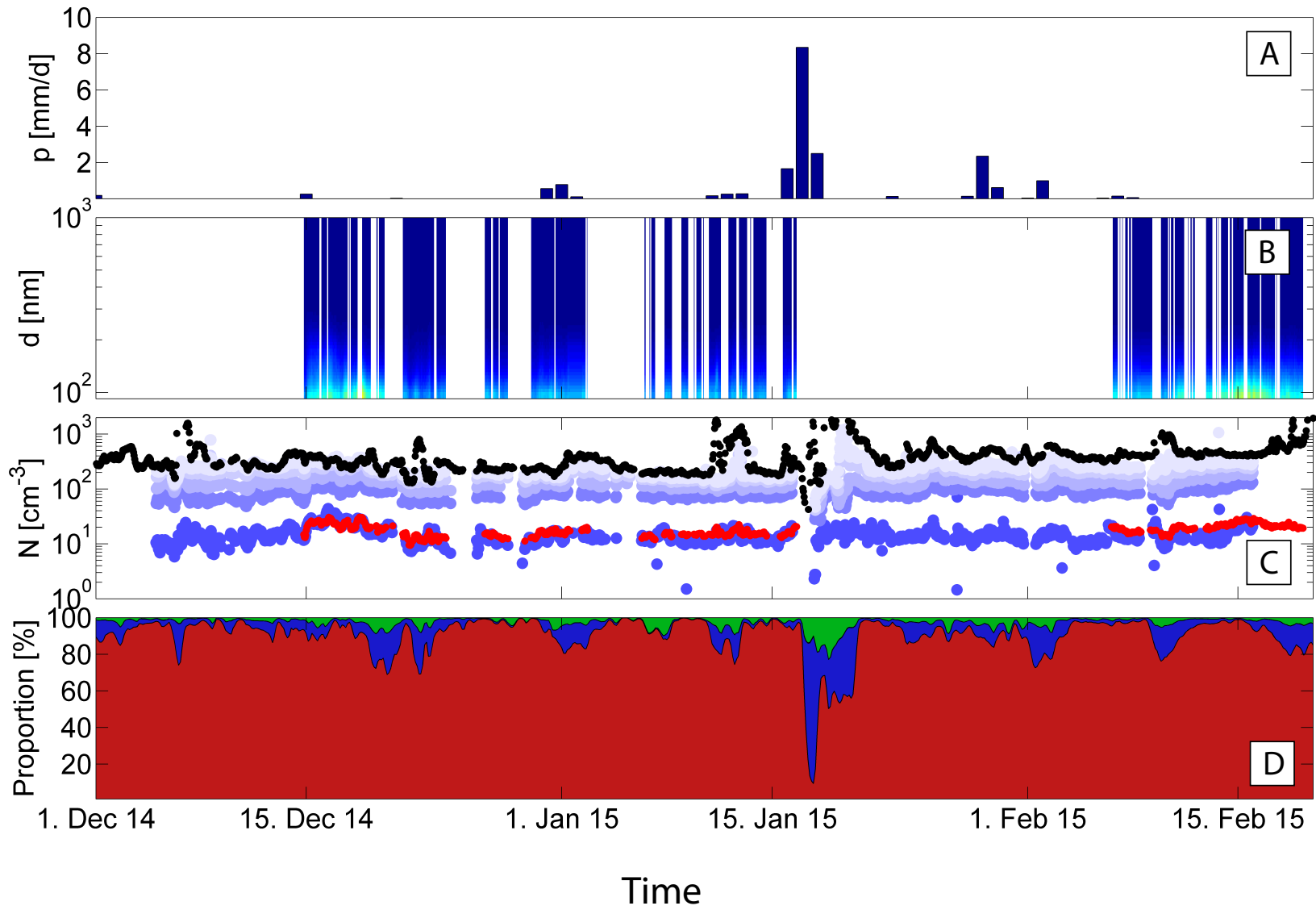


Figure 3.16.: **Antarctica - time series of measured properties 2014/15**

Time series of the second season (December 2014 to February 2015). For further details see caption of Figure 3.15.

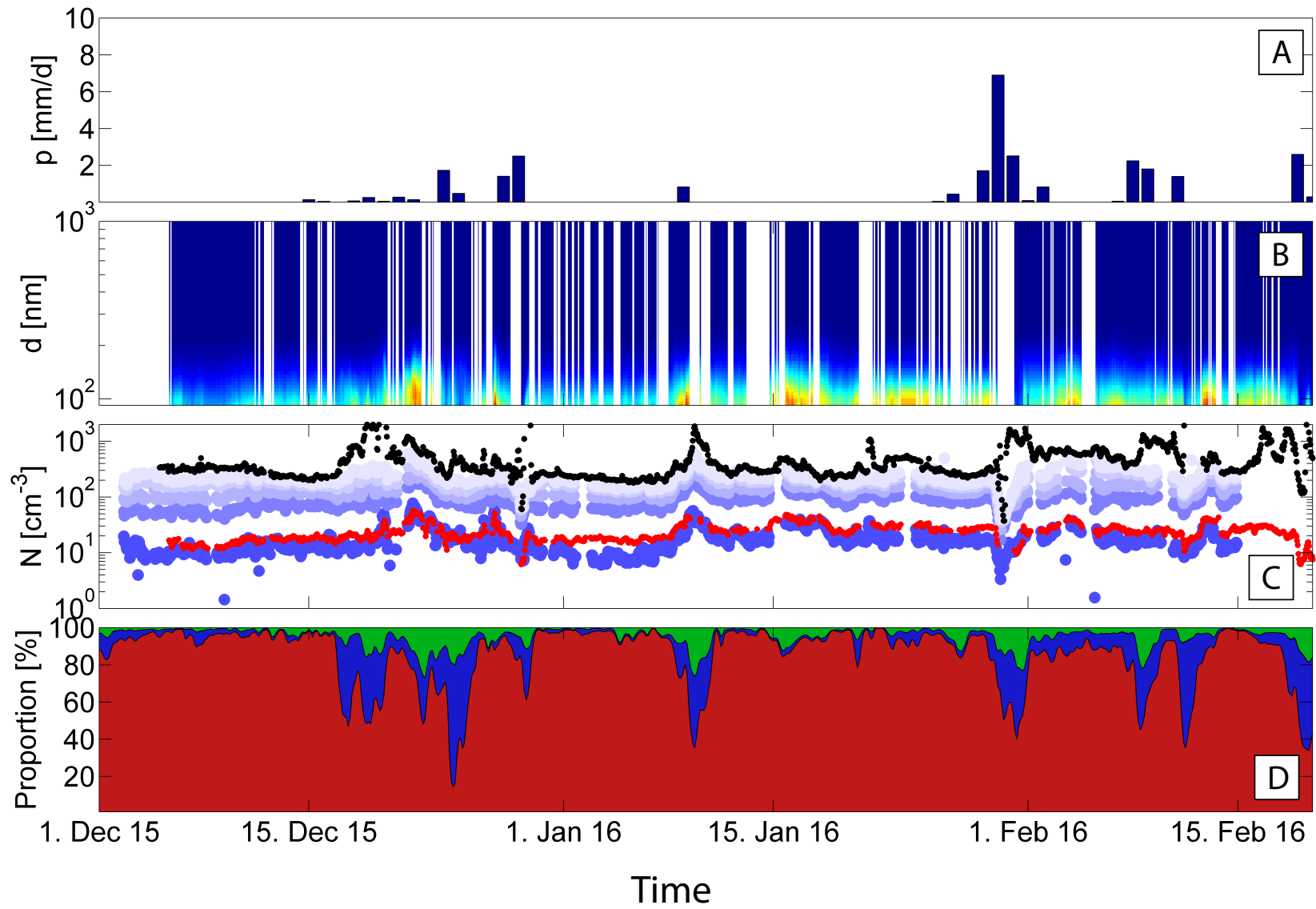


Figure 3.17.: Antarctica - time series of measured properties 2015/16

Time series of the third season (December 2015 to February 2016). For further details see caption of Figure 3.15.

a low variability in the measured N_{CN} and N_{CCN} was recorded. To illustrate this, the different panels of Figure 3.18 show scatter plots and box and whisker plots, displaying N_{CN} and N_{CCN} (the latter at the two exemplary supersaturations of 0.3 % and 0.7 %) versus the fraction of time that the respective air masses spent over the Antarctic region (continental fraction). All data from the three seasons are included. It can clearly be seen panel a) and b) of Figure 3.18 that N_{CN} scatters the least and reaches the lowest median value during CEs (note: only few data points exist for the low continental fractions, up to roughly 30 %, making their median and percentiles statistically unreliable). During CEs, N_{CN} rarely exceeds 475 cm^{-3} , with maximum values of 990 cm^{-3} , while 90 % of N_{CN} cover a range from 170 to 475 cm^{-3} . The concentration ranges during CEs for N_{CN} , $N_{\text{CN}>90\text{nm}}$ and N_{CCN} at all SS are shown in the second column of Table 3.3. These concentration ranges can be assumed to be pristine Antarctic continental background concentrations during austral summer.

During 39 % of the time the proportion of the Productive Zone plus the Southern Ocean region was larger than 10 %, which from now on are called Marine Events (MEs). During MEs an enhanced variability in N_{CN} and N_{CCN} was recorded. Also the precipitation, depicted in panel A of Figure 3.15, 3.16 and 3.17, shows a connection to MEs. Especially strong precipitation events only occur during certain most intense MEs affecting PE, e.g., on December 21 in 2013, January 18 in 2015 and January 30 in 2016, in line with the findings of Gorodetskaya et al. (2014) and Souverijns et al. (2018). These precipitation events significantly decrease N_{CN} and N_{CCN} on a time scale of some hours to one day, due to scavenging and wet deposition. The minimum values that are reported for N_{CN} and N_{CCN} were measured during these strong precipitation events. As the Antarctic region does not act as a significant source of water vapor (see katabatic meteorological regime in Section 3.2.1) it is self-explanatory that strong precipitation events only occur during MEs. But also the highest values for N_{CN} and N_{CCN} are only observed during MEs. The Productive Zone and the Southern Ocean region potentially represent source regions for primary and secondary formed aerosol particles. As already mentioned in Section 2.3.1 the region of the Productive Zone can contribute to the Antarctic aerosol particle loading due to sea bird and penguin guano and microbiota occurring in open meltwater ponds and related to sea ice, all connected to the release of ammonia that potentially contributes to the formation of new particles (Legrand et al., 1998; Kyrö et al., 2013; Schmale et al., 2013; Dall'Osto et al., 2017b). Maybe more importantly, the Productive Zone and the Southern Ocean region also emit DMS, whose oxidation products sulfuric and methane sulfonic acid similarly contribute to NPF and have the ability to form aerosol particles that grow to CCN sizes (Liss and Lovelock, 2008). Also, these regions have the potential to contribute to the aerosol particle loading by primary emissions of sea salt particles due to blowing snow on sea ice surfaces (Huang and Jaeglé, 2017; Yang et al., 2008; Wagenbach et al., 1998) or bubble bursting from wave action (Lamb and Verlinde, 2011).

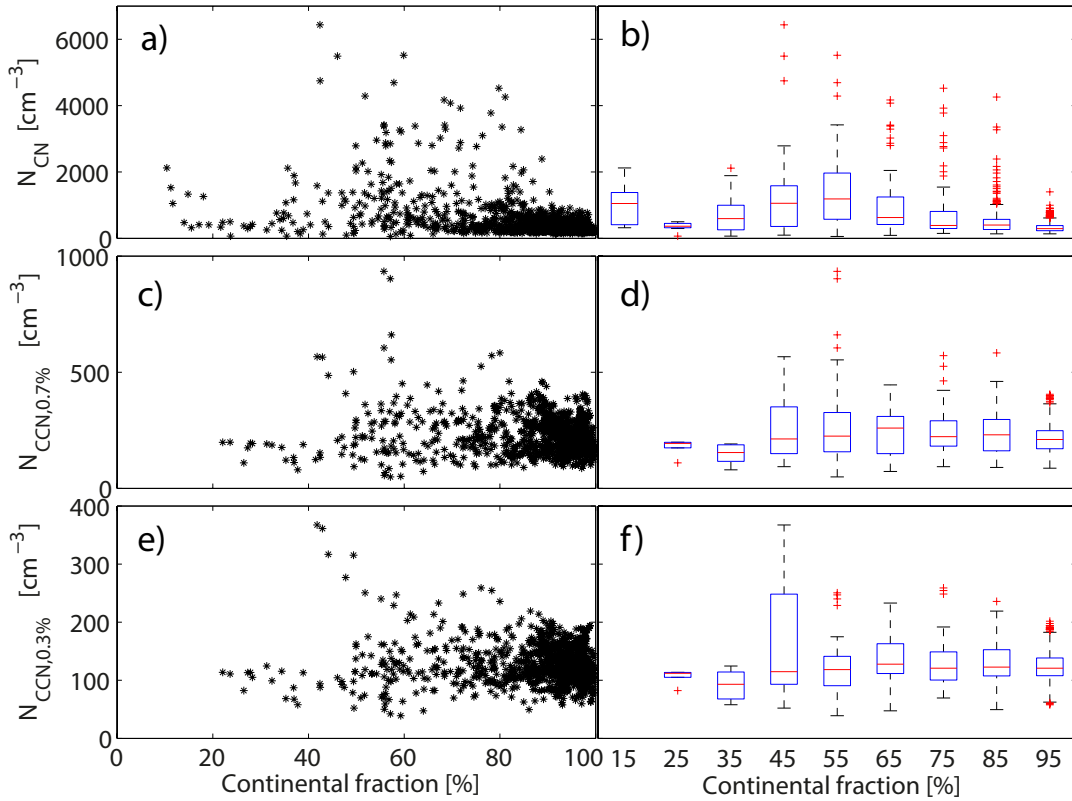


Figure 3.18.: **Antarctica - Connection between N_{CN} and the occurrence of continental air masses**

Connection between N_{CN} and N_{CCN} (at supersaturations of 0.3 % and 0.7 %) and the occurrence of continental air masses. While panels a), c) and e) show the data separately, panel b), d) and f) give a box and whisker plot with median values and the interquartile range (blue boxes).

The time series of N_{CN} in Figure 3.15, 3.16 and 3.17 often show a spontaneous increase during MEs of several thousand particles per cm^3 . Figure 3.19 exemplarily shows such an event, that took place on December 6 in 2014. Between 7 and 10 a.m. N_{CN} increased from ≈ 200 to $\approx 6000 cm^{-3}$. This was accompanied by an increase of N_{CCN} . In total 12 comparable events with an increase of N_{CN} up to several thousand cm^{-3} were detected that all took place in a time frame between several hours and ≈ 1 day. In the vast majority these events of increased N_{CN} were followed by an increase of N_{CCN} by a factor of roughly two, in three cases even by an increase of more than a factor of 10. This only holds for N_{CCN} measured at SS between 0.2 %-0.7 %. N_{CCN} measured at a SS of 0.1 % usually show a different trend and seem to be decoupled from the other measurements. Other studies at Antarctic sites report events of NPF during austral summer, e.g., Asmi et al. (2010) and Weller et al. (2015) at the Finnish research station Aboa and the German Neumayer station, respectively, which are both coastal sites. Järvinen et al. (2013) even reported the observation of NPF at Dome C, a site in Central Antarctica. Median growth rates of

particles from NPF were ≈ 2.5 nm/h at Dome C throughout the year, and 3.4 nm/h and 0.6 nm/h for particles up to and above 25 nm, respectively, in the austral summer. At Aboa, variable growth rates were reported, ranging from 0.8 nm/h to 2.5 nm/h reported in Asmi et al. (2010) and from 1.8 nm/h to 8.8 nm/h derived in Kyrö et al. (2013), while growth rates were only ≈ 1 nm/h for the coastal site of Neumayer (Weller et al., 2015). While it was also described that particles rarely grew to sizes larger than ≈ 25 nm at Neumayer (Weller et al., 2015), i.e., that they do not reach sizes at which they can readily act as CCN, growth of newly formed particles into the CCN size range was reported for Aboa, likely due to precursor emissions from local meltwater ponds (Kyrö et al., 2013) or due to precursor gases advected to the site with marine/coastal air masses (Koponen et al., 2003). The surprisingly high growth rates observed at Dome C may be related to air masses that had picked up precursor gases for the formation of particulate matter over the Southern Ocean or the region defined as Productive Zone herein, and that were subsequently transported in the free troposphere followed by descent over Antarctica (Fiebig et al., 2014). This likely is a process occurring widely spread in Antarctica, for which not the availability of precursor gases but rather the photooxidative capacity regulates the connected NPF and particulate growth (Fiebig et al., 2014). Tropospheric NPF with subsequent growth therefore likely also explains the above described observations at the PE station.

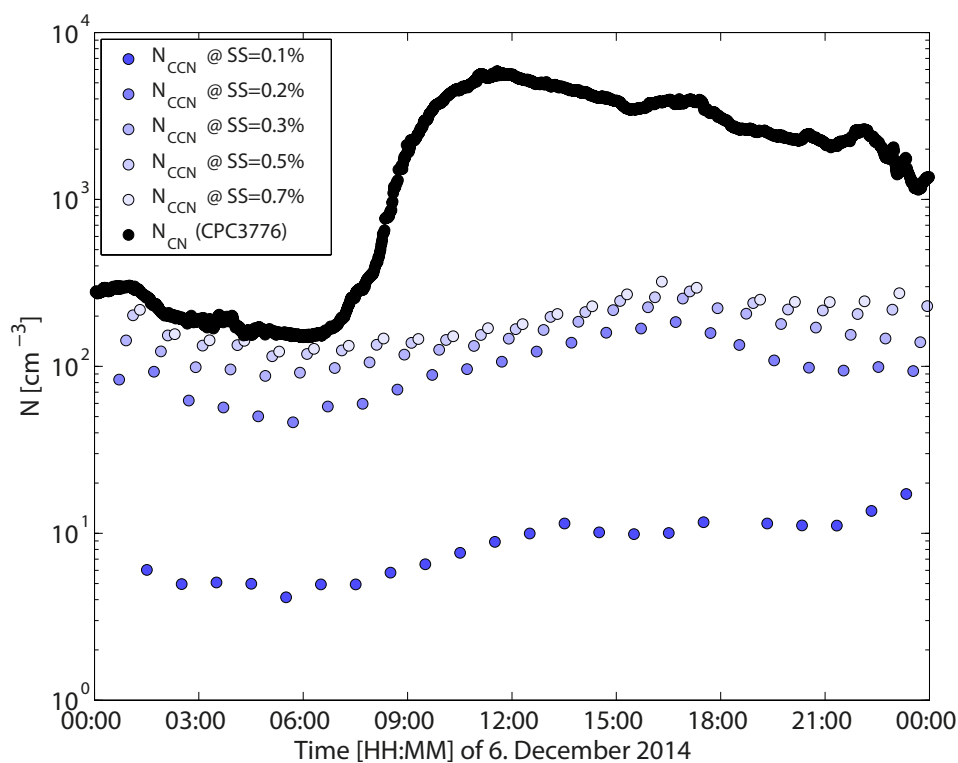


Figure 3.19.: **Antarctica - example of new particle formation**
 N_{CN} and N_{CCN} during an event of new particle formation at the PE station.

The measured *PNSDs* do not cover the size range of the nucleation and Aitken mode, however, in combination with measurements of N_{CN} and N_{CCN} it can be stated that comparably freshly formed particles originating from new particle formation events were observed during our measurements. Our measurements at the PE station show, that these freshly formed aerosol particles seem to reach size ranges relevant for CCN activation and thus are climatically relevant.

3.2.3. PSCF results

Figure 3.20 shows the spatial distribution of the PSCF calculated for N_{CN} , $N_{\text{CN}}-N_{\text{CCN},0.7\%}$, $N_{\text{CCN},0.7\%}$ and $N_{\text{CCN},0.1\%}$. These four parameters represent concentrations of all particles (with a lower size cut at 3 nm), particles in the size range up to ≈ 35 nm, particles with sizes above ≈ 35 nm and the largest particles above ≈ 110 nm, respectively. The analysis was done using the data of all three austral summer periods, which is a data set of approximately 230 days and a corresponding set of 88152 back trajectories. The 75 % percentile values of N_{CN} , $N_{\text{CN}}-N_{\text{CCN},0.7\%}$, $N_{\text{CCN},0.7\%}$ and $N_{\text{CCN},0.1\%}$, on the basis of which the PSCF analysis was done, are 466, 184, 268 and 13, respectively. High values in the maps in Figure 3.20 indicate, which regions have a high potential to contribute to the 25 % of the highest number concentrations measured at the receptor site. The PSCF of N_{CN} shows enhanced values over the region of the Southern Ocean, mostly between 60° S and 40° S, but not over the Antarctic continental region. Hence, the Southern Ocean is likely to be the dominant source region leading to an enhancement in N_{CN} measured at PE, while the Antarctic continent itself is not likely to act as a particle source. This is in accordance with results discussed in Section 3.2.2, i.e., the low variability of measured number concentrations during CEs and the occurrence of high values of N_{CN} observed for air masses connected to MEs.

$N_{\text{CN}}-N_{\text{CCN},0.7\%}$ and $N_{\text{CCN},0.7\%}$ are two complementary parameters, adding up to N_{CN} . The PSCF maps of $N_{\text{CCN},0.7\%}$ and $N_{\text{CN}}-N_{\text{CCN},0.7\%}$ show clearly distinct patterns, indicating that different source regions are likely to contribute to high concentrations of particles with sizes below and above ≈ 35 nm. However, both share that their highest signals are again in the Southern Ocean between 60° S and 40° S, however, at different longitudes. The PSCF of $N_{\text{CN}}-N_{\text{CCN},0.7\%}$ (particles with sizes below ≈ 35 nm) shows a large area of high signals between 40° W and 60° E. When calculating transport times based on air mass back trajectories, an average transport time of 5.1 days from this area to PE station is obtained. The PSCF of $N_{\text{CCN},0.7\%}$ (particles with sizes above ≈ 35 nm) shows the largest area of high signals in a region between 140° W and 80° W, for which the average transport time to the PE station is 8.8 days. These air masses usually travel either along the west wind drift through the Drake Passage and circumnavigate Antarctica

3.2. Measurements of aerosol and CCN properties at the Princess Elisabeth Antarctica Research Station during three austral summers

before making landfall close to PE station, or they travel along the easterly winds over coastal East Antarctica till they reach the PE station. This is consistent with the predominance of the easterly wind component during synoptically driven MEs (Gorodetskaya et al., 2013; Souverijns et al., 2018). As already discussed in Section 3.2.2, the aerosol observed at the PE station features a dominant Aitken mode. This can be brought in line with the results discussed here. The aerosol particles that originate from the marine areas that show up dominantly in the PSCF likely are mainly secondary aerosol particles that grow during the transport to the PE station. The size of the measured aerosol particles can be assumed to be a function of average transport time, corresponding to source regions for larger particles that are further away (when considering air mass traveling times).

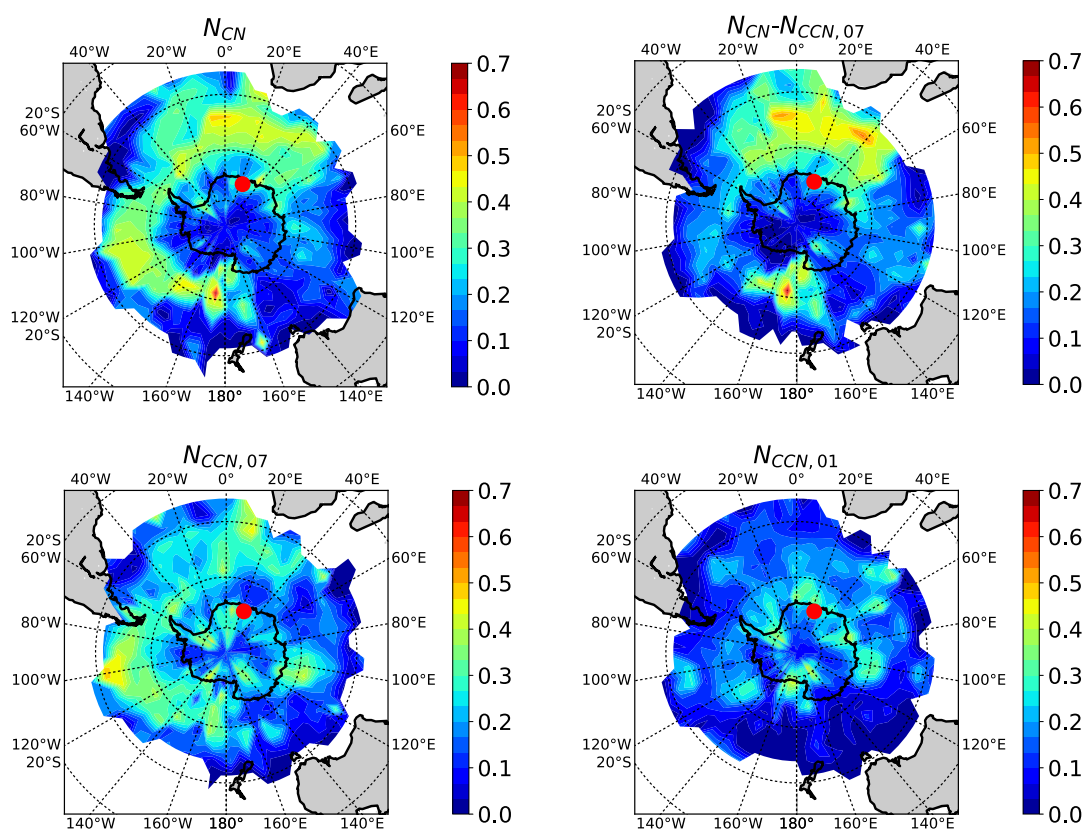


Figure 3.20.: **Antarctica - PSCF results**

PSCF results that are plotted over a map of Antarctica for N_{CN} , $N_{CN}-N_{CCN,0.7\%}$, $N_{CCN,0.7\%}$ and $N_{CCN,0.1\%}$. The colorbar indicates the value of the PSCF.

The PSCF map for $N_{CCN,0.1\%}$ differs from the others. Overall, values are lower, pointing towards a more uniformly distributed origin of particles with sizes above ≈ 110 nm. But it should also be stressed that values for $N_{CCN,0.1\%}$ are generally low (see Table 3.3). The PSCF map shows almost no areas of enhanced values over the Southern Ocean, but several spots of comparably enhanced values show up along the coast of Antarctica, i.e., over the Productive Zone region. The overlap between these spots and the different shelf ice areas that are shown in Panel d of Figure 3.12 is noteworthy. The PSCF shows significantly

increased values at the locations of the Ross, Ronne-Filchner and Amery shelf ice (1, 2 and 6 in Panel d of Figure 3.12), and slightly increased values at the location of the Fimbul, West and Shakleton shelf ice (5, 7 and 8). Hence, the Antarctic shelf ice regions seem to be potential source regions for enhanced values of $N_{CCN,0.1\%}$. This will be elaborated further in the next section.

3.2.4. Hygroscopicity

For the data set presented here, the hygroscopicity parameter κ can only be inferred for $SS=0.1\%$, for which the median d_{crit} was determined to be 110 nm. For higher SS , N_{CCN} is above $N_{CN>90nm}$, i.e., d_{crit} is below the lower size limit of the measured *PNSD*. Therefore, the hygroscopicity derived here is only valid for the low number of comparably large particles that are activated at 0.1% (see Table 3.3). All κ values from the three seasons have a median value of 1 and are shown in a histogram in Figure 3.21. These are generally high atmospheric κ values covering a broad range between 0.5 and 1.6. Separate analysis of κ for CEs and MEs results in 0.99 ± 0.18 (to which 64% of all separate κ values contribute) and 1.05 ± 0.20 , respectively. There is no clear difference in hygroscopicity of the here analyzed large particles of roughly 110 nm, independent of the time the air mass had been over the continent. This points towards common sources of these large particles for both, CEs and MEs, which are discussed in the following.

Large κ values as those observed here typically are only found for particles consisting of inorganic substances (Petters and Kreidenweis, 2007). Particularly values of roughly 1 or above are only known to occur for sea salt. 0.95 was reported in Wex et al. (2010) as the mean value for the sea spray signal in marine air masses, derived from a collection of ambient hygroscopic growth measurements. Zieger et al. (2017) give a value of 1.1 for inorganic sea salt particles at 90% relative humidity, and Petters and Kreidenweis (2007) give mean values of 1.12 and 1.28 for NaCl, based on hygroscopic growth and CCN measurements, respectively. (It may be worth noting that κ derived from hygroscopic growth typically is below that derived from CCN measurements, see Petters and Kreidenweis, 2007). The lower values derived for κ are too low to originate from pure sea salt particles. In addition to inorganic compounds, marine aerosol particles may also contain internally mixed organic substances which reduce their hygroscopicity (Swietlicki et al., 2008). Secondarily formed aerosol particles of marine origin are a result of DMS oxidation and further reactions. They can be expected to contain sulfates, and Petters and Kreidenweis (2007) give a κ value of 0.61 for ammonium sulfate, derived from CCN measurements. Overall, the range of κ values derived for particles with sizes of ≈ 110 nm indicates that they are mostly composed of inorganic substances. While the lowest κ values determined in this study point towards a contribution of sulfate containing particles in the here examined particle size range of around 110 nm, the median κ of

1 might even point towards a dominance of sea salt. This agrees with sea spray particles being generally larger in size, compared to particles formed during NPF and growth, so that they might contribute to particles in this size range. It also agrees with an observation made at the Aboa research station, where sodium chloride was found for larger particles with sizes above 100 nm (Teinila et al., 2000).

Before the results of this study are compared to literature, it is necessary to mention that the uncertainty of the κ values was inferred with a method based on Monte Carlo simulations as described in Herenz et al. (2018) and Kristensen et al. (2016). In this approach, uncertainties of input parameters needed for the calculation of κ are combined, namely the uncertainties for particle sizing and counting as well as for the supersaturation adjusted in the CCNC. During Monte Carlo simulations, these parameters are randomly varied within their uncertainty range during a large number of separate runs (10000 runs in this study) to yield the uncertainty of the derived κ based on the uncertainty of the input parameters. This analysis shows that the uncertainties in our κ values are in the same order than the variability of the values itself, i.e., the uncertainty in the derived κ values can be explained based on measurement uncertainties. This allows no interpretation of the variability in κ with respect to different air mass origins.

A few other studies already examined the hygroscopicity of Antarctic aerosol particles, as well as the impact of sea ice regions on it. During the PEGASO ship cruise that took place in the austral summer in 2015 in the proximity of the Antarctic Peninsula and the Filchner-Ronne ice-shelf, Dall'Osto et al. (2017b) found an increased N_{CN} (aerosol particles larger than 3 nm) within air masses with an origin over sea ice regions in comparison to air masses that originated over open water. Other studies further suggest, that sea ice regions efficiently emit sea salt aerosol particles, e.g., Huang and Jaeglé (2017); Yang et al. (2008); Wagenbach et al. (1998). O'Shea et al. (2017) measured CCN at the Halley research station, ≈ 30 km from the Weddell Sea on the Brunt Ice Shelf. They report a median κ value of 0.66 during measurements in December for five different SS (0.08, 0.2, 0.32, 0.41, 0.53 %). Also, they had an event of a median κ value of 1.13 during two days when back trajectories indicate that air masses had passed over sea ice regions of the Weddell Sea. This is indicative for ice surfaces being able to emit aerosol particles with a high hygroscopicity and is in line with our findings. Pringle et al. (2010) applied the ECHAM-MESSy Atmospheric Chemistry (EMAC) model to simulate the global distribution of κ at the surface. That study results in values between 0.6 and 0.9 for Antarctic coastal areas and >0.9 for the Southern Ocean region. Asmi et al. (2010) measured the hygroscopicity of Antarctic aerosol particles at the Aboa station using a Hygroscopicity-Tandem Differential Mobility Analyser. They also found the Antarctic aerosol particles to be very hygroscopic with an average hygroscopic growth factor of 1.63, 1.67 and 1.75 for 25, 50 and 90 nm particles, respectively, at 90 % RH, which is similar to the hygroscopic growth factor of ammonium sulfate particles at 90 % RH (given as 1.64, 1.68 and 1.71 for

these three different sizes in Asmi et al., 2010). Unlike these studies and our findings, Kim et al. (2017) report a lower particle hygroscopicity. Their results are based on CCN and *PNSD* measurements that were conducted at the King Sejong Station in the Antarctic Peninsula between 2009 and 2015. For CCN measurements at a *SS* of 0.4 % they found an annual mean κ value of 0.15 ± 0.05 , which, however, is the only time such low κ values were reported for Antarctica.

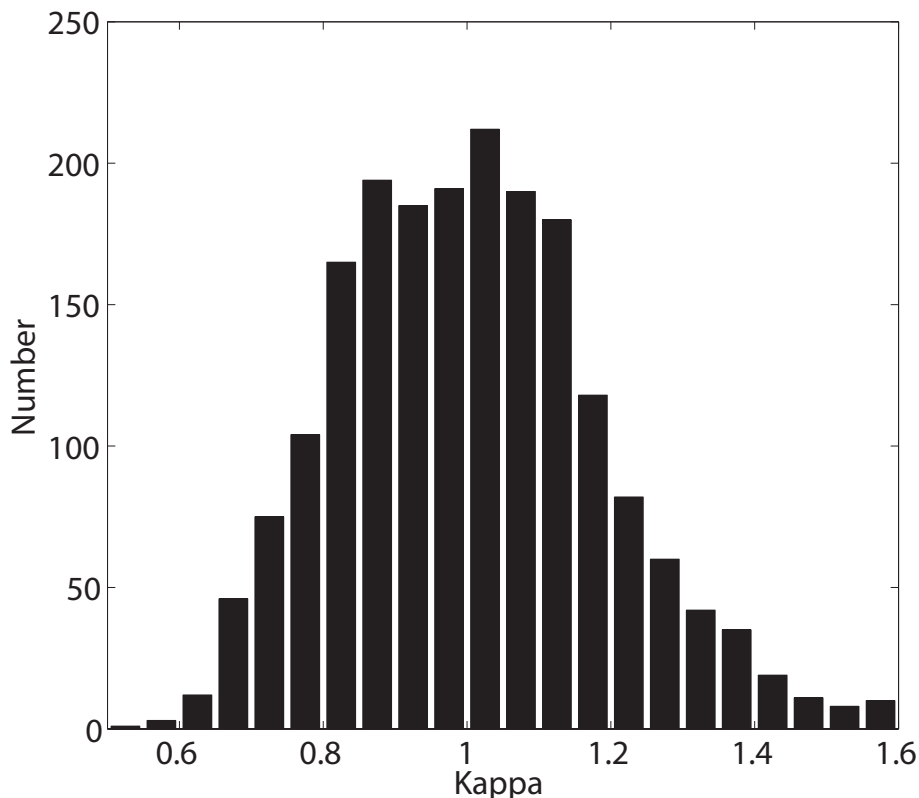


Figure 3.21.: **Antarctica - κ results**
Histogram showing the 2171 κ values of all three seasons.

Summarizing, it can be concluded that the few large aerosol particles that were observed for sizes of and above ≈ 110 nm may partially originate from NPF and subsequent growth. In this respect, it should also be explicitly mentioned that cloud processing of particles also adds mass to those particles that are activated to cloud droplets (Ervens et al., 2018, and references therein), potentially aiding the growth of particles formed by NPF into the here discussed size range. However, particulate mass added during cloud processing will not have κ values above these of sulfates. Therefore, the majority of these aerosol particles in the size range of ≈ 110 nm likely consist of sea spray particles originating from the open ocean or of sea salt particles emitted over sea ice regions, a statement that is based on their comparably high κ values. This fits to the results presented for $N_{CCN,0.1\%}$

3.2. Measurements of aerosol and CCN properties at the Princess Elisabeth Antarctica Research Station during three austral summers

in Section 3.2.3, showing the marine areas in coastal proximity and especially the shelf ice regions as potential source regions.

4. Summary, Conclusions and Outlook

In view of the fast climatic relevant changes that currently take place in the Arctic and Antarctic enormous scientific effort was, is and still needs to be made to capture these changes by collecting numerous data sets of relevant parameters. Long time series covering several years and full yearly cycles are extremely valuable as they can be used to document ongoing changes. Short time data sets are desirable as they document the situation at a specific time period during the change and allow for more detailed process studies. The data presented and analyzed in this thesis belong to the latter kind and were realized as a part of BACCHUS, which is a collaborative European research project. One of the project's primary objective is the characterization of aerosol particles in regions that are key regulators of the Earth's climate as well as regions that experience the most intense climate changes with possible irreversible transitions. The Arctic and the Antarctic are such regions. In the framework of this doctoral thesis two data sets were recorded, that enable a basic characterization of the current conditions of the spring and summer time aerosol particles and CCN in the Canadian Arctic and the East Antarctic.

Arctic CCN and aerosol particle properties were measured during the RACEPAC campaign in May 2014. Due to the occurrence of local pollution, a filtering procedure had to be applied before the data set was further evaluated to obtain estimates for the background conditions. The local pollution caused peaks in up to more than 10000 cm^{-3} with a typical temporal duration of 1 to 5 minutes in N_{CN} . A comparison of the $PNSDs$ of the polluted and the unpolluted periods shows that the local pollution significantly contributed to the measured particle number concentration below a size of 150 nm. As a consequence of this, N_{CCN} and κ obtained for $SS = 0.1\%$ could be analyzed for the whole measurement period, as these were not affected by pollution events of particle sizes below 150 nm, while N_{CCN} and κ at all other measured SS as well as the $PNSDs$ were analyzed for three distinct time periods only, during which local pollution did not affect the measurements. 10 day back trajectories that were computed for the three periods showed that air masses from two different origins were investigated. Air masses with an origin in North-East Canada were typically dominated by Arctic haze. The corresponding mono-modal $PNSD$ shows an accumulation mode which most likely contains well aged particles that have an

Eurasian origin (Behrenfeld et al., 2008). The other origin is the region of the North Pacific and Eastern Russia. The corresponding bi-modal *PNSD* shows an additional mode of smaller particles that may be attributed to new particle formation and growth potentially due to oxidation products of marine emissions of DMS (Engvall et al., 2008; Wiedensohler et al., 2011). This variability in the *PNSD* is typical for the transition from Arctic spring to summer during April, May and June (Engvall et al., 2008). Further, the PSCF receptor model was applied to identify possible source regions for aerosol particles measured at Tuktoyaktuk. It was found that air masses having their origin in active fire areas in Central Canada and Siberia, in areas of industrial anthropogenic pollution (Norilsk and Prudhoe Bay Oil Field) and in the area of the North-West Pacific cause enhanced N_{CN} values. Thus, these regions are considered to be potential source regions of Arctic aerosol particles. CCN number concentrations were found to cover a range between less than 10 and 250 cm^{-3} for *SS* between 0.1 and 0.7 %, respectively.

Applying the κ -Köhler theory (Petters and Kreidenweis, 2007) the hygroscopicity parameter κ was inferred. The median κ of all *SS* and all three periods is 0.23. At *SS* = 0.1 %, for which the whole measurement period could be evaluated, a mean κ of 0.19 was found. The estimated random errors typically exceed the observed variation in the observed κ values. Consequently, it was not possible to distinguish κ values related to different air masses or particle sizes. The here reported κ values and those reported in other Arctic springtime studies e.g., Kammermann et al. (2010); Moore et al. (2011); Latham et al. (2013) fit together and do rarely exceed 0.3. But, these studies explain hygroscopicity variations by different types of air masses (Moore et al., 2011; Latham et al., 2013) or special circumstance in the surrounding of the measurement station like the local proximity to the Stordalen mire in Kammermann et al. (2010). In this thesis, however, observed variations of the κ values are explained by the uncertainties of the measurement and data evaluation methods. Note, comparable instruments and methods were used in these studies. Due to the findings of this thesis it is highly recommended to apply a robust analysis of the uncertainties in the κ evaluation to not over interpret results. Furthermore, with regard to only a few existing κ -data sets the large Arctic area is temporally and locally undersampled, so that it is highly suggested to conduct further measurements. For this purpose a CCNC of the Cloud Group of the Leibniz Institute for Tropospheric Research is permanently installed at Greenland, Station Nord (since 2018), recording the seasonal cycle of N_{CCN} at different *SS*. Together with simultaneous *PNSD* measurements, this will allow to examine the seasonal cycle of the hygroscopicity of Arctic aerosol particles.

Simultaneous measurements at the ground based measuring station in Tuktoyaktuk and on the research aircraft Polar 6 show a qualitatively good agreement of ground based *PNSDs* with *PNSDs* of the lowest tropospheric layers (up to 1200 m when measurements at this height were present) during four overflights. Hence, it can be excluded that local natural sources contribute significantly to the ground based measurements during the

observed time period and that the ground based measurements of $PNSD_{cs}$ (without influence of local pollution) are representative for the atmospheric boundary layer in the area of Tuktoyaktuk during the measurement period. Moreover two profile flights show that the $PNSDs$ measured inside and above the atmospheric boundary layer can vary in shape and integrated particle number concentration. The largest particle number concentrations were observed in the highest layer (3000 m). It can be assumed that the aerosol is advected via long range transport from lower latitudes in different height layers and mixed down in the lower Arctic troposphere. This may originate in different sources for the particles found in different altitudes. Stone et al. (2014) explained that the transport of emissions from distant source regions to the Arctic in the spring months happens at different layers depending on the latitude of release. The airborne $PNSD$ measurements indicate such different layers, that however can not be investigated in detail. On the basis of this data it strongly is suggested to consider height resolved aerosol particle measurements in and above the Arctic boundary layer as subject for future investigations. A better understanding of how anthropogenic long range transported emissions enter the Arctic atmosphere and change the prevailed aerosol particle conditions is a major puzzle to understand the role of aerosol particles in Arctic climate change.

Antarctic CCN and aerosol particle properties were measured at the Belgian Antarctic research station Princess Elisabeth (PE), in Dronning Maud Land in East Antarctica. During three austral summer seasons (2013-2016, each from December to February) the total aerosol particle number concentration and size distribution as well as the total CCN number concentration at 5 different supersaturations inside the East Antarctic boundary layer were measured. An automatic weather station, that is installed in the vicinity of the PE station, and a precipitation radar were used to gain further information about the meteorological conditions. The history of the measured air masses arriving at the PE station was modeled by using the NAME dispersion model and the PSCF model, that is based on HYSPLIT back trajectories.

N_{CN} was found to range between 40 and 6700 cm^{-3} with a median of 333 cm^{-3} . For particles larger than 90 nm ($N_{CN>90nm}$) a median concentration of 20 cm^{-3} was found. N_{CCN} covers a range between less than 10 cm^{-3} at $SS=0.1\%$ and 1300 cm^{-3} for the highest SS of 0.7%. The median values of N_{CCN} for supersaturations of 0.1, 0.2, 0.3, 0.5 and 0.7% are 14, 81, 121, 177 and 212 cm^{-3} , respectively. All of the previous values are calculated on the basis of the entire measurement period of three austral summers. The ratios of $N_{CN>90nm}/N_{CN}$ and $N_{CCN,0.7\%}/N_{CN}$ indicate that 94% and 36% of the particles are smaller than 90 nm and ≈ 35 nm, respectively. From this it can be concluded, that an Aitken mode dominated aerosol prevailed, that likely includes a significant amount of secondarily formed aerosol particles.

The fluctuations in N_{CN} and N_{CCN} can be associated with the history of the air masses and

the precipitation measured at the PE station. Both methods, the regional analysis on the basis of the NAME dispersion model as well as the PSCF analysis show, that high N_{CN} values are directly linked to the advection of marine air masses, which were called marine events (MEs), having their origin in the region of the Southern Ocean. The occurrence of precipitation is also directly linked to the occurrence of MEs, as marine air masses are the only significant source of water vapor in Antarctica. Strong precipitation events caused the lowest N_{CN} and N_{CCN} values presented in this study, due to particle scavenging and wet deposition. Therefore, MEs showed the lowest but also the highest particle concentrations measured. In contrast, when air masses had spent more than 90 % of the 10 days prior to arrival over the Antarctic continent, which are times that were called continental events (CEs), measured N_{CN} and N_{CCN} values were comparably constant, and these were assumed to be continental background concentrations during austral summer. The Antarctic continent itself was found to not act as a significant source of aerosol particles and CCN measured at the PE station during these times. MEs and CEs occur 39 % and 61 % of the time, respectively.

The hygroscopicity of the CCNs could only be determined for measurements at $SS=0.1\%$, as the $PNSDs$ could only be measured in a size range between 90 nm and $6.8\ \mu m$. The median d_{crit} and κ of the entire measurement period were determined to be 110 nm and 1, respectively. This high hygroscopicity, which is valid for the comparably small fraction of particles observed in the respective size range, can be attributed to the presence of mainly sea salt and likely, but to a minor fraction, sulfate aerosol particles. The presence of sea salt also is in agreement with the results of the PSCF analysis, which shows that air masses having their origin at Antarctic ice shelf areas cause elevated values for particles with sizes above ≈ 110 nm. These particles could have been released and formed from snow particles from surface snow layers, e.g., during periods of high wind speed when fresh snow is available and winds are high enough to cause drifting or blowing snow (Gossart et al., 2017) or else may originate from sea spray directly. Enhanced κ values are also reported by O'Shea et al. (2017). They inferred a median κ of 1.13 during two days when back trajectories indicate that air masses had passed over sea ice regions of the Weddell Sea. As the majority of the aerosol particles with respect to number are found to be smaller than 110 nm and are known to be formed indirectly during NPF and growth processes, it can be assumed that the measurements at higher SS would yield to a lower aerosol particle hygroscopicity. O'Shea et al. (2017) for instance report a median κ value of 0.66 during measurements in December for five different SS (0.08, 0.2, 0.32, 0.41, 0.53 %). However, the mean κ value of 0.15 at 0.4 % SS reported by Kim et al. (2017) is remarkably low and is hardly compatible with the results presented in this thesis or the generally high hygroscopicity reported in other studies, e.g., O'Shea et al. (2017); Pringle et al. (2010); Asmi et al. (2010). Following from these results, the Antarctic aerosol particle hygroscopicity appears to cover a wide range that likely depends on the measurement

location (the above mentioned κ values were measured at different locations). For a more precise characterization of the Antarctic aerosol particle hygroscopicity additional investigations are suggested.

This study and the collected data set contributes to a better understanding of aerosol particles and CCN in particular in the undersampled region of East Antarctica. Currently it might be the most comprehensive set of CCN data in the region of East Antarctica and beside of the data presented by Kim et al. (2017) it is the only Antarctic CCN data set that was recorded during several years. Nonetheless, in contrast to Kim et al. (2017) it is limited on the austral summer seasons, since the PE station is under remote control during the austral winter time. A further limitation of the data set is the *PNSD* measurement starting just from 90 nm. Therefore the hygroscopicity of Aitken mode aerosol particles and NPF events as well as growth rates could not be examined, but would be extremely valuable for a better characterization of the East Antarctic aerosol particle properties. Beside this, the collection of chemical information of aerosol particles would be a further valuable addition to similar measurements as presented in this thesis. A first attempt to collect aerosol particles on filters using a simple set up consisting of a pump and a filter holder were done in the austral summer of 2017/18 at the PE station. Such filter samples can be used to determine the chemical composition and also to investigate ice nucleating particles (INP). Further, there are plans to use the infrastructure at the German Neumayer station, including a SMPS system which measures the Antarctic *PNSD* also in the size range below 100 nm. Measurements of the full yearly cycle would be possible at this location.

A. Appendix

A.1. *SS* calibration of the CCNC

Prior to each of the measurement campaigns a *SS* calibration of the CCNC was done at the cloud laboratory of the Leibniz Institute for Tropospheric Research (TROPOS) following a standard procedure (Gysel and Stratmann, 2013) with some modifications to account for the lower pressure (approximately 820 hPa) at the PE station in Antarctica. These calibrations were performed with the set up that is schematically shown in Figure A.1.

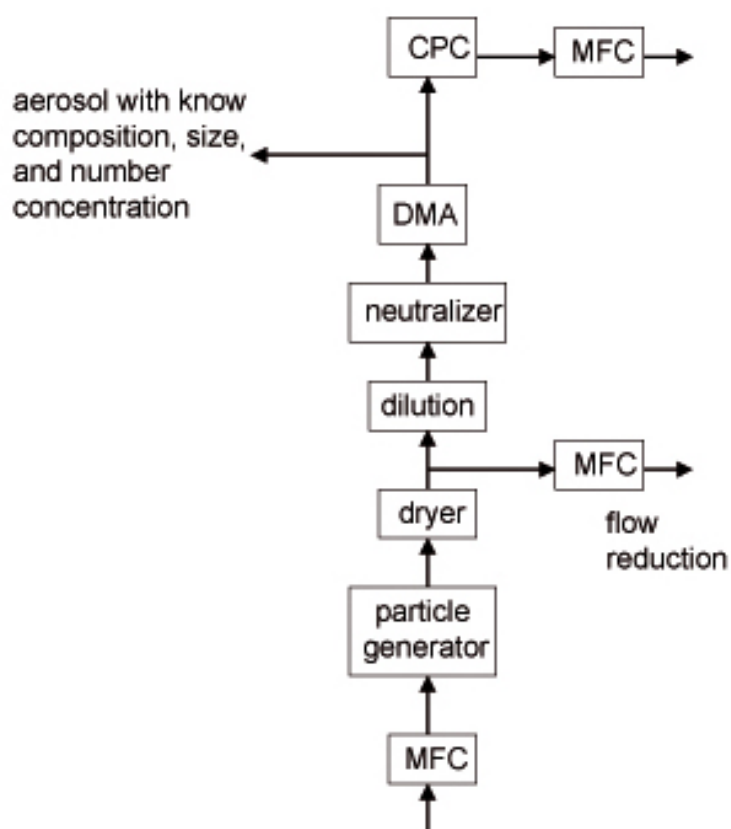


Figure A.1.: Schematic of the aerosol particle production

Synthetic ammonium sulfate aerosol particles are produced using a wet solution of approximately 0.1 g of ammonium sulfate per 0.5l of Milli-Q water. An atomizer creates ammonium sulfate solution droplets. The solution droplets are dried to get a polydisperse aerosol population of pure ammonium sulfate aerosol particles. A dilution section is used

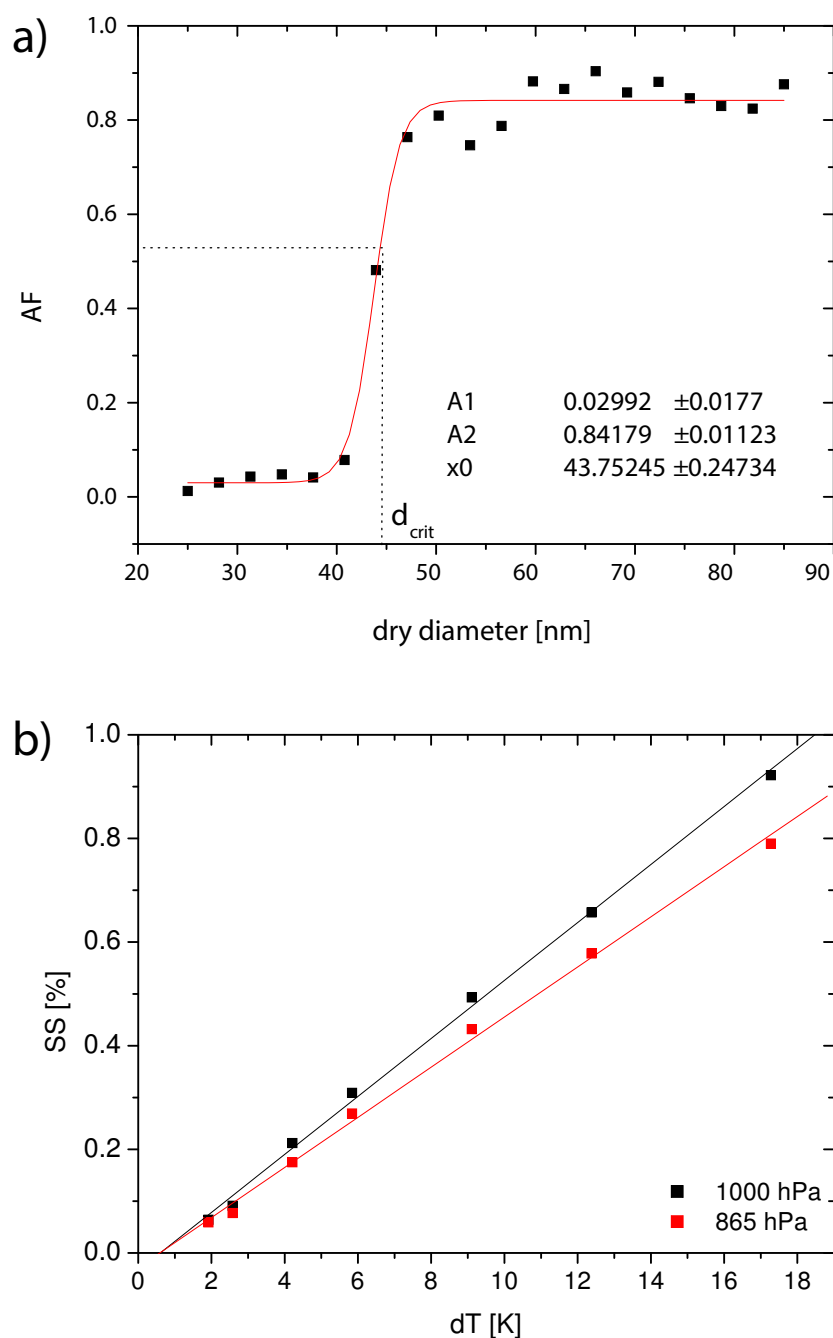


Figure A.2.: **SS calibration of a CCNC**

a) AF (black dots) vs. the dry particle diameter together with a Boltzmann fit function (red curve). Such a scan is used to determine d_{crit} of ammonium sulfate particles, that is used for the SS calibration of a CCNC. d_{crit} is the diameter at which 50% of the aerosol particles activate to cloud droplets. This particular scan was done with a temperature difference inside the CCNC column of 8.91 K.

b) Result of a SS calibration showing the effective SS over dT for the 6 standard SS values of 0.07, 0.1, 0.2, 0.3, 0.5, 0.7 and 1% together with a linear fit for standard pressure (black) and under pressure (red). The linear fit gives the final calibration function for the CCNC.

to adjust the aerosol particle number concentration, so that the CCNC gets a) at least 100 cm^{-3} of ammonium sulfate particles to ensure a good counting statistic and b) less than 2000 cm^{-3} (Gysel and Stratmann, 2013) to avoid competition for water vapor between the separate aerosol particles (there is not enough water vapor available to activate more than 2000 cm^{-3} particles to cloud droplets reliably). In the next step the size selection is done by means of a Differential Mobility Particle Sizer (DMPS). The individual components of the DMPS, are a neutralizer, a DMA and a CPC. The working principal is comparable to the SMPS system, that was explained in Subsection 2.1.2. However, the DMPS steps through the particle diameter range of interest, staying at a single step with a constant aerosol particle diameter as long as necessary for counting particle number concentrations, which typically is on the order of some seconds. This results in a good counting statistic, which is an advantage of the DMPS if it is applied for a CCNC calibration. Stepping through the whole size range takes longer than in case of using a SMPS, which however is not a disadvantage in case of a calibration in the laboratory.

Behind the DMA the aerosol flow is split in two parts, so that the CPC and a CCNC get the same number concentration of the monodisperse aerosol particles as input. In case of a CCNC calibration prior to using the instrument in Antarctica, it is set to a pressure of $\approx 830 \text{ hPa}$ using vacuum and needle valves at the inlet and the outlet of the CCNC. The ratio of N_{CCN} to N_{CN} gives the activated fraction (AF). The CCNC calibrations are done at a SS of 0.07, 0.1, 0.2, 0.3, 0.5, 0.7 and 1 % (to be absolutely correct the temperature difference between the bottom and top of the CCNC column is adjusted so that, based on the former SS calibration, these SS values are reached). For each SS the aerosol particle size is scanned, so that the AF ranges from zero to one. Figure A.2a depicts an AF curve (black dots) measured at a temperature difference of 8.91 K and a Boltzmann fit (red curve). The Boltzmann fit function is used to determine d_{crit} , which is the argument, i.e. the dry particle diameter, at $(A2 - A1)/2$, where 50 % of the available ammonium sulfate particles activate to cloud droplets. The Boltzmann fit function only works well if the plateaus at $A1$ and $A2$ are large enough, which means, that a sufficiently large diameter range has to be scanned during the calibration. Using d_{crit} and applying the Köhler theory the real (also called effective) SS inside the CCNC column can be determined for the adjusted temperature difference dT . This procedure is done for all SS , which results in the black and red data points of Figure A.2b. A linear fit gives the final SS calibration function for the CCNC.

A.2. Error Analysis with Monte Carlo Simulation

Measurements of $PNSD$ and N_{CCN} come along with device specific uncertainties. For instance the particle diameter that is selected with a DMA can be assumed to have an uncertainty of 3 % and the measured particle number concentration an uncertainty of 5 %

corresponding to 1 standard deviation, respectively (Gysel and Stratmann, 2013). Moreover, the effective SS in the CCN counter has a relative uncertainty of 3.5 % for SS above 0.2 % corresponding to 1 standard deviation. These uncertainties have been inferred from several SS calibrations that were performed at the Leibniz Institute for Tropospheric Research (TROPOS). Below $SS = 0.2\%$ the same absolute uncertainty as for $SS = 0.2\%$ can be assumed (Gysel and Stratmann, 2013). To consider the impact of these uncertainties on d_{crit} and κ in a realistic way, a Monte Carlo simulation (MCS) based on random normal distributions was used. This following general equation was applied:

$$s_{MC} = s + (s * u * p), \quad (\text{A.1})$$

where u is the relative uncertainty, p a random number, s is the measured signal and s_{MC} the resulting MCS signal. This was done for 10000 random and normally distributed numbers p , with a mean of 0 and a standard deviation of 1, which then results in 10000 values for s_{MC} with a variability that is characterized by u .

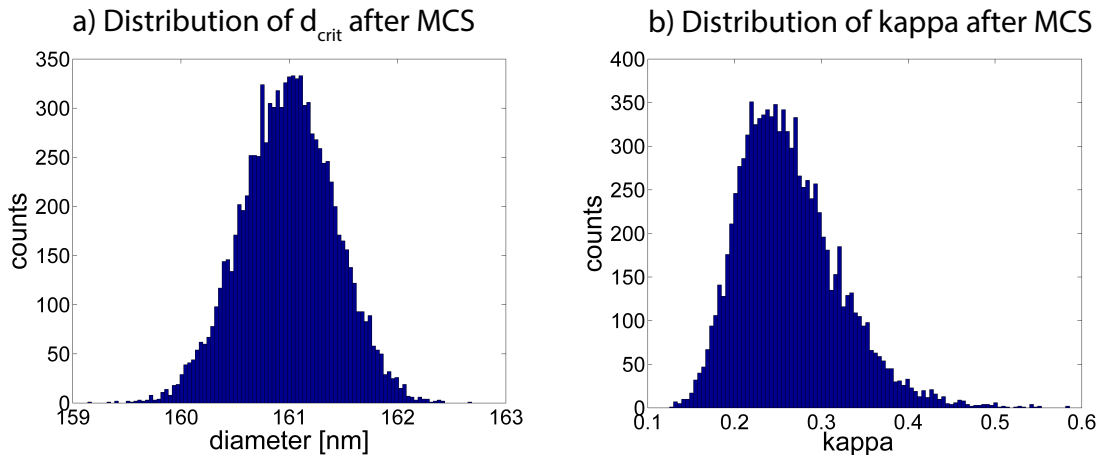


Figure A.3.: **Monte Carlo simulation**

- a) Distribution of 10000 d_{crit} values after applying the MCS. The mean and the standard deviation of this distribution are the final d_{crit} and its uncertainty due to the 5 % uncertainty in the particle number concentration of each size bin in the $PNSD$, respectively.
- b) Distribution of 10000 κ values after applying the MCS. As this results in a log-normal distribution of κ values it is appropriate to use the median and percentiles as the final κ value and its uncertainty, respectively.

In a first step, the uncertainty in d_{crit} was obtained by a MCS based on one exemplary $PNSD$, the related N_{CCN} and a 5 % uncertainty in the particle number concentration. Equation A.1 was used to vary the particle number concentration of each size bin of the $PNSD$ to calculate 10000 d_{crit} values, of which a distribution is shown in Figure A.3a. The mean and standard deviation of these 10000 d_{crit} values can be taken from this distribution, and the overall uncertainty in d_{crit} was derived from those values together with the 3 % uncertainty in the particle sizing due to the DMA, using error propagation. This was then done for all $PNSDs$. The resulting uncertainties are shown as error bars in the middle panel of

Figure 3.9.

κ and the corresponding error bars in the lower panel of Figure 3.9 are inferred by means of Eq. 2.6 where d_{crit} and S_{crit} , which is the effective SS of the CCN counter, are 10000 times Monte Carlo simulated (same procedure as for d_{crit}). Since the connection between κ and SS is logarithmic the resulting distribution of the 10000 κ values is a log-normal distribution, as can be seen in Figure A.3b exemplarily for one case. Consequently, our final inferred κ and its uncertainty are the median and the 5 and 95 % percentiles of this distribution, respectively. The average of all widths between the 5 and 95 % percentiles is the value we compared with the width between the 5 and 95 % percentiles of all median κ values to make a statement about the significance of our results.

List of Figures

2.1. Aerosol particle modes	10
2.2. Schematic of the TSI SMPS model 3936	12
2.3. Schematic of the TSI LAS-X model 3340	14
2.4. Working principle of the DMT CCNC-100	15
2.5. Köhler curve of an ammonium sulphate particle	17
2.6. Determination of d_{crit}	19
2.7. NAME footprint	20
2.8. NAME regional analysis	21
3.1. RACEPAC - overview map	26
3.2. RACEPAC - time series of meteorological parameters	27
3.3. RACEPAC - measuring set up	28
3.4. RACEPAC - time series of particle number concentrations	30
3.5. RACEPAC - clean and polluted <i>PNSD</i>	31
3.6. RACEPAC - backtrajectories of the three periods	33
3.7. RACEPAC - PSCF analysis	35
3.8. RACEPAC - <i>PNSDs</i> of the three periods	36
3.9. RACEPAC - CCN and hygroscopicity	40
3.10. RACEPAC - κ PDF	41
3.11. RACEPAC - comparison of ground based and airborne <i>PNSDs</i>	42
3.12. Antarctica - overview about the Princess Elisabeth Antarctica research station	46
3.13. Antarctica - time series of basic weather parameters	47
3.14. Antarctica - annual cycle of N_{CN}	51
3.15. Antarctica - time series of measured properties 2013/14	53
3.16. Antarctica - time series of measured properties 2014/15	54
3.17. Antarctica - time series of measured properties 2015/16	55
3.18. Antarctica - Connection between N_{CN} and the occurrence of continental air masses	57
3.19. Antarctica - example of new particle formation	58
3.20. Antarctica - PSCF results	60
3.21. Antarctica - κ results	63

List of Figures

A.1. Schematic of the aerosol particle production	71
A.2. AF of a size scan	72
A.3. Monte Carlo simulation	74

List of Tables

2.1. Instruments	9
3.1. RACEPAC - CCN and hygroscopicity	39
3.2. Antarctica - basic weather parameters	48
3.3. Antarctica - summary of measured properties	48

Bibliography

- Albrecht, B. (1989). Aerosols, cloud microphysics, and fractional cloudiness. *Science*, 245(4923):1227–1230.
- AMAP (2006). *AMAP Assessment 2006: Acidifying Pollutants, Arctic Haze, and Acidification in the Arctic*. Arctic Monitoring and Assessment Programme (AMAP).
- Andreae, M. O. and Rosenfeld, D. (2008). Aerosol-cloud-precipitation interactions. Part 1. The nature and sources of cloud-active aerosols. *Earth-Sci. Rev.*, 89(1):13 – 41.
- Ashbaugh, L. L., Malm, W. C., and Sadeh, W. Z. (1985). A residence time probability analysis of sulfur concentrations at grand Canyon National Park. *Atmos. Environ.*, 19(8):1263 – 1270.
- Asmi, E., Frey, A., Virkkula, A., Ehn, M., Manninen, H., Timonen, H., Tolonen-Kivimäki, O., Aurela, M., Hillamo, R., and Kulmala, M. (2010). Hygroscopicity and chemical composition of Antarctic sub-micrometre aerosol particles and observations of new particle formation. *Atmos. Chem. Phys.*, 10(9):4253–4271.
- Asmi, E., Kondratyev, V., Brus, D., Laurila, T., Lihavainen, H., Backman, J., Vakkari, V., Aurela, M., Hatakka, J., Viisanen, Y., Uttal, T., Ivakhov, V., and Makshtas, A. (2016). Aerosol size distribution seasonal characteristics measured in Tiksi, Russian Arctic. *Atmos. Chem. Phys.*, 16(3):1271–1287.
- Behrenfeld, U., Krejci, R., Ström, J., and Stohl, A. (2008). Chemical properties of Arctic aerosol particles collected at the Zeppelin station during the aerosol transition period in May and June of 2004. *Tellus B*, 60(3):405–415.
- Browse, J., Carslaw, K. S., Arnold, S. R., Pringle, K., and Boucher, O. (2012). The scavenging processes controlling the seasonal cycle in Arctic sulphate and black carbon aerosol. *Atmos. Chem. Phys.*, 12(15):6775–6798.
- Burkart, J., Hodshire, A. L., Mungall, E. L., Pierce, J. R., Collins, D. B., Ladino, L. A., Lee, A. K. Y., Irish, V., Wentzell, J. J. B., Liggió, J., Papakyriakou, T., Murphy, J., and Abbatt, J. (2017a). Organic condensation and particle growth to CCN sizes in the summertime marine Arctic is driven by materials more semivolatile than at continental sites. *Geophys. Res. Lett.*, 44.

- Burkart, J., Willis, M. D., Bozem, H., Thomas, J. L., Law, K., Hoor, P., Aliabadi, A. A., Kollner, F., Schneiders, J., Herber, A., Abbatt, J. P. D., and Leaitch, W. R. (2017b). Summertime observations of elevated levels of ultrafine particles in the high Arctic marine boundary layer. *Atmos. Chem. Phys.*, 17(8):5515–5535.
- Carslaw, K., Lee, L., Reddington, C., Pringle, K., Rap, A., Forster, P., Mann, G., Spracklen, D., Woodhouse, M., Regayre, L., et al. (2013). Large contribution of natural aerosols to uncertainty in indirect forcing. *Nature*, 503(7474):67–71.
- Cavalieri, D. and Parkinson, C. (2008). Antarctic sea ice variability and trends, 1979–2006. *J. Geophys. Res.: Oceans*, 113(C7).
- Collins, D. B., Burkart, J., Chang, R. Y. W., Lizotte, M., Boivin-Rioux, A., Blais, M., Mungall, E. L., Boyer, M., Irish, V. E., Masse, G., Kunkel, D., Tremblay, J. E., Papyriakou, T., Bertram, A. K., Bozem, H., Gosselin, M., Lévasseur, M., and Abbatt, J. P. D. (2017). Frequent ultrafine particle formation and growth in Canadian Arctic marine and coastal environments. *Atmos. Chem. Phys.*, 17(21):13119–13138.
- Croft, B., Martin, R. V., Leaitch, W. R., Tunved, P., Breider, T. J., D’Andrea, S. D., and Pierce, J. R. (2016a). Processes controlling the annual cycle of Arctic aerosol number and size distributions. *Atmos. Chem. Phys.*, 16(6):3665–3682.
- Croft, B., Wentworth, G. R., Martin, R. V., Leaitch, W. R., Murphy, J. G., Murphy, B. N., Kodros, J. K., Abbatt, J. P. D., and Pierce, J. R. (2016b). Contribution of Arctic seabird-colony ammonia to atmospheric particles and cloud-albedo radiative effect. *Nat. Commun.*, 7.
- Dall’Osto, M., Beddows, D. C. S., Tunved, P., Krejci, R., Ström, J., Hansson, H.-C., Yoon, Y. J., Park, K.-T., Becagli, S., Udusti, R., Onasch, T., O’Dowd, C. D., Simó, R., and Harrison, R. M. (2017a). Arctic sea ice melt leads to atmospheric new particle formation. *Sci. Rep.*, 7(1):3318.
- Dall’Osto, M., Ovadnevaite, J., Paglione, M., Beddows, D. C., Ceburnis, D., Cree, C., Cortés, P., Zamanillo, M., Nunes, S. O., Pérez, G. L., et al. (2017b). Antarctic sea ice region as a source of biogenic organic nitrogen in aerosols. *Sci. Rep.*, 7(1):6047.
- DeFelice, T. (1996). Variations in cloud condensation nuclei at palmer station Antarctica during February 1994. *Atmos. Res.*, 41(3-4):229–248.
- DeFelice, T., Saxena, V., and Yu, S. (1997). On the measurements of cloud condensation nuclei at Palmer Station, Antarctica. *Atmos. Environ.*, 31(23):4039–4044.
- DMT (2012). *Cloud Condensation Nuclei (CCN) Counter Manual for Single-Column CCNs DOC-0086 Revision I-2*. Droplet Measurement Technologies, Inc.

- Engvall, A.-C., Krejci, R., Ström, J., Treffeisen, R., Scheele, R., Hermansen, O., and Paatero, J. (2008). Changes in aerosol properties during spring-summer period in the Arctic troposphere. *Atmos. Chem. Phys.*, 8(3):445–462.
- Ervens, B., Sorooshian, A., Aldhaif, M., Shingler, T., Crosbie, E., Ziemba, L., Campuzano-Jost, P., Jimenez, J. L., and Wisthaler, A. (2018). Is there an aerosol signature of cloud processing? *Atmos. Chem. Phys. Discuss.*
- Fiebig, M., Hirdman, D., Lunder, C. R., Ogren, J. A., Solberg, S., Stohl, A., and Thompson, R. L. (2014). Annual cycle of Antarctic baseline aerosol: controlled by photooxidation-limited aerosol formation. *Atmos. Chem. Phys.*, 14(6):3083–3093.
- Freud, E., Krejci, R., Tunved, P., Leaitch, R., Nguyen, Q. T., Massling, A., Skov, H., and Barrie, L. (2017). Pan-Arctic aerosol number size distributions: seasonality and transport patterns. *Atmos. Chem. Phys.*, 17(13):8101–8128.
- Garrett, T. J., Radke, L. F., and Hobbs, P. V. (2002). Aerosol Effects on Cloud Emissivity and Surface Longwave Heating in the Arctic. *J. Atmos. Sci.*, 59(3):769–778.
- Gorodetskaya, I. V., Kneifel, S., Maahn, M., Van Tricht, K., Thiery, W., Schween, J. H., Mangold, A., Crewell, S., and Van Lipzig, N. P. M. (2015). Cloud and precipitation properties from ground-based remote-sensing instruments in East Antarctica. *Cryosphere*, 9(1):285–304.
- Gorodetskaya, I. V., Tsukernik, M., Claes, K., Ralph, M. F., Neff, W. D., and Van Lipzig, N. P. M. (2014). The role of atmospheric rivers in anomalous snow accumulation in East Antarctica. *Geophys. Res. Lett.*, 41(17):6199–6206.
- Gorodetskaya, I. V., Van Lipzig, N. P. M., Van den Broeke, M. R., Mangold, A., Boot, W., and Reijmer, C. H. (2013). Meteorological regimes and accumulation patterns at Utsteinen, Dronning Maud Land, East Antarctica: Analysis of two contrasting years. *J. Geophys. Res.: Atmos.*, 118(4):1700–1715.
- Gossart, A., Souverijns, N., Gorodetskaya, I. V., Lhermitte, S., Lenaerts, J. T. M., Schween, J. H., Mangold, A., Laffineur, Q., and van Lipzig, N. P. M. (2017). Blowing snow detection from ground-based ceilometers: application to East Antarctica. *Cryosphere*, 11(6):2755–2772.
- Greene, C. A., Gwyther, D. E., and Blankenship, D. D. (2017). Antarctic Mapping Tools for Matlab. *Comput. Geosci.*, 104(Supplement C):151 – 157.
- Gunsch, M. J., Kirpes, R. M., Kolesar, K. R., Barrett, T. E., China, S., Sheesley, R. J., Laskin, A., Wiedensohler, A., Tuch, T., and Pratt, K. A. (2017). Contributions of

- transported Prudhoe Bay oil field emissions to the aerosol population in Utqiagvik, Alaska. *Atmos. Chem. Phys.*, 17(17):10879–10892.
- Gysel, M. and Stratmann, F. (2013). WP3 - NA3: In-situ chemical, physical and optical properties of aerosols, Deliverable D3.11: Standardized protocol for CCN measurements. *Tech. rep.*
- Hamilton, D. S., Lee, L. A., Pringle, K. J., Reddington, C. L., Spracklen, D. V., and Carslaw, K. S. (2014). Occurrence of pristine aerosol environments on a polluted planet. *Proc. Natl. Acad. Sci.*, 111(52):18466–18471.
- Hara, K., Osada, K., Nishita-Hara, C., and Yamanouchi, T. (2011). Seasonal variations and vertical features of aerosol particles in the Antarctic troposphere. *Atmos. Chem. Phys.*, 11(11):5471–5484.
- Heintzenberg, J. (1980). Particle size distribution and optical properties of Arctic haze. *Tellus*, 32(3):251–260.
- Herenz, P., Wex, H., Henning, S., Kristensen, T. B., Rubach, F., Roth, A., Borrmann, S., Bozem, H., Schulz, H., and Stratmann, F. (2018). Measurements of aerosol and CCN properties in the Mackenzie River delta (Canadian Arctic) during spring–summer transition in May 2014. *Atmospheric Chemistry and Physics*, 18(7):4477–4496.
- Hopke, P. K. (2016). Review of receptor modeling methods for source apportionment. *J. Air Waste Manag. Assoc.*, 66(3):237–259. PMID: 26756961.
- Hoppel, W. A., Frick, G. M., Fitzgerald, J. W., and Larson, R. E. (1994). Marine boundary layer measurements of new particle formation and the effects nonprecipitating clouds have on aerosol size distribution. *J. Geophys. Res.: Atmos.*, 99(D7):14443–14459.
- Huang, J. and Jaeglé, L. (2017). Wintertime enhancements of sea salt aerosol in polar regions consistent with a sea ice source from blowing snow. *Atmos. Chem. Phys.*, 17(5):3699–3712.
- IPCC (2013). *Climate Change 2013: The Physical Science Basis. Contribution of Working Group I to the Fifth Assessment Report of the Intergovernmental Panel on Climate Change*. Cambridge University Press, Cambridge, United Kingdom and New York, NY, USA.
- Iversen, T. and Joranger, E. (1985). Arctic air pollution and large scale atmospheric flows. *Atmos. Environ.*, 19(12):2099 – 2108.
- Jacka, T. and Budd, W. (1998). Detection of temperature and sea-ice-extent changes in the Antarctic and Southern Ocean, 1949-96. *Ann. Glaciol.*, 27(1):553–559.

- Jacob, D. J., Crawford, J. H., Maring, H., Clarke, A. D., Dibb, J. E., Emmons, L. K., Ferrare, R. A., Hostetler, C. A., Russell, P. B., Singh, H. B., Thompson, A. M., Shaw, G. E., McCauley, E., Pederson, J. R., and Fisher, J. A. (2010). The Arctic Research of the Composition of the Troposphere from Aircraft and Satellites (ARCTAS) mission: design, execution, and first results. *Atmos. Chem. Phys.*, 10(11):5191–5212.
- Järvinen, E., Virkkula, A., Nieminen, T., Aalto, P. P., Asmi, E., Lanconelli, C., Busetto, M., Lupi, A., Schioppo, R., Vitale, V., Mazzola, M., Petäjä, T., Kerminen, V.-M., and Kulmala, M. (2013). Seasonal cycle and modal structure of particle number size distribution at Dome C, Antarctica. *Atmos. Chem. Phys.*, 13(15):7473–7487.
- Jones, A., Thomson, D., Hort, M., and Devenish, B. (2007). *The U.K. Met Office's Next-Generation Atmospheric Dispersion Model, NAME III*, pages 580–589. Springer US, Boston, MA.
- Kammermann, L., Gysel, M., Weingartner, E., Herich, H., Cziczo, D. J., Holst, T., Svenningsson, B., Arneth, A., and Baltensperger, U. (2010). Subarctic atmospheric aerosol composition: 3. Measured and modeled properties of cloud condensation nuclei. *J. Geophys. Res.: Atmos.*, 115(D4). D04202.
- Keegan, K. M., Albert, M. R., McConnell, J. R., and Baker, I. (2014). Climate change and forest fires synergistically drive widespread melt events of the Greenland Ice Sheet. *Proc. Natl. Acad. Sci.*, 111(22):7964–7967.
- Kim, J., Yoon, Y. J., Gim, Y., Kang, H. J., Choi, J. H., Park, K.-T., and Lee, B. Y. (2017). Seasonal variations in physical characteristics of aerosol particles at the King Sejong Station, Antarctic Peninsula. *Atmos. Chem. Phys.*, 17(21):12985–12999.
- Knutson, E. and Whitby, K. (1975). Aerosol classification by electric mobility: apparatus, theory, and applications. *J. Aerosol Sci.*, 6(6):443 – 451.
- Köhler, H. (1936). The nucleus in and the growth of hygroscopic droplets. *Trans. Faraday Soc.*, 32:1152–1161.
- Kolesar, K. R., Cellini, J., Peterson, P. K., Jefferson, A., Tuch, T., Birmili, W., Wiedensohler, A., and Pratt, K. A. (2017). Effect of Prudhoe Bay emissions on atmospheric aerosol growth events observed in Utqiagvik (Barrow), Alaska. *Atmos. Environ.*, 152:146–155.
- Koponen, I. K., Virkkula, A., Hillamo, R., Kerminen, V. M., and Kulmala, M. (2003). Number size distributions and concentrations of the continental summer aerosols in Queen Maud Land, Antarctica. *J. Geophys. Res.*, 108(D18).

- Kravchenko, V., Evtushevsky, O., Grytsai, A., and Milinevsky, G. (2011). Decadal variability of winter temperatures in the Antarctic Peninsula region. *Antarct. Sci.*, 23(6):614–622.
- Kristensen, T. B., Müller, T., Kandler, K., Benker, N., Hartmann, M., Prospero, J. M., Wiedensohler, A., and Stratmann, F. (2016). Properties of cloud condensation nuclei (CCN) in the trade wind marine boundary layer of the western North Atlantic. *Atmos. Chem. Phys.*, 16(4):2675–2688.
- Kyrö, E. M., Kerminen, V. M., Virkkula, A., Dal Maso, M., Parshintsev, J., Ruiz-Jimenez, J., Forsstrom, L., Manninen, H. E., Riekkola, M. L., Heinonen, P., and Kulmala, M. (2013). Antarctic new particle formation from continental biogenic precursors. *Atmos. Chem. Phys.*, 13(7):3527–3546.
- Lamb, D. and Verlinde, J. (2011). *Physics and chemistry of clouds*. Cambridge University Press.
- Latham, T. L., Beyersdorf, A. J., Thornhill, K. L., Winstead, E. L., Cubison, M. J., Hecobian, A., Jimenez, J. L., Weber, R. J., Anderson, B. E., and Nenes, A. (2013). Analysis of CCN activity of Arctic aerosol and Canadian biomass burning during summer 2008. *Atmos. Chem. Phys.*, 13(5):2735–2756.
- Law, K. S. and Stohl, A. (2007). Arctic Air Pollution: Origins and Impacts. *Science*, 315(5818):1537–1540.
- Leaitch, R. W., Sharma, S., Huang, L., Toom-Saunty, D., Chivulescu, A., Macdonald, A. M., von Salzen, K., Pierce, J. R., Bertram, A. K., Schroder, J. C., Shantz, N. C., Chang, R. Y.-W., and Norman, A.-L. (2013). Dimethyl sulfide control of the clean summertime Arctic aerosol and cloud. *Elem. Sci. Anthr.*, 1(1).
- Leaitch, W. R., Korolev, A., Aliabadi, A. A., Burkart, J., Willis, M. D., Abbatt, J. P. D., Bozem, H., Hoor, P., Kollnr, F., Schneider, J., Herber, A., Konrad, C., and Brauner, R. (2016). Effects of 20-100nm particles on liquid clouds in the clean summertime Arctic. *Atmos. Chem. Phys.*, 16(17):11107–11124.
- Legrand, M., Ducroz, F., Wagenbach, D., Mulvaney, R., and Hall, J. (1998). Ammonium in coastal Antarctic aerosol and snow: Role of polar ocean and penguin emissions. *J. Geophys. Res.: Atmos.*, 103(D9):11043–11056.
- Li, S.-M., Barrie, L. A., and Sirois, A. (1993). Biogenic sulfur aerosol in the Arctic troposphere: 2. Trends and seasonal variations. *J. Geophys. Res.: Atmos.*, 98(D11):20623–20631.

- Liss, P. S. and Lovelock, J. E. (2008). Climate change: the effect of DMS emissions. *Environ. Chem.*, 4(6):377–378.
- Lubin, D. and Vogelmann, A. M. (2006). A climatologically significant aerosol longwave indirect effect in the Arctic. *Nature*, 439(7075):453–456.
- Martin-Español, A., Bamber, J. L., and Zammit-Mangion, A. (2017). Constraining the mass balance of East Antarctica. *Geophys. Res. Lett.*, 44(9):4168–4175. 2017GL072937.
- Mauritsen, T., Sedlar, J., Tjernström, M., Leck, C., Martin, M., Shupe, M., Sjogren, S., Sierau, B., Persson, P. O. G., Brooks, I. M., and Swietlicki, E. (2011). An Arctic CCN-limited cloud-aerosol regime. *Atmos. Chem. Phys.*, 11(1):165–173.
- Modini, R. L., Frossard, A. A., Ahlm, L., Russell, L. M., Corrigan, C. E., Roberts, G. C., Hawkins, L. N., Schroder, J. C., Bertram, A. K., Zhao, R., Lee, A. K. Y., Abbatt, J. P. D., Lin, J., Nenes, A., Wang, Z., Wonaschütz, A., Sorooshian, A., Noone, K. J., Jonsson, H., Seinfeld, J. H., Toom-Saunty, D., Macdonald, A. M., and Leaitch, W. R. (2015). Primary marine aerosol-cloud interactions off the coast of California. *J. Geophys. Res.: Atmos.*, 120(9):4282–4303. 2014JD022963.
- Moore, R. H., Bahreini, R., Brock, C. A., Froyd, K. D., Cozic, J., Holloway, J. S., Middlebrook, A. M., Murphy, D. M., and Nenes, A. (2011). Hygroscopicity and composition of Alaskan Arctic CCN during April 2008. *Atmos. Chem. Phys.*, 11(22):11807–11825.
- Nguyen, Q. T., Glasius, M., Sorensen, L. L., Jensen, B., Skov, H., Birmili, W., Wiedensohler, A., Kristensson, A., Nojgaard, J. K., and Massling, A. (2016). Seasonal variation of atmospheric particle number concentrations, new particle formation and atmospheric oxidation capacity at the high Arctic site Villum Research Station, Station Nord. *Atmos. Chem. Phys.*, 16(17):11319–11336.
- O’Shea, S. J., Choularton, T. W., Flynn, M., Bower, K. N., Gallagher, M., Crosier, J., Williams, P., Crawford, I., Fleming, Z. L., Listowski, C., Kirchgaessner, A., Ladkin, R. S., and Lachlan-Cope, T. (2017). In situ measurements of cloud microphysics and aerosol over coastal Antarctica during the MAC campaign. *Atmos. Chem. Phys.*, 17(21):13049–13070.
- Parkinson, C. and Cavalieri, D. (2012). Antarctic sea ice variability and trends, 1979–2010. *Cryosphere*, 6(4):871.
- Petters, M. D. and Kreidenweis, S. M. (2007). A single parameter representation of hygroscopic growth and cloud condensation nucleus activity. *Atmos. Chem. Phys.*, 7(8):1961–1971.

- Pringle, K. J., Tost, H., Pozzer, A., Pöschl, U., and Lelieveld, J. (2010). Global distribution of the effective aerosol hygroscopicity parameter for CCN activation. *Atmos. Chem. Phys.*, 10(12):5241–5255.
- Pruppacher, H. R. and Klett, J. D. (1997). *Microphysics of Clouds and Precipitation*. Kluwer Academic Publishers.
- Quinn, P. K., Coffman, D. J., Johnson, J. E., Upchurch, L. M., and Bates, T. S. (2017). Small fraction of marine cloud condensation nuclei made up of sea spray aerosol. *Nat. Geosci.*, 10(9):674.
- Quinn, P. K., Miller, T. L., Bates, T. S., Ogren, J. A., Andrews, E., and Shaw, G. E. (2002). A 3-year record of simultaneously measured aerosol chemical and optical properties at Barrow, Alaska. *J. Geophys. Res.: Atmos.*, 107(D11):AAC 8–1–AAC 8–15.
- Quinn, P. K., Shaw, G., Andrews, E., Dutton, E. G., Ruoho-Airola, T., and Gong, S. L. (2007). Arctic haze: current trends and knowledge gaps. *Tellus B*, 59B:99 – 114.
- Roberts, G. C. and Nenes, A. (2005). A continuous-flow streamwise thermal-gradient CCN chamber for atmospheric measurements. *Aerosol Sci. Technol.*, 39(3):206–221.
- Schaffer, J., Timmermann, R., Arndt, J. E., Kristensen, S. S., Mayer, C., Morlighem, M., and Steinhage, D. (2016). A global, high-resolution data set of ice sheet topography, cavity geometry, and ocean bathymetry. *Earth Syst. Sci. Data*, 8(2):543.
- Schmale, J., Schneider, J., Nemitz, E., Tang, Y. S., Dragosits, U., Blackall, T. D., Trathan, P. N., Phillips, G. J., Sutton, M., and Braban, C. F. (2013). Sub-Antarctic marine aerosol: dominant contributions from biogenic sources. *Atmos. Chem. Phys.*, 13(17):8669–8694.
- Seinfeld, J. and Pandis, S. (1998). *Atmospheric Chemistry and Physics: From Air Pollution to Climate Change*. Wiley-Interscience.
- Sharma, S., Chan, E., Ishizawa, M., Toom-Sauntry, D., Gong, S. L., Li, S. M., Tarasick, D. W., Leaitch, W. R., Norman, A., Quinn, P. K., Bates, T. S., Lelieveld, M., Barrie, L. A., and Maenhaut, W. (2012). Influence of transport and ocean ice extent on biogenic aerosol sulfur in the Arctic atmosphere. *J. Geophys. Res. Atmos.*, 117.
- Shaw, G. (1981). Eddy diffusion transport of Arctic pollution from the mid-latitudes: A preliminary model. *Atmos. Environ.*, 15(8):1483 – 1490.
- Shaw, G. E. (1995). The Arctic Haze Phenomenon. *Bull. Am. Meteorol. Soc.*, 76(12):2403–2413.

- Shepherd, A., Ivins, E., Rignot, E., Smith, B., van den Broeke, M., Velicogna, I., Whitehouse, P., Briggs, K., Joughin, I., Krinner, G., Nowicki, S., Payne, T., Scambos, T., Schlegel, N., Geruo, A., Agosta, C., Ahlstrom, A., Babonis, G., Barletta, V., Blazquez, A., Bonin, J., Csatho, B., Cullather, R., Felikson, D., Fettweis, X., Forsberg, R., Gallee, H., Gardner, A., Gilbert, L., Groh, A., Gunter, B., Hanna, E., Harig, C., Helm, V., Horvath, A., Horwath, M., Khan, S., Kjeldsen, K. K., Konrad, H., Langen, P., Lecavalier, B., Loomis, B., Luthcke, S., McMillan, M., Melini, D., Mernild, S., Mohajerani, Y., Moore, P., Mouginit, J., Moyano, G., Muir, A., Nagler, T., Nield, G., Nilsson, J., Noel, B., Ootosaka, I., Pattle, M. E., Peltier, W. R., Pie, N., Rietbroek, R., Rott, H., Sandberg-Sorensen, L., Sasgen, I., Save, H., Scheuchl, B., Schrama, E., Schroder, L., Seo, K. W., Simonsen, S., Slater, T., Spada, G., Sutterley, T., Talpe, M., Tarasov, L., van de Berg, W. J., van der Wal, W., van Wessem, M., Vishwakarma, B. D., Wiese, D., Wouters, B., and Team, I. (2018). Mass balance of the Antarctic Ice Sheet from 1992 to 2017. *Nature*, 558(7709):219–222.
- Shepherd, A., Ivins, E. R., Geruo, A., Barletta, V. R., Bentley, M. J., Bettadpur, S., Briggs, K. H., Bromwich, D. H., Forsberg, R., Galin, N., et al. (2012). A reconciled estimate of ice-sheet mass balance. *Science*, 338(6111):1183–1189.
- Silvergren, S., Wideqvist, U., Ström, J., Sjogren, S., and Svenningsson, B. (2014). Hygroscopic growth and cloud forming potential of Arctic aerosol based on observed chemical and physical characteristics (a 1 year study 2007-2008). *J. Geophys. Res.: Atmos.*, 119(24):14,080–14,097. 2014JD021657.
- Souverein, N., Gossart, A., Gorodetskaya, I. V., Lhermitte, S., Mangold, A., Laffineur, Q., Delcloo, A., and van Lipzig, N. P. M. (2018). How does the ice sheet surface mass balance relate to snowfall? Insights from a ground-based precipitation radar in East Antarctica. *The Cryosphere*.
- Sprenger, M. and Wernli, H. (2015). The LAGRANTO Lagrangian analysis tool - version 2.0. *Geosci. Model Dev.*, 8(8):2569–2586.
- Stein, A. F., Draxler, R. R., Rolph, G. D., Stunder, B. J. B., Cohen, M. D., and Ngan, F. (2015). NOAA's HYSPLIT Atmospheric Transport and Dispersion Modeling System. *Bull. Am. Meteorol. Soc.*, 96(12):2059–2077.
- Stohl, A. (2006). Characteristics of atmospheric transport into the Arctic troposphere. *J. Geophys. Res.: Atmos.*, 111(D11). D11306.
- Stone, R. S., Sharma, S., Herber, A., Eleftheriadis, K., and Nelson, D. W. (2014). A characterization of Arctic aerosols on the basis of aerosol optical depth and black carbon measurements. *ELEMENTA - Science of the Anthropocene*.

- Ström, J., Engvall, A.-C., Delbart, F., Krejci, R., and Treffeisen, R. (2009). On small particles in the Arctic summer boundary layer: observations at two different heights near Ny-Ålesund, Svalbard. *Tellus B*, 61(2):473–482.
- Swietlicki, E., Hansson, H.-C., Hämeri, K., Svenningsson, B., Massling, A., McFiggans, G., McMurry, P., Petäjä, T., Tunved, P., Gysel, M., et al. (2008). Hygroscopic properties of submicrometer atmospheric aerosol particles measured with H-TDMA instruments in various environments - A review. *Tellus B*, 60(3):432–469.
- Teinila, K., Kerminen, V. M., and Hillamo, R. (2000). A study of size-segregated aerosol chemistry in the Antarctic atmosphere. *J. Geophys. Res. Atmos.*, 105(D3):3893–3904.
- Tietze, K., Riedi, J., Stohl, A., and Garrett, T. J. (2011). Space-based evaluation of interactions between aerosols and low-level Arctic clouds during the Spring and Summer of 2008. *Atmos. Chem. Phys.*, 11(7):3359–3373.
- TSI (2001). *Model 3936 Scanning Mobility Particle Sizer (SMPS) - Instruction Manual*. TSI Inc.
- TSI (2015). *Laser Aerosol Spectrometer Model 3340 - Operation and Service Manual*. TSI Inc.
- Tunved, P., Ström, J., and Krejci, R. (2013). Arctic aerosol life cycle: linking aerosol size distributions observed between 2000 and 2010 with air mass transport and precipitation at Zeppelin station, Ny-Ålesund, Svalbard. *Atmos. Chem. Phys.*, 13(7):3643–3660.
- Twomey, S. (1974). Pollution and the planetary albedo. *Atmos. Environ.*, 8:1251–1256.
- Vallina, S. M., Simó, R., and Gassó, S. (2006). What controls CCN seasonality in the Southern Ocean? A statistical analysis based on satellite-derived chlorophyll and CCN and model-estimated OH radical and rainfall. *Global. Biogeochem. Cycles*, 20(1). GB1014.
- Vaughan, D. G., Marshall, G. J., Connolley, W. M., Parkinson, C., Mulvaney, R., Hodgson, D. A., King, J. C., Pudsey, C. J., and Turner, J. (2003). Recent Rapid Regional Climate Warming on the Antarctic Peninsula. *Clim. Change*, 60(3):243–274.
- Velicogna, I. and Wahr, J. (2006). Measurements of time-variable gravity show mass loss in Antarctica. *Science*, 311(5768):1754–1756.
- Virkkula, A., Asmi, E., Teinilä, K., Frey, A., Aurela, M., Timonen, H., Mäkelä, T., Samuli, A., Hillamo, R., Aalto, P. P., et al. (2009). Review of aerosol research at the Finnish antarctic research station Aboa and its surroundings in Queen Maud Land, Antarctica. *Geophysica*, 45(1-2):163–181.

- Wagenbach, D., Ducroz, F., Mulvaney, R., Keck, L., Minikin, A., Legrand, M., Hall, J., and Wolff, E. (1998). Sea-salt aerosol in coastal Antarctic regions. *J. Geophys. Res.: Atmos.*, 103(D9):10961–10974.
- Wagenbach, D., Görlach, U., Moser, K., and Münnich, K. O. (1988). Coastal Antarctic aerosol: The seasonal pattern of its chemical composition and radionuclide content. *Tellus B*, 40(5):426–436.
- Waked, A., Favez, O., Alleman, L. Y., Piot, C., Petit, J.-E., Delaunay, T., Verlinden, E., Golly, B., Besombes, J.-L., Jaffrezo, J.-L., and Leoz-Garziandia, E. (2014). Source apportionment of PM₁₀ in a north-western Europe regional urban background site (Lens, France) using positive matrix factorization and including primary biogenic emissions. *Atmos. Chem. Phys.*, 14(7):3325–3346.
- Warneke, C., Bahreini, R., Brioude, J., Brock, C. A., de Gouw, J. A., Fahey, D. W., Froyd, K. D., Holloway, J. S., Middlebrook, A., Miller, L., Montzka, S., Murphy, D. M., Peischl, J., Ryerson, T. B., Schwarz, J. P., Spackman, J. R., and Veres, P. (2009). Biomass burning in Siberia and Kazakhstan as an important source for haze over the Alaskan Arctic in April 2008. *Geophys. Res. Lett.*, 36.
- Wegner, A., Fischer, H., Delmonte, B., Petit, J.-R., Erhardt, T., Ruth, U., Svensson, A., Vinther, B., and Miller, H. (2015). The role of seasonality of mineral dust concentration and size on glacial/interglacial dust changes in the EPICA Dronning Maud Land ice core. *J. Geophys. Res.: Atmos.*, 120(19):9916–9931. 2015JD023608.
- Wegner, T., Hussein, T., Hämeri, K., Vesala, T., Kulmala, M., and Weber, S. (2012). Properties of aerosol signature size distributions in the urban environment as derived by cluster analysis. *Atmos. Environ.*, 61:350 – 360.
- Weller, R., Minikin, A., Wagenbach, D., and Dreiling, V. (2011). Characterization of the inter-annual, seasonal, and diurnal variations of condensation particle concentrations at Neumayer, Antarctica. *Atmos. Chem. Phys.*, 11(24):13243–13257.
- Weller, R., Schmidt, K., Teinilä, K., and Hillamo, R. (2015). Natural new particle formation at the coastal Antarctic site Neumayer. *Atmos. Chem. Phys.*, 15(19):11399–11410.
- Wentworth, G. R., Murphy, J. G., Croft, B., Martin, R. V., Pierce, J. R., Cote, J. S., Courchesne, I., Tremblay, J. E., Gagnon, J., Thomas, J. L., Sharma, S., Toom-Saunty, D., Chivulescu, A., Lévassieur, M., and Abbatt, J. P. D. (2016). Ammonia in the summertime Arctic marine boundary layer: sources, sinks, and implications. *Atmos. Chem. Phys.*, 16(4):1937–1953.

- Wex, H., McFiggans, G., Henning, S., and Stratmann, F. (2010). Influence of the external mixing state of atmospheric aerosol on derived CCN number concentrations. *Geophys. Res. Lett.*, 37(L10805):doi:10.1029/2010GL043337.
- Wiedensohler, A. (1988). An approximation of the bipolar charge distribution for particles in the submicron size range. *J. Aerosol Sci.*, 19(3):387 – 389.
- Wiedensohler, A., Covert, D., Swietlicki, E., Aalto, P., Heintzenberg, J., and Leck, C. (2011). Occurrence of an ultrafine particle mode less than 20 nm in diameter in the marine boundary layer during Arctic summer and autumn. *Tellus B*, 48(2).
- Willis, M. D., Burkart, J., Thomas, J. L., Kollner, F., Schneider, J., Bozem, H., Hoor, P. M., Aliabadi, A. A., Schulz, H., Herber, A. B., Leaitch, W. R., and Abbatt, J. P. D. (2016). Growth of nucleation mode particles in the summertime Arctic: a case study. *Atmos. Chem. Phys.*, 16(12):7663–7679.
- Yang, X., Pyle, J. A., and Cox, R. A. (2008). Sea salt aerosol production and bromine release: Role of snow on sea ice. *Geophys. Res. Lett.*, 35(16). L16815.
- Yli-Tuomi, T., Hopke, P. K., Paatero, P., Basunia, M., Landsberger, S., Viisanen, Y., and Paatero, J. (2003). Atmospheric aerosol over Finnish Arctic: source analysis by the multilinear engine and the potential source contribution function. *Atmos. Environ.*, 37(31):4381 – 4392.
- Zieger, P., Väisänen, O., Corbin, J., Partridge, D. G., Bastelberger, S., Mousavi-Fard, M., Rosati, B., Gysel, M., Krieger, U., Leck, C., et al. (2017). Revising the hygroscopicity of inorganic sea salt particles. *Nat. Commun.*, 8:15883.
- Zorn, S. R., Drewnick, F., Schott, M., Hoffmann, T., and Borrmann, S. (2008). Characterization of the South Atlantic marine boundary layer aerosol using an aerodyne aerosol mass spectrometer. *Atmos. Chem. Phys.*, 8(16):4711–4728.

Curriculum Vitae

Paul Herenz

Born on 25 January 1989
in Riesa, Germany
married, two children

EDUCATION & EMPLOYMENT

04/2018 – now	Senate Department for the Environment, Transport and Climate Protection, Department for Integrative Environmental Protection, Berlin, Germany
08/2014 – 03/2018	Ph.D. student at the Leibniz Institute for Tropospheric Research (TROPOS) Research: <i>Physical Properties of Arctic and Antarctic Aerosol Particles and Cloud Condensation Nuclei</i>
08/2010 – 07/2014	Student/scientific assistant at TROPOS
05/2014	Master thesis: <i>Investigations corresponding the influence of temporal change of the thermodynamic state on the surface structure of ice particles</i> Academic degree: Master of Science (M.Sc.)
10/2008 – 05/2014	Study of Meteorology, University of Leipzig, Germany
07/2007	Abitur form German secondary school qualifying for University admission or matriculation

Danksagung

Für die Hilfe, die ich während meiner Doktorandenzeit erhalten habe, möchte ich mich bei einer handvoll Personen herzlichst bedanken:

- Allen voran danke ich Frank Stratmann, der mich vom ersten bis zum letzten Tag in der Wolkengruppe stets unterstützt hat und mir mit humorvoller Ehrlichkeit oft die Richtung vorgegeben hat. Seine Betreuung hat mir das Verfassen dieser Arbeit überhaupt erst ermöglicht. Im Nachhinein erinnere ich mich besonders gerne an die stundenlangen Diskussionen zusammen mit Heike Wex über die PSCF.
- Ich bedanke mich bei allen Kollegen, die während meiner Zeit in der Wolkengruppe, den Wolkenturm als Arbeitsplatz mit mir geteilt haben. Jedes Büro und Labor stand für jedes kleinere und größere Anliegen stets offen, so dass Probleme jeglicher Art irgendwie immer gelöst wurden. Besonders danke ich Thomas Conrath für den besten technischen Support, den man sich nur vorstellen kann, und die tollen Mittagspausen. Weiterhin geht ein besonderer Dank an Silvia Henning, weil sie mich bei so vielen wissenschaftlichen Problemen vorangebracht hat und wir unsere Freude und unser Leid mit Matlab und dem CCNC immer wieder teilen durften.
- Ich möchte mich auch bei den Tropotones bedanken, da das Musizieren mit euch immer ein toller Gegenpart zur Arbeit war.
- Ich danke allen meinen Freunden und der gesamten Familie für Ratschläge und Aufmunterungen und natürlich für die Betreuung meiner kleinen Familie während meiner Kampagnenzeit.
- Danke Johanna, dass du die Zeit mit mir so ausdauernd und verständnisvoll durchgehalten hast, mir immer den Rücken freigehalten hast und mir in so vielen Momenten Mut und Zuversicht gegeben hast. Dein Anteil an dieser Arbeit ist aus so vielen Gründen, die über das Korrekturlesen und Bildersetzen weit hinausgehen, zwar kaum sichtbar aber enorm groß und wird womöglich nur noch vom folgenden Beitrag getoppt.
- Vielen Dank liebe Heike für alle deine Ratschläge, ob wissenschaftlich oder privat, für deine Unterstützung im Labor, für das Abfangen meiner Schreibschwäche, für immer wieder Druck machen und Vorantreiben und für all die Dinge, die hier gar keinen Platz finden aber für das Zustandekommen dieser Dissertation von enormer Wichtigkeit waren. Und natürlich dafür, dass du in all den Jahren einfach eine gute Freundin gewesen bist.